Hot Electron Generation and Transport in Fast Ignition Relevant Plasmas

Ian Andrew Bush

A thesis submitted for the degree of

Doctor of Philosophy

The University of York

Department of Physics

May 2012

Abstract

This thesis presents a mixture of theoretical work and experimental results relating to the generation and transport of relativistic electrons in fast ignition inertial confinement fusion.

First the theoretical work is presented, which focuses on the effect that a fast electron beam has on a background plasma. The fast electron beam drives a resistive return current in the plasma, which causes Ohmic heating, leading to a pressure gradient, and a $J \times B$ force. Both of these would be expected to cause cavitation in the background plasma. In this work an analytic model has been developed which shows that the pressure gradient is the dominant force, and predicts the significance of cavitation over a range of parameters relevant to fast ignition fusion. In addition to this the timescale on which shocks can form is considered. This work was verified by the development of a one dimensional fluid code which included the effects of a resistive return current, and was used to model shock formation when the cavitation in the plasma is strong. Some results from a two dimensional version of the code are also presented.

The experimental work in this thesis focuses on an experiment which looked at the interaction of a high-powered laser with gold cone targets, similar to those that would be used in cone-guided fast ignition schemes. In this experiment, the effect of defocusing the laser upon the production of hot electrons was investigated. A copper wire was attached to the cones to act as a diagnostic for the hot electrons. A ray-tracing code was developed to better understand the change in intensity inside the cone when the laser is defocused. The results of this experiment demonstrate that the energy coupling of the laser into hot electrons is maintained when defocusing, while the spectrum of the hot electrons softens.

To my parents.

Contents

List of Figures

Acknowledgements

The work contained in this thesis would not be possible without the input of a great number of people. I would firstly like to thank my supervisor, Dr John Pasley, for giving me the opportunity to begin with, and for all the help and support provided through my PhD. Clear explanations provided on all aspects of inertial confinement fusion have been particularly helpful.

I am also very grateful to Dr Alex Robinson, who has supervised me on the theoretical work contained in this thesis, while I was based at the Central Laser Facility, STFC Rutherford Appleton Laboratory. In addition to this, the sessions covering many aspects of plasma physics, for myself and other students based at the Central Laser Facility, have been extremely useful.

I would also like to thank Prof Peter Norreys, the head of the Plasma Physics Group at the Central Laser Facility, not only for providing me with the opportunity to work in the group, but also for making me feel very welcome during the time I was based there. I am also extremely grateful for the opportunity provided by Peter to be involved with experiments at the Jupiter Laser Facility and the Laboratory for Laser Energetics. I would also like to thank Dr Raoul Trines in the same group for his help with Fortran, LaTeX and Linux.

I am very grateful to the experimental staff at the Central Laser Facility, for all their help during experiments. Without their level of expertise the experimental work presented in this thesis would not be possible.

I would also like to thank the other students and academics in the field, with whom I have shared an office, been on experiment, chatted to over coffee or attended summer schools and conferences. There are too many such people to name, but the people in the community are part of the reason the PhD has been so enjoyable.

Finally, thank you to Rachel, for being patient with me and helping to keep me focused while I have written up my PhD.

The Role of the Author

The work presented in chapter 3 of this thesis was the author's own work, and was done primarily under the supervision of Dr Alex Robinson.

The work presented in chapter 4 is experimental, and by its nature requires a large team of collaborators. The author assisted in setting up many of the diagnostics used, and had a primary role in running the HOPG spectrometers and the electron spectrometer, whilst also running other diagnostics at various times. The author also had a primary role in the target alignment process. The other experimental collaborators provided the knowledge of setting-up and running such experiments. The author did not have any role in the planning prior to the experiment. The staff at the Central Laser Facility were crucial in many aspects of the experiment, providing the technical expertise required in running the laser and manufacturing the targets. All of the data was analysed by the author, with the exception of the electron spectrometer data. Parts of the analysis where significant help was given by others have been acknowledged. The ray-tracing code presented in chapter 4 was entirely the authors own work. Simulation results presented that were not done by the author are acknowledged.

Publications Resulting

Based on the results presented in Chapter 3:

> I. A. Bush, A. P. L. Robinson, R. Kingham and J. Pasley. Cavitation and shock wave formation in dense plasmas by relativistic electron beams. *Plasma Physics and Controlled Fusion*, **52** 12 p. 125007, 2010. Web: `dx.doi.org/10.1088/0741-3335/52/12/12500`

Based on the results presented in Chapter 4:

> I. A. Bush, A. G. R. Thomas, L. Gartside, S. Sarfraz, E. Wagenaars, J. S. Green, M. Notley, H. Lowe, C. Spindloe, T. Winstone, A. P. L. Robinson, R. Clarke, T. Ma, T. Yabuuchi, M. Wei, F. N. Beg, A. MacPhee, A. J. MacKinnon, M. H. Key, W. Nazarov, M. Sherlock and J. Pasley. Effect of Defocusing on Picosecond Laser-Coupling into Gold Cones. *With co-authors, in final stages of preparation for submission to PRL as of May 2012.*

Chapter 1

Introduction

1.1 Overview and Motivation

Nuclear fusion has the potential to offer one of the most attractive long-term energy solutions; one that is free of emissions, has enough fuel to last for millions of years, and has no long-lived radioactive waste. Indeed, most of the energy used on Earth already comes indirectly from fusion power, via proton-proton reactions in the sun. The idea of creating a fusion based power station on Earth gained credibility in the 1950s, with the successful demonstration of the H-bomb and the creation of the first devices to magnetically confine plasmas.

Shortly after, in 1960, the first optical laser was created, and just a year later Q-switching was demonstrated, allowing laser pulses with hundreds of kilowatts of power and pulse lengths on the order of nanoseconds [1]. It was quickly realised that lasers, which had been described as "a solution looking for a problem" [2], could potentially be used to ignite fusion fuel. Decades later, despite huge advances in laser power and in the understanding of magnetic confinement devices, this feat has still not been realised. However, with the completion of the National Ignition Facility, the demonstration of fusion ignition for peaceful purposes is unlikely to be far away.

The need for alternative energy sources is a pressing one; demand for energy is growing rapidly. Globally, demand for electricity is predicted to increase by 2.5% per year up until 2030 [3], with 28% of this growth coming from China

alone. Concerns about the availability of fossil fuels and the implications of global warming have driven the development of renewable energy resources, such as wind and solar power. However, it is unlikely that renewable energy alone can meet global demand [4]. In the longer term alternatives will be needed, and here fusion power is a desirable option, with enough fuel available on Earth to last for millions of years.

1.2 Nuclear Fusion

The fusion reaction of most interest is the deuterium-tritium (DT) reaction, due to the fact it has the highest fusion cross-section of any possible reaction below temperatures of a few hundred keV. The reaction is given by

$$ {}^{2}_{1}\mathrm{D} + {}^{3}_{1}\mathrm{T} \rightarrow {}^{4}_{2}\mathrm{He}\ (3.5\ \mathrm{MeV}) + {}^{1}_{0}\mathrm{n}\ (14.1\ \mathrm{MeV}) \tag{1.1} $$

where, due to momentum conservation, the neutron carries 80% of the energy, and the helium nucleus (an α-particle) 20% of the energy. Figure 1.1 shows the reaction rate for DT compared to four other fusion reactions.

Deuterium is a naturally abundant isotope of hydrogen, accounting for 1 atom in 6,700 of hydrogen on Earth. Tritium is more problematic however, as it has a half life of 12.3 years, so is not found naturally. Tritium can be produced by neutron reactions with lithium however, for which easily accessible reserves would provide 20,000 years worth of fuel [5]. Lithium is also present in seawater, which contains sufficient quantities to breed tritium for fusion energy for millions of years, although it is more difficult to extract [4]. The most useful for reaction for creating tritium involves lithium-6,

$$ {}^{6}_{3}\mathrm{Li} + {}^{1}_{0}\mathrm{n} \rightarrow {}^{4}_{2}\mathrm{He}\ (2.1\ \mathrm{MeV})\ + {}^{3}_{1}\mathrm{T}\ (2.7\ \mathrm{MeV}). \tag{1.2} $$

A fusion power plant would have to produce its own tritium, which could be achieved by surrounding a burning DT plasma with a lithium blanket. The lithium-6 reaction would not on its own produce enough tritium, due to inevitable losses in neutrons produced from the burning DT plasma, so neutron multipliers would be needed. The lithium-6 reaction works optimally with slower neutrons,

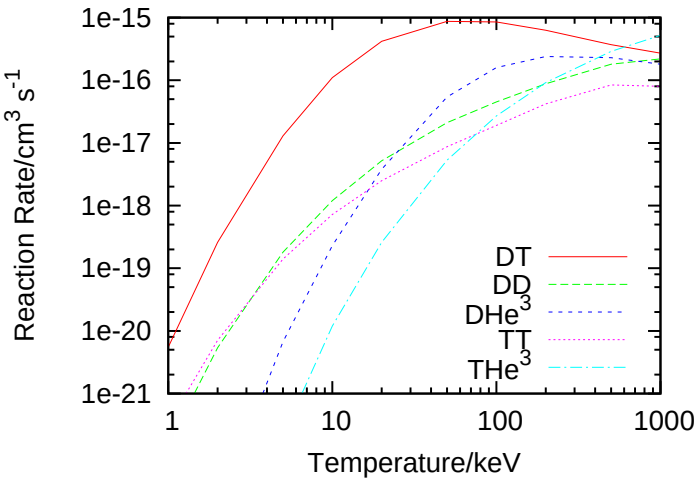

Figure 1.1: Reaction rates for five different fusion fuels [6]. The DT reaction has the highest reaction rate below temperatures of a few hundred keV.

so a moderator to slow the fusion-produced neutrons down is also required. Naturally lithium is made up of just 7.4% lithium-6, and 92.6% lithium-7, which also reacts with a neutron to produce tritium via the reaction

$$^{7}_{3}\mathrm{Li} + ^{1}_{0}\mathrm{n} \rightarrow ^{4}_{2}\mathrm{He} + ^{3}_{1}\mathrm{T} + ^{1}_{0}\mathrm{n}. \tag{1.3}$$

However, this reaction has a much smaller cross-section than the lithium-6 reaction, making it difficult to use to produce enough tritium. Additionally it is an endothermic reaction, consuming 2.5 MeV of energy, and hence reducing the heating in the lithium blanket. The purpose of the lithium blanket, as well as producing tritium, would be to generate heat to drive steam turbines, ultimately producing electricity. A more complete discussion of the blanket design for DT fuel is given in by Freidberg [5].

Another approach that could be pursued in a fusion reactor is to use the deuterium-deuterium (DD) reaction,

$$^{2}_{1}\mathrm{D} + ^{2}_{1}\mathrm{D} \begin{array}{l} \rightarrow ^{3}_{2}\mathrm{He}\ (0.82\ \mathrm{MeV}) + ^{1}_{0}\mathrm{n}\ (2.45\ \mathrm{MeV}) \\ \rightarrow ^{3}_{1}\mathrm{T}\ (1.01\ \mathrm{MeV}) + ^{1}_{1}\mathrm{p}\ (3.02\ \mathrm{MeV}) \end{array}, \tag{1.4}$$

which has two possible branches, both with approximately equal probability of

occurring. These two primary reactions release much less energy than that of the DT reaction, but secondary reactions will occur because of the tritium and helium-3 produced. It is difficult to envisage how a pure DD plasma could ignite; figure 1.1 shows the temperature needed is orders of magnitude higher just to achieve a similar reaction rate to DT fusion. Using the DT reaction to heat the fuel and start the DD reactions may be one way around this [7]. In such a scheme a lithium blanket may not be required, as the unburnt tritium produced from the DD reaction could potentially be used [8].

Finally, the deuterium-helium-3 reaction proceeds as

$$ {}^{2}_{1}\mathrm{D} + {}^{3}_{2}\mathrm{He} \rightarrow {}^{4}_{2}\mathrm{He}\ (3.6\ \mathrm{MeV}) + {}^{1}_{0}\mathrm{p}\ (14.7\ \mathrm{MeV}), \tag{1.5} $$

however there are no neutrons produced, only charged particles. This could be a desirable approach as the charged particles have the potential to be used for direct electricity generation without the need for the inefficient steam turbines. In addition to being difficult to initiate however, there is also very little helium-3 available on Earth [9].

The temperature for fusion reactions to occur needs to be high, so that the kinetic energy of the ions overcomes the repulsive Coulomb force, and allows them to come close enough together that the strong force dominates. The challenge however is not so much in starting the first fusion reactions, which has been achieved in numerous different ways, but to keep the reactions going in a self-sustaining manner. Stars achieve this by means of gravitational confinement, where the gravitational forces are sufficient to achieve the densities and pressures required to start fusion reactions, and the pressure generated from fusion moderates the star's inwards collapse.

To achieve fusion on Earth there are a number of approaches. One way is magnetic confinement fusion (MCF), where a toroidal plasma is kept in a steady state by toroidal and poloidal magnetic fields, known as a tokamak. In this case the plasma density is low, $\sim 10^{-11}$ g cm^{-3}, but as the plasma is at a temperature of around 10 keV the pressure is $\sim$10 bar. Inertial confinement fusion (ICF) offers a very different approach. A small pellet containing a few milligrams of fusion fuel is compressed and heated, and the confinement is provided only by

the time the compressed pellet takes to blow itself apart again. In this case the same temperature of ∼10 keV is required[1], but the density is many orders of magnitude higher, with peak densities in excess of 1000 g cm^{-3} and pressures exceeding 10^{12} bar.

There are also a large number of approaches that occupy an intermediate regime between MCF and ICF, known as magneto-inertial fusion. One such scheme is known as magnetised target fusion, where a plasma is inserted into a thin metal liner. A large current, on the order of mega-amps, is passed through the metal liner, driving an implosion via the $J \times B$ force, and compressing the plasma [10, 11]. Such schemes have a lot in common with inertial confinement approaches, but the magnetic field reduces losses by thermal conduction, and enhances alpha-particle deposition via a reduced Larmor radius.

1.3 Inertial Confinement Fusion

1.3.1 Direct Drive

Using lasers to heat and compress a target directly, with the laser light incident on the surface of a DT target, is known as direct drive [12]. A typical inertial confinement fusion target for direct drive is described in *The Physics of Inertial Fusion* by Atzeni and Meyer-ter-Vehn [8]. The target contains 2 mg of DT fuel and is 2 mm in radius, as shown in figure 1.2. The surface is heated symmetrically by a number of laser beams, causing the plastic shell that coats the target to ablate, driving an inwards reaction force and compressing the DT fuel.

Reference [8] shows the densities, pressures and temperatures obtained in the capsule at a number of different times, along with the laser pulse shape. The laser pulse starts off with a 12 ns foot pulse, at 1.3 TW, and then increases to the peak power of 600 TW, before switching off at 23 ns. The pulse shape in this simulation is designed to give isentropic compression, that is compression at a constant entropy. This minimises the energy required for the compression of the target.

[1] A temperature of ∼10 keV is required for ignition, but during the burn phase in an ICF target the temperature exceeds 100 keV.

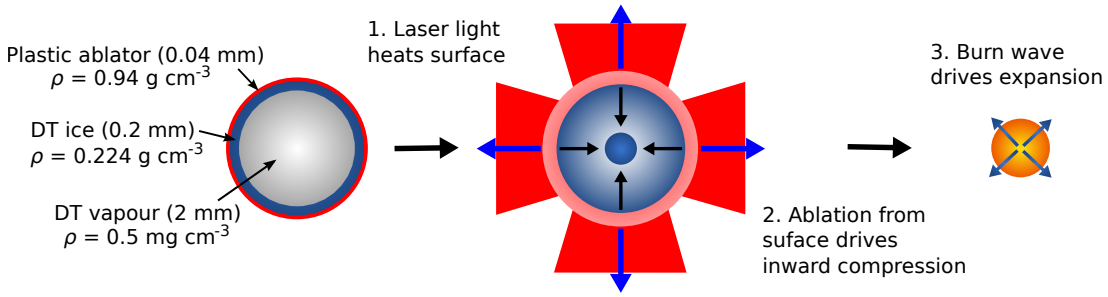

Figure 1.2: Compression and heating in inertial confinement fusion. The thickness and density of different layers are shown.

At the end of the implosion the plasma at the centre of the fuel reaches the highest temperature at ∼10 keV, and in this region the fusion reactions start. This central region of the fuel is also where the highest pressure of 170 Gbar occurs, while the peak density of 440 g cm^{-3} occurs in the colder fuel surrounding the hotspot. At the end of the implosion the hotspot begins to undergo self-heating, reaching a temperature of ∼70 keV in around 100 ps. At this point a thermonuclear burn-wave propagates into the cold fuel, as fusion products and electron conduction from the hotspot act to heat it. During the burn phase temperatures rise above 100 keV, and multi-Tbar pressures are achieved. This is known as central hotspot ignition.

1.3.2 Laser Light Absorption in Direct Drive ICF

In direct drive ICF the surface of the fuel pellet is heated and creates an ablating plasma around the target. The laser light can only propagate up to the critical surface, which is given by

$$n_c = \frac{(2\pi)^2 m_e \epsilon_0 c^2}{e^2 \lambda_L^2} \simeq 10^{21} (\lambda_{L\mu m})^{-2} \mathrm{cm}^{-3}, \tag{1.6}$$

where m_e is the mass of the electron, ϵ_0 the permittivity of free space, c the speed of light, e the elementary charge and λ_L the wavelength of the laser light ($\lambda_{L\mu m}$ is the wavelength of the laser light in micrometres)[1]. For a 1.053 µm

[1]This critical density applies for laser intensities up to around 10^{18} W cm^{-2}. Above this a relativistic correction needs to be applied, see section 1.5.1.

wavelength laser incident on a DT plasma this would give a critical density of 4×10^{-3} g cm^{-3}. This is much lower than some of the values considered in section 1.3.1, so the laser light itself will not propagate into the dense fuel. Plasma which has a lower density than the critical density for a particular wavelength of light being considered is known as underdense, and plasma with a greater density overdense. Laser light is absorbed in the underdense pre-plasma up to the critical density, where the light can not propagate any further and the energy is partially absorbed and partially reflected. There are two methods by which laser light is usually absorbed in ICF, known as collisional absorption and resonance absorption.

Collisional absorption, also known as inverse bremsstrahlung, is a local energy deposition process [13]. For 3ω laser light ($\lambda_L = 0.351$ µm) at an intensity of around 10^{15} W cm^{-2}, such as is typically used in direct drive, collisional absorption is dominant. In collisional absorption an electron begins to oscillate in the electric field of the laser. If the electron undergoes a collision with an ion, while it is still oscillating in the electric field, some of the energy is transferred to thermal energy in the plasma. In underdense plasmas, such as the ablating shell of an ICF capsule, this is the dominant energy absorption process.

The efficiency of collisional absorption is dependent not only on the laser intensity and wavelength, but also on the density scale length of the plasma and the polarisation of the laser light. Over the first few cycles of a laser pulse, incident on a solid target, a layer of plasma is formed which is much higher than the critical density. This gives a scale length of the plasma as $L = c_s \tau_L$, where c_s is the plasma sound speed and τ_L the laser pulse duration. The sound speed is given by $c_s = \sqrt{\gamma k_B T_e / m_i}$, where γ is the adiabatic index, k_B is Boltzmann's constant, T_e the temperature of the electrons and m_i the mass of the ions in the plasma. For a short pulse, picosecond laser the value of L may be around 0.1 µm, but for direct drive ICF the scale length of the plasma is on the order of ∼100 µm [14]. This density scale length is not necessarily created just by the main laser pulse, but also by any pre-pulse present in the laser system, if it has a high enough intensity. This leads to the formation of a pre-plasma with a long density scale length, before the arrival of the main laser pulse.

Provided the density gradient is long enough, i.e. $L/\lambda_L \gg 1$, the solution

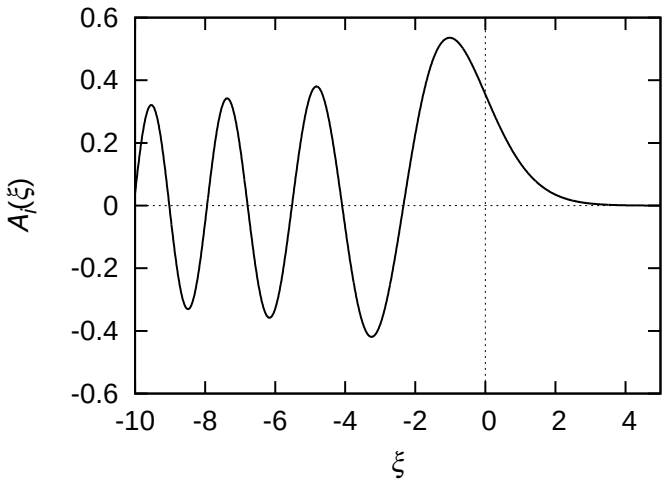

Figure 1.3: A plot of the Airy function, $A_i(\xi)$, which is proportional to the electric field incident on a plasma slab with a density given by $n_e = n_c x/L$, where $\xi = (\omega_L^2/c^2 L)^{1/3}(x - L)$.

for the electric field can be found by the Wentzel-Kramers-Brillouin (WKB) approximation. For s-polarised light, where the electric field is perpendicular to the density gradient and direction of propogation, the electric field is found to be proportional to an Airy function, as plotted in figure 1.3. The absorption fraction is given by

$$\psi = 1 - \exp\left(-\frac{8\nu_{ei}L}{3c}\cos^3\theta\right), \tag{1.7}$$

where ν_{ei} is the electron-ion collision frequency and θ the angle between the density gradient and the laser pulse. Hence it can be seen that the longer the plasma scale-length the higher the absorption efficiency.

For p-polarised light, where the field is in the plane of the density gradient, a mechanism known as resonance absorption becomes important. This is a collisionless process, where part of the incoming laser energy is transferred into electrostatic oscillations in the plasma [15]. These longitudinal waves, also known as Langmuir or plasma waves, have a frequency ω_p given by

$$\omega_p^2 = \frac{n_e e^2}{m_e \epsilon_0}, \tag{1.8}$$

where n_e is the electron number density. There are specific conditions that need to be met for resonance absorption to occur. In addition to being p-polarised the laser must be entering at an oblique angle to the density gradient. If these conditions are met the laser light will propagate up to a density $n_c \cos^2\theta$ [16]. At this density part of the wave will then be reflected, and some of the energy will excite a Langmuir wave.

Due to resonance absorption, p-polarised light always has a higher or equal fraction of absorption to s-polarised light. The optimal angle for the resonance absorption is dependent on the parameter L/λ, for $L/\lambda = 1$ the optimal angle is around 25°, where the p-polarised light would have an absorption of around 60%. For s-polarised light at the same parameters the absorption is around 20%.

Simulations show that the fast electron temperature scaling of resonance absorption is given by

$$T_f \approx 10(T_e I_{15} \lambda_{L\mu m}^2)^{1/3} \text{ keV}, \tag{1.9}$$

where I_{15} is the laser intensity in units of 10^{15} W cm^{-2}, $\lambda_{L\mu m}$ the wavelength in micrometres, and T_f and T_e the temperature of the fast (hot) electrons and background electrons respectively, in keV [16, 17, 18].

There are other important methods by which laser light can be absorbed at higher intensities and longer wavelengths, above the value of $I\lambda_L^2$ required for direct drive ICF, for example vacuum heating and $J \times B$ heating [14]. Collisional absorption is desirable for ICF, due to the fact the laser energy is deposited close to the critical surface [19]. Conversely, resonance absorption transfers energy into a small fraction of the electrons, which deposit their energy throughout the target. This means the pressure in the centre of the ICF target is raised prematurely, limiting the compression that is achieved.

1.3.3 The Rayleigh-Taylor Instability

Rayleigh-Taylor instabilities (RTI) occur in fluids when a lower density fluid accelerates a higher density fluid [20], such as when a lighter fluid is supporting a heavier fluid. At the interface between the two the instability occurs, and fingers of the heavier fluid penetrate into the lighter one. In ICF there are two points at

which RTIs occur, the first is during the ablative acceleration of the fuel, which can cause the shell of the DT fuel to rupture and mix with the ablator. The second occurs when the low density, high pressure central hotspot in the fuel begins to decelerate the incoming cold, dense shell of fuel. This causes mixing between the cold and the hot fuel, reducing the fusion yield in the target.

The growth rate of the instabilities, η, is exponential with time, that is $\eta \sim e^{\sigma t}$. Classically $\sigma = \sqrt{A_t a k}$, where a is the acceleration of the fluid and k the wave number of the perturbation. If λ is the characteristic wavelength of the perturbation then $k = 2\pi/\lambda$. A_t is the Atwood number, given by $A_t = (\rho_h - \rho_l)/(\rho_h + \rho_l)$, where ρ_h and ρ_l are the densities of the heavier and lighter fuels respectively [8]. This classical value for the RTI growth would be prohibitively large in ICF, requiring the initial perturbation to be on the nanometre scale, which is not practically possible. Fortunately, other effects during the compression of an ICF capsule reduce the size of the instability.

The main reduction in the growth is due to the fact that the acceleration is ablation driven. A model by Takabe *et al.* [21] gives the growth rate as $\sigma = 0.9\sqrt{ak} - 3ku_a$, where u_a is the ablation velocity. This gives a much smaller growth rate than the classical case, and for small wavelengths the ablation actually stabilises any perturbations ($\sigma < 0$). A comparison of classical and ablative RTIs are shown in figure 1.4. Other reductions in the growth rate come from the density gradients that are present, and thermal conduction.

Rayleigh-Taylor instabilities are not the only instabilities that occur in ICF. Two others that are important are the Kelvin-Helmholtz instability and the Richtmyer-Meshkov instability. The former occurs at the interface where two fluids are moving in opposite directions, when viewed from some frame, known as counter-streaming. For example, the waves caused by the wind blowing over the ocean are due to the Kelvin-Helmholtz instability. In ICF the Kelvin-Helmholtz instability occurs when fingers of the heavier fluid move in to the lighter one, due to the Rayleigh-Taylor instability. This leads to counter-streaming along the boundary between the fluids, and the growth of the Kelvin-Helmholtz instability. The Richtmyer-Meshkov instability occurs when a shock propagates across the interface between two different fluids, which can seed both Rayleigh-Taylor and Kelvin-Helmholtz instabilities.

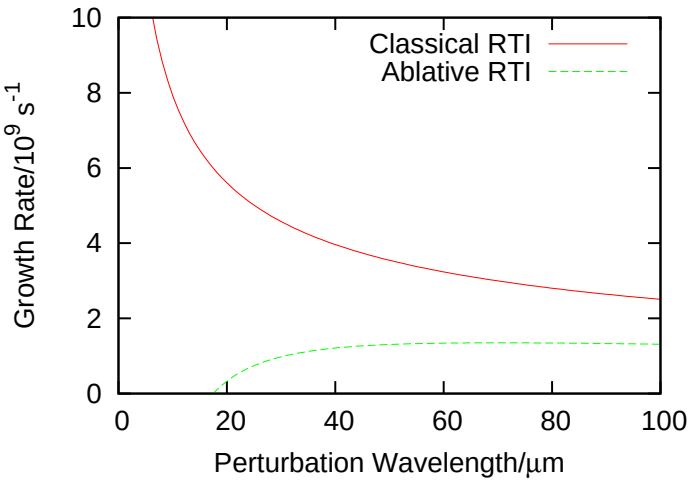

Figure 1.4: Comparison of the classical and ablative Rayleigh-Taylor instability growth rates, for $a = 10^{14}$ m s^{-2}, $u_a = 5 \times 10^3$ m s^{-1}. Based on a figure from *The Physics of Inertial Fusion* by Atzeni and Meyer-ter-Vehn [8].

1.3.4 Indirect Drive

For a pellet of fusion fuel to achieve a sufficiently high temperature and density for ignition the instabilities during the implosion need to be kept small. To minimise the growth of the instabilities the radiation used to heat and compress the fuel needs to be as uniform as possible, as does the target itself. In direct drive this is an issue, as many overlapping laser beams are required to avoid any significant non-uniformity, for example from interference patterns between the different laser beams, and laser beam speckle.

Indirect drive avoids this problem, by relying on approximately black body radiation to compress and heat the fusion fuel [22]. Energy is absorbed into a hohlraum, typically from a similar type of laser beam to those that would be used in direct drive. The hohlraum then heats up and emits approximately black body radiation in the form of X-rays, as shown in figure 1.5, which cause the ablation required on the surface of the target. The structure of the target is similar to that of direct drive, although the ablator would be made of a different material. The reason for this is that the capsule implosion is very sensitive to the opacity of the ablator material. Beryllium is a favoured choice for the ablator material in

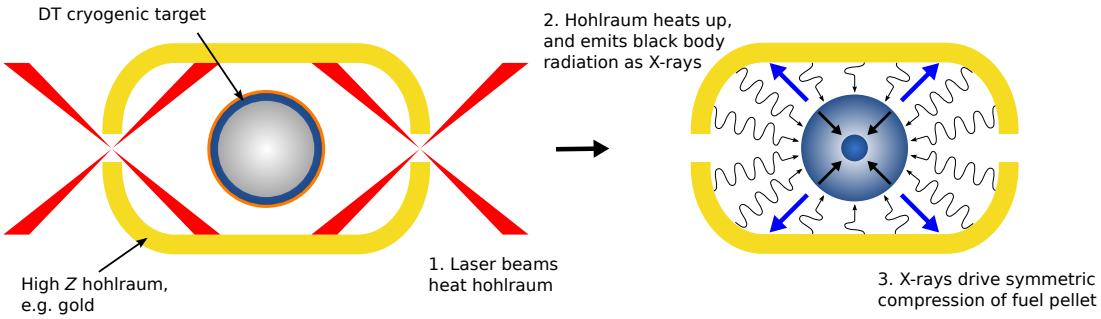

Figure 1.5: Laser heating is used in indirect drive to heat the hohlraum. X-ray radiation from the hohlraum walls then provides the compression and heating of the fuel. The DT target would be similar to that shown in figure 1.2, with a different ablator material.

indirect drive, in addition to a low opacity when heated it has other favourable properties such as a high density and a low specific heat [23]. Where beryllium is used it can be doped with copper, typically <1%, to allow finer control over the opacity. This has the effect of reducing the radiative preheating of the DT fuel.

The significant advantage with indirect drive is that the Rayleigh-Taylor instabilities, that limit the compression achieved, are mitigated by the very high uniformity of the X-ray radiation and a higher ablation velocity. Black body radiation is also incoherent, so there are no concerns with interference patterns as there are with direct laser heating. The downside to using this approach is the low efficiency. A reference example given in *The Physics of Inertial Fusion* [8] gives the radiation absorbed by the fuel capsule as 6%, compared with 78% of the laser energy for the direct drive target described in section 1.3.1.

Using laser light is not the only option for heating the hohlraum. Other options include ion-beam [22] and Z-pinch [24] hohlraum heating. A Z-pinch works by passing a large current, on the order of megaamperes, through a hollow cylinder, along its length. This leads to a $J \times B$ force, which is directed inwards from the cylinder surface towards the axis of the symmetry in the cylinder. The resistive (Ohmic) heating leads to the material on the surface of the cylinder to ablate, which the $J \times B$ force will cause to flow towards the axis of the cylinder. The resulting high-temperature plasma radiates X-rays, which would act to heat

the hohlraum. Z-pinch driven fusion could provide a possible advantage in terms of driver efficiency. Currently Z-pinches achieve around 10 - 15% efficiency in converting electrical power into X-rays [25]. The best performing Z-pinches take the form of wire-arrays.

In comparison, the National Ignition Facility (NIF) [26], which has 192 laser beams to provide the hohlraum heating, has an efficiency of just 0.5% in converting electrical energy to laser light [27]. One way to improve this is to use a diode pumped solid state laser, where the flash lamps, which emit a wide spectrum of light to pump the lasing medium, are replaced with diode lasers. The Mercury laser at Lawrence Livermore National Laboratories in the US [28] and the DiPOLE project at STFC Rutherford Appleton Laboratory in the UK [29] are examples of developmental diode pumped solid state lasers. Such lasers would potentially offer electrical to optical efficiencies up to 30% [30]. Using this method of pumping also allows the high repetition rates required for Inertial Fusion Energy (IFE), something that remains a significant challenge for Z-pinch driven fusion.

1.3.5 The Lawson Criterion

In a tokamak [31], where the aim is to hold the plasma in a steady state for many minutes, the condition for ignition is given by the Lawson criterion [32], where the energy losses must be balanced by energy released from fusion reactions. For a DT plasma the fusion reaction rate is given by $n_D n_T \langle \sigma v \rangle_{DT}$, where n_D and n_T are the number densities of the deuterium and tritium ions respectively and $\langle \sigma v \rangle_{DT}$ is the reaction rate for DT, averaged over a Maxwellian distribution, as shown in figure 1.1. Each reaction releases 17.6 MeV of energy, E_{DT}, as shown in equation 1.1. In the derivation of the Lawson criterion the energy of the neutron is neglected, as the neutron escapes the plasma without heating it significantly.[1] The energy contained in the DT ions in the plasma is given by $\frac{3}{2}(n_D + n_T + n_e) k_B T$. The energy confinement time is represented by

[1] The same assumption can not be made in ICF, where the neutrons do make a contribution to the plasma heating.

τ_{conf}. Putting this together gives the energy balance as

$$\frac{n_i^2}{4} \langle \sigma v \rangle_{DT} E_{DT} = \frac{3 n_i k_B T}{\tau_{conf}} \tag{1.10}$$

assuming equimolar DT, that is $n_i = \frac{n_D}{2} = \frac{n_T}{2} = n_e$. This can be re-arranged to find the ignition condition

$$n_i \tau_{conf} > \frac{12 k_B T}{\langle \sigma v \rangle_{DT} E_{DT}} \sim 10^{20} \text{ s m}^{-3} \tag{1.11}$$

for a plasma at 20 keV. This is known as the Lawson Criterion. The choice of temperature as 20 keV is not arbitrary, this represents the optimal balance between losses in the plasma, due to bremsstrahlung radiation, against a low fusion reaction rate. To establish a minimum temperature required for ignition the bremsstrahlung losses can be compared against the α-particle heating. Approximate equations for bremsstrahlung power loss and α-particle heating are respectively given by

$$P_{brem} = 5.34 \times 10^{-25} \; n^2 T_{keV} \text{ W m}^{-3} \tag{1.12}$$

and

$$P_{DT} = 5.15 \times 10^{-19} \; n^2 T_{keV}^{-2/3} e^{-19.94 T_{keV}^{-1/3}} \text{ W m}^{-3}, \tag{1.13}$$

where $n = n_D/2 = n_T/2 = n_i = n_e$ [6, 8]. Note equation 1.13 for the DT fusion power is only accurate for temperatures up to ∼25 keV. These equations are plotted in figure 1.6. From this it can be seen that the minimum temperature required in the plasma is ∼5 keV. Below this the bremsstrahlung losses outweigh the α-particle heating. Other loss mechanisms and imperfect confinement of the α-particles will make the minimum required temperature higher still. Further analysis along these lines shows that the optimal plasma temperature in a tokamak, which will minimise the value of $n\tau_E$ required, is around 20 keV.

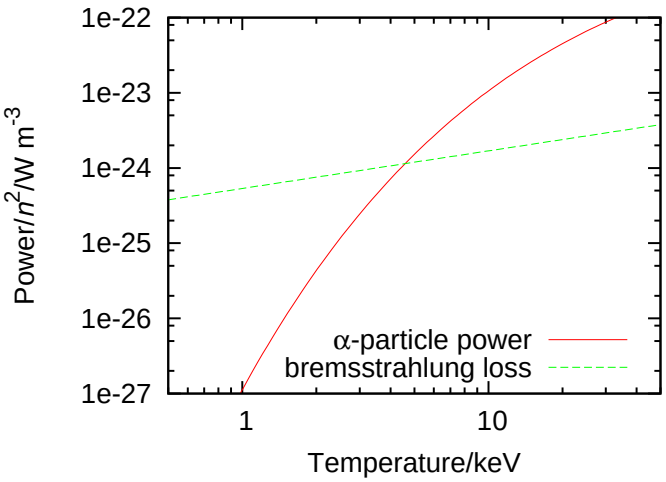

Figure 1.6: A comparison of power loss by bremsstrahlung radiation in a plasma to the power generated by the fusion α particles. Note the y-axis scale is divided by n^2.

1.3.6 The Areal Density Criterion, Burn Efficiency and Gain for ICF

To determine a comparable parameter to the Lawson criterion in equation 1.10 for ICF the amount of fuel burned during the confinement of the fuel needs to be considered. The reaction rate is given by

$$\frac{dn_{fus}(t)}{dt} = n_D(t) n_T(t) \langle \sigma v \rangle_{DT} \,, \tag{1.14}$$

where n_{fus} is the number of fusion reactions per unit volume. The fraction of the fuel burned is given by $f_B = 2n_{fus}(t)/n_0$, where n_0 is the initial ion number density, taken to be equal parts deuterium tritium. The deuterium and tritium ion number densities are then given by

$$n_D(t) = n_T(t) = \frac{n_0}{2} - n_f(t) = \frac{n_0}{2}\left(1 - f_B\right) \tag{1.15}$$

and taking the derivative of f_B with respect to time gives

$$\frac{df_B}{dt} = \frac{n_0}{2}\left(1 - f_B\right)^2 \langle \sigma v \rangle_{DT} \,. \tag{1.16}$$

Solving the previous equation allows the fraction of fuel burned, f_B, to be found

$$\int_0^{f_B} \frac{1}{(1-f'_B)^2} df'_B = \int_0^{\tau_{conf}} \frac{n_0}{2} \langle \sigma v \rangle_{DT} \, dt, \tag{1.17}$$

where τ_{conf} is the time the fuel is confined for. Solving and rearranging for f_B yields

$$f_B = \frac{n_0 \tau_{conf} \langle \sigma v \rangle_{DT}}{n_0 \tau_{conf} \langle \sigma v \rangle_{DT} + 2}. \tag{1.18}$$

In this equation the confinement time, τ_{conf} still needs to be determined. The average confinement, considering a rarefaction wave travelling towards the centre of a sphere of radius R, at the sound speed, c_s, would give a confinement time $\tau_{conf} = R/2c_s$. However, the distribution of mass in a sphere scales as R^3, so this would overestimate the confinement. The average confinement in a sphere of uniform density is given by

$$\langle \tau_{conf} \rangle = \frac{1}{M_0} \int_0^R \frac{dM}{dr} \tau_{conf}(r) dr, \tag{1.19}$$

where $\tau_{conf}(r) = R - r/c_s$, M is the mass in the sphere, and M_0 the initial mass. The resulting average confinement is found to be

$$\langle \tau_{conf} \rangle = \frac{R}{4c_s}. \tag{1.20}$$

Using this in equation 1.18, and taking $n_0 = \rho/m_i$, where ρ is the fuel density and m_i the average ion mass, gives the value of the fractional burn-up as

$$f_B = \frac{\rho R}{\frac{8c_s m_i}{\langle \sigma v \rangle_{DT}} + \rho R}. \tag{1.21}$$

The terms in the denominator are commonly collected together as the burn parameter, H_B, given by

$$H_B = \frac{8c_s m_i}{\langle \sigma v \rangle_{DT}}. \tag{1.22}$$

From equation 1.21 it can be seen that the amount of fuel burned in the target

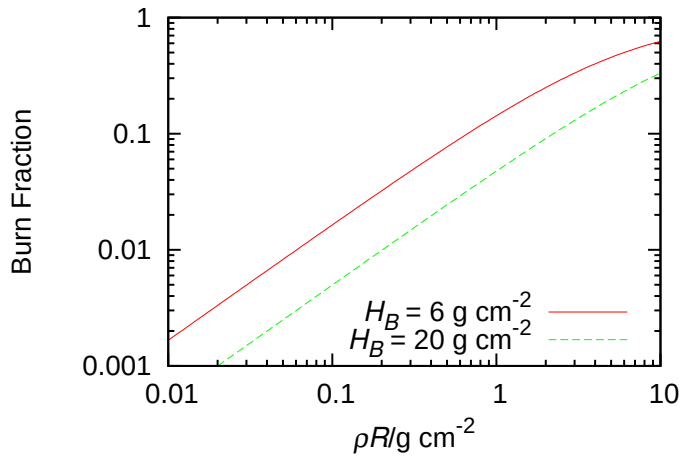

Figure 1.7: Burn efficiency as a function of the areal density, for two values of H_b. The smaller value of H_b (solid line) corresponds approximately to the temperature range 20 - 100 keV, while the larger value corresponds to 10 keV.

is dependent on the ratio of the areal density, ρR, to H_B.

The burn parameter is approximately constant between 20 and 70 keV, and a value of 7 g cm^{-2} can be used [33]. Plots of the burn fraction against ρR are shown in figure 1.7, for two different values of H_B. These two values approximately correspond to 10 keV and 20 - 70 keV plasmas. Using this equation a value of ρR $\sim$3 g cm^{-2}, at a temperature of 20 keV, is required to achieve a 30% burn-up in the target.

This dependence on ρR implies a target for ICF could be constructed that is large, and has a modest density. However, the fusion yield from such a target would be too much to realistically contain, and the energy to heat such a target to ignition temperatures would be unfeasibly large. The reference target discussed in section 1.3.1 would have a peak ρR in the fuel of 1.7 g cm^{-2} and a peak density of 440 g cm^{-3}, achieving a 19% burn-up of the fuel.

It is also important to consider the gain in an ICF target, which is defined as $G = E_{fus}/E_{drv}$, where E_{fus} and E_{drv} are the fusion energy yield and driver energy respectively. A gain of $G = 1$ represents the case where the laser energy onto the target is equal to the fusion power produced, but this ignores the inefficiencies associated with the driver, the inefficiency in converting the neutron deposited

energy into electricity, and the fact that not all of the fusion energy is in the form of neutrons. The driver efficiency, ψ_{drv}, that is the efficiency of the laser system, at best could be around 30% (see section 1.3.4). The efficiency of a generator, ψ_{gen}, in converting the heat from the lithium blanket to electricity would also be around 40% [5]. Overall this gives a requirement for the gain as

$$G > \frac{1}{\psi_{drv}\psi_{gen}} \sim 10 \tag{1.23}$$

for break-even. To produce useful power a fusion power plant would need a gain of 30 - 100 [8]. The direct drive target discussed in section 1.3.1 would have a gain of ∼60, with a laser energy input of 1.7 MJ and a released fusion yield of ∼100 MJ. Optimised targets with higher gains than this would be desirable for fusion power, and such targets would need to be shot at ∼10 Hz for a power station generating ∼1 GW of power.

If the DT fuel is uniformly heated, then the gain in the target is given by

$$G = \frac{E_{DT}}{4\left(\frac{3}{2}k_B T\right)} f_B, \tag{1.24}$$

where the energy released from each fusion reaction has been divided by the thermal energy for two ions and two electrons. Hence, when heating the fuel to a temperature of 5 keV, the gain, for $f_B = 0.3$, is approximately 20. This is too low for useful power generation. For this reason only a small amount of the fuel, the hotspot (see section 1.3.1), is heated to fusion temperatures. The hotspot is then surrounded by colder denser fuel. The hotspot size must be sufficient for it to self-heat, due to the fusion borne α-particles, and create a burn wave that propagates into the cold fuel. For the α-particles to deposit a significant amount of their energy within the hotspot, the areal density of the hotspot must exceed ∼0.3 g cm^{-2} [8].

1.4 Shocks

In inertial confinement fusion rapid compression is required, and the compression driven by high powered lasers leads to strong shock waves in the DT fuel.

The Hugoniot curves relates the pre-shock density, pressure and velocity to the post-shock values [34]. Figure 1.8 shows the pre-shock region, subscript 1, and post-shock region, subscript 2, variables in the stationary frame of the shock. The Hugoniot curves are given by

$$\frac{\rho_2}{\rho_1} = \frac{u_1}{u_2} = \frac{(\gamma+1)p_2 + (\gamma-1)p_1}{(\gamma-1)p_1 + (\gamma+1)p_2} \tag{1.25}$$

$$\frac{p_2}{p_1} = \frac{(\gamma+1)\rho_2 + (\gamma-1)\rho_1}{(\gamma-1)\rho_1 + (\gamma+1)\rho_2}, \tag{1.26}$$

where $\gamma = C_p/C_V$, the ratio of the constant pressure specific heat to the constant volume specific heat. Taking the case of a strong shock, where $p_2 \gg p_1$, the relation for the density and velocity reduces to

$$\frac{\rho_2}{\rho_1} = \frac{u_1}{u_2} = \frac{\gamma+1}{\gamma-1}. \tag{1.27}$$

For a monatomic gas, where $\gamma = 5/3$, this gives a maximum compression of 4.

This compression is not high enough for inertial confinement fusion where to achieve the ρR required, as discussed in section 1.3.6, compression to ∼5000 times solid density is required. Isentropic compression, where the entropy is kept constant, effectively equates to an infinite number of shocks of infinitesimal strength. While true isentropic compression cannot be achieved on ICF timescales, a close approximation can be achieved by driving a series of shocks into the target. In ICF much of the compression is achieved as the implosion stagnates, and the imploding material comes to rest.

In ICF radiation transport plays a role in determining the nature of the shock front. In classical shocks, where radiation can be neglected, there are sharp discontinuities in the fluid variables across the shock front. However, at high temperatures, the radiative energy carried away from the shock front can be significant, with the radiation energy flux proportional to T^4. Since the radiation can travel faster than the sound speed in the plasma, the region directly in front of the shock is heated. For extremely strong shock waves this can act to completely smooth the discontinuity that would occur classically [34].

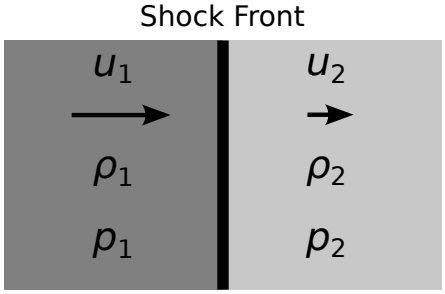

Figure 1.8: An illustration of the convention used across a shock front. The values on the left refer to the pre-shock fluid for velocity, density and pressure, and on the right the post-shock fluid.

1.5 Fast Ignition

Fast Ignition (FI) is a concept that has gained popularity relatively recently, due to the availability of petawatt power lasers through new techniques such as optical parametric chirped pulsed amplification [35]. The fuel is initially compressed, in a similar way to the methods used for ICF, but without the requirement to produce the central hotspot. The ignition of the fuel is instead provided by an external trigger. The initial scheme proposed by Tabak *et al.* [36] proposed an igniter laser pulse with an intensity of $\sim 10^{19}$ W cm^{-2} to create an ignition 'spark' in the fuel, via hot electrons. The imploded core would be compressed and heated in a similar way to that for direct drive, however the requirement for the peak density is relaxed.

The ignitor laser bores a hole up to $\sim$100 times the relativistic critical density in the plasma (see section 1.5.1), and at the tip of this channel generates high energy electrons. These electrons propagate into the core of the imploded fuel and provide the heating in the DT fuel, causing a small region to be heated to ignition temperatures. This then starts a burn-wave that propagates into the rest of the fuel. Central hotspot ignition, as described in section 1.3.1, is known as isobaric, as the pressure is approximately constant between the cold dense fuel and the low density hotspot. FI is closer to being isochoric, with the pressure in the centre of the fuel being much higher than the cold fuel surrounding it, at the point of ignition.

Hole boring fast ignition does have some complications however, the laser boring into the plasma above critical density is prone to filamentation instabilities, and the electrons are slowed by anomalous stopping in the overdense regions [37]. One way to avoid the need for the laser to bore a hole through the plasma, and give the igniter laser a clean path to the centre of the fuel, is to insert a cone into the initial fuel capsule [38]. This process is illustrated in figure 1.9. To begin with the fuel is compressed in the same way as it would be in ICF. The igniter laser is then fired into the cone at the point of peak compression, and this generates hot (relativistic) electrons at the cone tip. These hot electrons propagate into the fuel, heating a small region of the core to the temperature required for ignition. The earliest FI experiments showed promise for cone-guided FI, with a thousand-fold increase in the neutron yields observed with the use of the igniter laser, compared with the same target where only the compression beams were fired [39, 40].

Electrons are not the only option for providing the heating in fast ignition. A proton beam, generated at the rear surface of a foil target irradiated by a laser, can be used to heat the core of the target to ignition temperatures [41, 42]. The foil target to generate the protons could be placed in a cone, allowing a path for the igniter laser in a similar way as for electron driven fast ignition, as shown in the box in figure 1.9. Proton fast ignition could offer an alternative should electron generation and transport issues prove to be a significant problem.

Shock ignition may also offer another route to achieving ignition in a non-isobaric target [43]. The target would be similar to a standard direct drive target, as shown in figure 1.2. It is compressed by laser driven ablation in a similar way to conventional direct drive, but with a slower implosion velocity. This means the target is compressed efficiently, but not to such a high temperature as for standard ICF. As the fuel reaches the maximum compression a shock is driven into the fuel by a short spike in the driver energy, $\sim$200 ps long and at an intensity of 10^{16} W cm^{-2}. This shock converges in the centre of the fuel, providing the ignition heating.

The potential advantage of FI over conventional ICF is the possible reduction in laser driver energy required. The Rayleigh-Taylor instabilities described in section 1.3.3 also become less of an issue, as the pressures generated as the fuel is compressed are not as high as in central hotspot ignition [44].

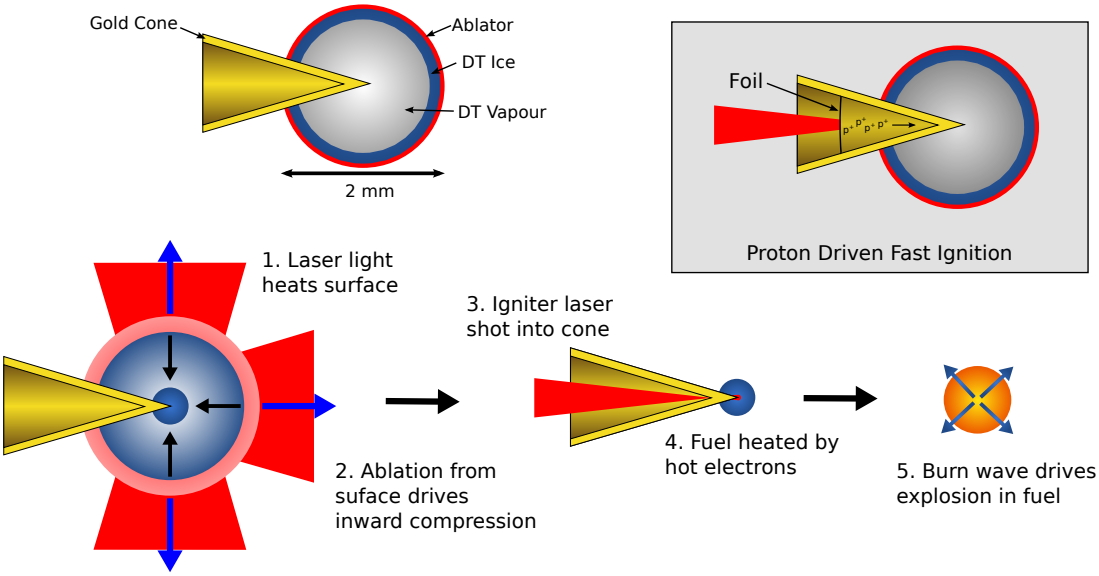

Figure 1.9: The compression and ignition process in re-entrant cone-guided fast ignition. The initial capsule is similar to that shown in figure 1.2. The box shows a target that could be used for proton driven fast ignition.

1.5.1 Relativistic Effects at High Intensities

A useful parameter to describe the intensity of a focused laser is the normalised vector potential, given by

$$a_0 = \frac{eE_0}{m_e c\omega}, \tag{1.28}$$

where E_0 is the peak amplitude of the electric field and ω is the angular frequency of the electric field. For $a_0 \ll 1$ the electron quiver velocity in the electric field of the laser is much less than the speed of light, but for $a_0 \gtrsim 1$ the electron motion is relativistic, and a correction to the critical frequency, as discussed in section 1.3.2, needs to be applied. More conveniently the normalised vector potential for linearly polarised light is expressed as

$$a_0 \sim 0.85 \left(I_{18}\lambda^2_{L\mu m}\right)^{1/2}, \tag{1.29}$$

where I_{18} is the intensity of the laser in units of 10^{18} W cm^{-2} and $\lambda_{L\mu m}$ is the wavelength of the laser light in micrometres.

At values of the normalised vector potential above unity the critical density of the plasma increases, an effect known as relativistically induced transparency [45]. The relativistic critical density is given by $n_{c,\gamma} = \gamma n_c$, where $\gamma = \sqrt{1 + a_0^2/2}$ for linearly polarised light. For example, at an intensity of 10^{21} W cm^{-2} the relativistically induced transparency means the effective critical density is 20 times higher than for the non-relativistic case.

1.5.2 Fast Electron Generation and Transport

The energy of the electrons generated in fast ignition needs to be controlled, as the electrons need to deposit their energy in a small volume of the DT fuel, else much of the igniter laser energy will be wasted. If the electron beam is spread out over a large area by the time it reaches the core of the fuel, or the electrons have too much energy to stop, then sufficient temperatures will not be achieved. The energy of the electrons generated by the ponderomotive force is given by the formula

$$u_e = 0.511 \left(\sqrt{1 + \frac{I_{18} \lambda_{L\mu m}^2}{1.37}} - 1 \right) \text{MeV}, \tag{1.30}$$

where u_e is the velocity or kinetic energy of the electrons in MeV [16]. Experiments have shown that this value from the ponderomotive force overestimates the hot electron energy at high temperatures, and a better scaling is given by

$$u_e = 0.215 \left(I_{18} \lambda_{L\mu m}^2 \right)^{\frac{1}{3}} \text{MeV}, \tag{1.31}$$

which has been found to be valid for laser intensities above 10^{18} W cm^{-2} [46].

The transport of laser produced electrons in solid targets is discussed in detail in [47]. The scale length over which the electrons travel is given by

$$z = 5.9 \ (I_{18})^{-1/3} \left(\frac{T_p}{100 \text{ eV}} \right)^{3/2} \left(\frac{Z}{13} \right)^{-1} \mu\text{m}, \tag{1.32}$$

where z is the scale length in µm, T_p the temperature of the background plasma, Z the atomic number of the ions in the plasma and I_{18} the intensity of the laser in units of 10^{18} W cm^{-2}. The scaling of interest in this equation is the dependence

on the scale length with laser intensity, $z \propto I^{-1/3}$. This formula uses the Beg scaling for the hot electron generation, as in equation 1.31.

Equation 1.32 assumes that form of the resistivity in the plasma is Spitzer-Härm, which will be further discussed in section 2.4.4. Here the penetration depth is restricted by more than just the collisional stopping length, which is further discussed in section 2.4.3. Essentially in this situation the background plasma is unable to provide sufficient electrons to balance the fast electron current produced by the laser. The return current carried by the background plasma is further discussed in section 3.1.

The divergence angle of the electrons is also important, if the angle is too large the electrons will heat the dense fuel inefficiently. There are a number of factors that affect the divergence of the electrons, such as the laser intensity [48], the structure of the target being hit by the laser [49], the plasma density scale length [50] and the electric and magnetic fields generated in the target [51, 52].

1.6 Summary and Thesis Outline

The generation and transport of fast electrons is one of the main outstanding physics issues in fast ignition. It is essential to have efficient heating of the hotspot in the imploded fuel, which requires a good understanding of both the generation and the transport the fast electrons in the target. The effect of a high current density electron beam on a background plasma, such as that in fast ignition, is a problem that has not been widely considered. Current densities of this magnitude will impart significant amounts of energy to the background plasma they are passing through, and significant magnetohydrodynamic evolution of the plasma may occur. Furthermore, the amount of energy which a laser would couple to electrons via a gold cone is not well understood. The energy of the individual electrons needs to be restricted, such that they will be stopped and heat the fuel. Further understanding these two areas is the focus of this thesis.

In **Chapter 2** the equations used to understand the behaviour of a plasma are introduced, resulting in the magnetohydrodynamic equations. In **Chapter 3** an analytic model is derived, starting from the magnetohydrodynamic equations, to understand the effect of a fast electron current on a background plasma. The

results of this are compared to a numerical magnetohydrodynamic simulation developed to study the problem further. In **Chapter 4** an experiment is described which sought to better understand the coupling of the laser energy into fast electrons, via a gold cone. Finally, **Chapter 5** provides the summary and conclusions of the thesis.

Chapter 2

Magnetohydrodynamics

The basic equation of motion for a charged particle in an electromagnetic field is given by the Lorentz force,

$$\boldsymbol{F} = q\left(\boldsymbol{E} + \boldsymbol{v} \times \boldsymbol{B}\right), \tag{2.1}$$

where $\boldsymbol{E}$ and $\boldsymbol{B}$ are the electric and magnetic fields respectively, q the charge on the particle and $\boldsymbol{v}$ the velocity of the particle. However, knowing the motion of individual particles is only useful in certain problems. Plasmas consist of N particles that interact in self-consistent fields, and N is typically extremely large, so a description that is more tractable is typically needed. Under certain conditions, the description can be reduced to a set of macroscopic fluid variables. These are the density, pressure, velocity and the electric and magnetic fields in the plasma. In this chapter the necessary background material will be provided, to show how the magnetohydrodynamic (MHD) equations emerge from basic principles. Some of the energy transport effects in the plasma are also described. Finally methods to solve the equations analytically are discussed.

2.1 Maxwell's Equations

Maxwell's equations [53] provide a description of the dynamical evolution of the electric and magnetic fields in the plasma, and relate the rate of change of the fields to the particles contained within them. Gauss's law relates the electric

field flux through a closed surface to the electrostatic charges contained within, and is given by

$$\nabla \cdot \boldsymbol{E} = \frac{\rho_q}{\epsilon_0}, \tag{2.2}$$

where $\rho_q = \sum_s n_s q_s$, that is to say the charge density, summing over all species s, and ϵ_0 is the permittivity of free space. The electric field is related to the electric potential by $\boldsymbol{E} = -\nabla\phi$, such that $\nabla \cdot \boldsymbol{E} = -\nabla^2\phi$. Gauss's law for the magnetic field similarly relates the magnetic flux through a closed surface to the charges within and is given by

$$\nabla \cdot \boldsymbol{B} = 0, \tag{2.3}$$

which sates that the magnetic flux through any closed surface is zero. Faraday's law describes the induction of an electric field from a time varying magnetic field,

$$\nabla \times \boldsymbol{E} = -\frac{\partial \boldsymbol{B}}{\partial t}. \tag{2.4}$$

Finally Ampère's law describes the magnetic field due to an electric current and is given by

$$\nabla \times \boldsymbol{B} = \mu_0 \boldsymbol{J} + \mu_0 \epsilon_0 \frac{\partial \boldsymbol{E}}{\partial t}, \tag{2.5}$$

where $\boldsymbol{J}_s = \sum_s n_s q_s \boldsymbol{v}_s$, the electric charge current density and μ_0 is the permeability of free space. The final term was not part of Ampère's original law, but was added by Maxwell, and is known as the displacement current. These four equations, along with the Lorentz force in equation 2.1, describe the electrodynamics of the plasma.

2.2 Debye Screening

If a single charged particle in a plasma is considered it will attract and repel other charged particles in its vicinity. At large distances from the charged particle the collective movement of the other particles acts to attenuate its electric field. This is known as Debye screening [54, 55], and the distance over which this occurs

is known as the Debye length. To determine this value the electric potential on a test particle is considered. The density distribution of electrons is given by the Boltzmann distribution,

$$n_e(r) = n_0 e^{-\frac{q_e \phi(r)}{k_B T}}, \tag{2.6}$$

where $n_e(r)$ is the electron density at a distance r from the test charge, $n_0 = Z n_i$ the average electron number density, $q_e = -e$ the charge on an electron, $\phi(r)$ the electric potential due to the test charge, and $k_B T$ the thermal energy in the plasma. The electric potential satisfies Gauss's law, as shown in equation 2.2,

$$\nabla^2 \phi = -\frac{\rho_q}{\epsilon_0} = -\frac{e}{\epsilon_0}\left(n_0 - n_0 e^{\frac{e\phi}{k_B T}}\right). \tag{2.7}$$

Poisson's equation in spherical co-ordinates is given by

$$\nabla^2 \phi = \frac{1}{r^2}\frac{\partial}{\partial r}\left(r^2 \frac{\partial \phi}{\partial r}\right), \tag{2.8}$$

assuming spherical symmetry. Assuming that the thermal energy is much greater than the electric potential energy, that is $e\phi \ll k_B T$, a Taylor expansion can be performed giving

$$e^{\frac{e\phi}{k_B T}} \approx 1 + \frac{e\phi}{k_B T}. \tag{2.9}$$

Putting this together, the resulting equation is given by

$$\frac{1}{r^2}\frac{\partial}{\partial r}\left(r^2 \frac{\partial \phi}{\partial r}\right) = \frac{n_0 e^2}{\epsilon_0 k_B T}\phi, \tag{2.10}$$

with the boundary conditions

$$\begin{aligned} &\phi(r) \to 0 && \text{as } r \to \infty \\ &\phi(r) \to \tfrac{q}{4\pi\epsilon_0 r} && \text{as } r \to 0. \end{aligned} \tag{2.11}$$

The solution to this equation is given by

$$\phi(r) = \frac{q}{4\pi\epsilon_0 r} e^{-r/\lambda_d}, \tag{2.12}$$

where q is the charge on the test particle and λ_d is the Debye length, given by

$$\lambda_d = \sqrt{\frac{\epsilon_0 k_B T}{n_0 e^2}}. \tag{2.13}$$

At distances beyond this length the potential of the particle is effectively screened. This means collisions in the plasma are only due to particles within a sphere surrounding the particle with a radius given by the Debye length, and the number of charged particles within this would be $\sim n_0 \lambda_d^3$.

2.3 The Boltzmann and Vlasov Equations

To understand the behaviour of the plasma, a collection of particles are considered, without interactions, with a distribution given by $f(\boldsymbol{x}, \boldsymbol{v}, t)$. Here $\boldsymbol{x} = x_1, x_2...$ and $\boldsymbol{v} = v_1, v_2...$, depending on the number of dimensions being considered. The evolution of such a species of particles is described by the collisionless Boltzmann equation [56]

$$\frac{\partial f}{\partial t} + \boldsymbol{v} \cdot \nabla f + \frac{\boldsymbol{F}}{m} \cdot \nabla_v f = 0, \tag{2.14}$$

where $\boldsymbol{F}$ is an external force acting on the particles, and $\nabla_v = \partial / \partial \boldsymbol{v}$. This equation is obtained only by making the assumption that the particles are conserved, such that the rate of change in a phase-space volume, given by $\mathrm{d}^3\boldsymbol{x}$ $\mathrm{d}^3\boldsymbol{v}$, is equal to the flux of particles into that volume [57, 58]. Simplifications have been made to the equation, by noting that x_j and v_j are independent of each other, and that the force, F_j, is independent of the velocity, v_j.

Equation 2.1 describes the forces the charged particles in a plasma are subjected too. Adding this term in to the collisionless Boltzmann equation yields the Vlasov equation [59]

$$\frac{\partial f}{\partial t} + \boldsymbol{v} \cdot \nabla f + \frac{q}{m} (\boldsymbol{E} + \boldsymbol{v} \times \boldsymbol{B}) \cdot \nabla_v f = 0. \tag{2.15}$$

Here only the long range fields $\boldsymbol{E}$ and $\boldsymbol{B}$ have been considered, not the fields within the Debye sphere. The force has a dependence on the velocity, but the cross product ensures that x_1 is not dependent on v_1 and so on.

As established in section 2.2, the particles in a plasma will also experience the electric potential of particles within the Debye sphere, which leads to electrostatic (Coulomb) collisions between these local particles. Adding a general collision term into equation 2.15 gives

$$\frac{\partial f}{\partial t} + \boldsymbol{v} \cdot \nabla f + \frac{q}{m} (\boldsymbol{E} + \boldsymbol{v} \times \boldsymbol{B}) \cdot \nabla_v f = \left(\frac{\partial f}{\partial t} \right)_{coll}, \tag{2.16}$$

where the collisions given by $(\partial f/\partial t)_{coll}$ are usually given by the Fokker-Planck equation [57]. The Fokker-Planck collision term takes the form

$$\left(\frac{\partial f}{\partial t} \right)_{coll} = -\nabla_v \cdot \left(\left\langle \frac{\Delta \boldsymbol{v}}{\Delta t} \right\rangle \right) + \frac{1}{2} \nabla_v \nabla_v : \left(\left\langle \frac{\Delta \boldsymbol{v} \Delta \boldsymbol{v}}{\Delta t} \right\rangle f \right), \tag{2.17}$$

where : is the scalar tensor product, and a test particle is gaining a velocity $\Delta \boldsymbol{v}$ in a time Δt [60]. This term in equation 2.16 yields the Vlasov-Fokker-Planck equation.

The first term in the Fokker-Planck equation, $\langle \Delta \boldsymbol{v}/\Delta t \rangle$ is known as the dynamical friction vector. This describes the frictional force, which decelerates fast particles and accelerates slow particles, and the term $-\nabla_v$ suggests the distribution in velocity space will narrow. The second term, $\langle \Delta \boldsymbol{v} \Delta \boldsymbol{v}/\Delta t \rangle$, is known as the diffusion tensor. The $\nabla_v \nabla_v$ term describes the diffusion of the distribution in velocity space, that is to say a broadening of the distribution. These two terms will balance for a distribution in equilibrium, with the equilibrium solution being a Maxwellian, as would be expected. Collisions in the plasma lead to effects such as resistivity and thermal conductivity, and are discussed further in section 2.4.3.

2.3.1 Moments of the Vlasov Equation

The distribution given by $f(\boldsymbol{x}, \boldsymbol{v}, t)$ needs to be related to the real physical quantities that are usually of interest in the plasma. For example density is

given by integrating the distribution function over velocity space,

$$n\left(\boldsymbol{x},t\right)=\int f\left(\boldsymbol{x},\boldsymbol{v},t\right)\mathrm{d}^{3}\boldsymbol{v}. \tag{2.18}$$

Similarly the velocity of the fluid is given by integrating $\boldsymbol{v}f$, and averaging over the particles,

$$\boldsymbol{u}(x,t)=\frac{\int \boldsymbol{v}f\left(\boldsymbol{x},\boldsymbol{v},t\right)\mathrm{d}^{3}\boldsymbol{v}}{\int f\left(\boldsymbol{x},\boldsymbol{v},t\right)\mathrm{d}^{3}\boldsymbol{v}}=\frac{1}{n}\int \boldsymbol{v}f\left(\boldsymbol{x},\boldsymbol{v},t\right)\mathrm{d}^{3}\boldsymbol{v}. \tag{2.19}$$

To obtain the fluid equations from the Vlasov equation, equation 2.15, the Vlasov equation is multiplied by powers of $\boldsymbol{v}$, and then integrated over all velocity space. These yield the fluid equations for the density, the velocity (or momentum) and the energy (or pressure, or temperature). The equations derived in this section will all apply to a single species of particles, for example ions or electrons, as opposed to the plasma as a whole.

2.3.2 Zeroth Order Moment

The zeroth order moment is given by multiplying the Vlasov equation by $\boldsymbol{v}^{0}$,

$$\begin{aligned}\int\frac{\partial f}{\partial t}\mathrm{d}^{3}\boldsymbol{v}+\int\boldsymbol{v}\cdot\nabla f\mathrm{d}^{3}\boldsymbol{v}+\frac{q}{m}\int\left(\boldsymbol{E}+\boldsymbol{v}\times\boldsymbol{B}\right)\cdot\nabla_{v}f\mathrm{d}^{3}\boldsymbol{v}=\\ \int\left(\frac{\partial f}{\partial t}\right)_{coll}\mathrm{d}^{3}\boldsymbol{v}.\end{aligned} \tag{2.20}$$

The terms in $\boldsymbol{E}$ and $\boldsymbol{B}$ disappear by the application of Gauss's theorem. As the surface integral goes to infinity the velocity quickly falls to zero. The term in the collisions also disappears since the total number of particles remains constant over time. Hence only the first and second terms remain, which yield

$$\frac{\partial}{\partial t}\int f\mathrm{d}^{3}\boldsymbol{v}+\nabla\cdot\int\boldsymbol{v}f\mathrm{d}^{3}\boldsymbol{v}=0. \tag{2.21}$$

Using equation 2.18 for the fluid density and equation 2.19 for the fluid velocity

gives

$$\frac{\partial n}{\partial t} + \nabla \cdot (n\boldsymbol{u}) = 0, \tag{2.22}$$

which is known as the continuity equation. This equation essentially states that the total number of particles is conserved. It can be rewritten as a mass or charge conservation equation by multiplying by the appropriate value for the particles concerned.

2.3.3 First Order Moment

Next the Vlasov equation is multiplied by the first order moment, $m\boldsymbol{v}$, to obtain the momentum equation

$$m\int \boldsymbol{v}\frac{\partial f}{\partial t}\mathrm{d}^3\boldsymbol{v} + m\int \boldsymbol{v}\left(\boldsymbol{v}\cdot\nabla f\right)\mathrm{d}^3\boldsymbol{v} + q\int \boldsymbol{v}\left(\boldsymbol{E}+\boldsymbol{v}\times\boldsymbol{B}\right)\cdot\nabla_v f\mathrm{d}^3\boldsymbol{v} = m\int \boldsymbol{v}\left(\frac{\partial f}{\partial t}\right)_{coll}\mathrm{d}^3\boldsymbol{v}, \tag{2.23}$$

where products such as $\boldsymbol{ab}$ are the vector direct product ($a_j b_k$ in Cartesian tensor notation). Similar arguments to those made in obtaining the zeroth order moment can be used, and the equation yields

$$mn\left(\frac{\partial \boldsymbol{u}}{\partial t} + \left(\boldsymbol{u}\cdot\nabla\right)\boldsymbol{u}\right) = qn\left(\boldsymbol{E}+\boldsymbol{u}\times\boldsymbol{B}\right) - \nabla\cdot\overleftrightarrow{\boldsymbol{P}} + \frac{\partial \boldsymbol{p}_{sr}}{\partial t}. \tag{2.24}$$

Further simplifications to the equation have been made using the continuity equation, equation 2.22. This essentially leads to a momentum equation for each dimension being considered.

The tensor $\overleftrightarrow{\boldsymbol{P}}$ is the pressure tensor, with the elements given by p_{jk}. This comes about by separating the particle velocity $\boldsymbol{v}$ into the fluid velocity $\boldsymbol{u}$ and a thermal velocity. The thermal velocity then leads to the pressure term. The diagonal elements of the tensor, where $j = k$, are pressure forces, while the off diagonal values, $j \neq k$, are viscous terms. No consideration of the viscous forces

is normally required in plasmas, such that $p_{jk} = 0$ for $j \neq k$. Isotropy can often be assumed, so the pressure terms are equal, such that $p_{jj} = p_{kk} \; \forall \; j, k$. Hence the pressure tensor can be taken more simply as a scalar p, where $p = p_{jj}$.

The final term, $\partial \boldsymbol{p}_{sr}/\partial t$ represents the change in momentum in the species s due to collisions with a species r in the plasma. Collisions between the same species do not produce a net change in momentum in that species. This term will be revisited in section 2.4.1. The precise form of the collisions is not important in obtaining the basic form of the MHD equations, however note that $\partial \boldsymbol{p}_{sr}/\partial t = -\partial \boldsymbol{p}_{rs}/\partial t$.

2.3.4 Second Order Moment

Finally, for the second order moment, the Vlasov equation is multiplied through by $mv^2/2$ to yield

$$\begin{aligned} \frac{m}{2}\int v^2 \frac{\partial f}{\partial t} \mathrm{d}^3\boldsymbol{v} + \frac{m}{2}\int v^2 \left(\boldsymbol{v}\cdot\nabla f\right) \mathrm{d}^3\boldsymbol{v} + \\ \frac{q}{2}\int v^2 \left(\boldsymbol{E} + \boldsymbol{v}\times\boldsymbol{B}\right)\cdot\nabla_v f \mathrm{d}^3\boldsymbol{v} = \frac{m}{2}\int v^2 \left(\frac{\partial f}{\partial t}\right)_c \mathrm{d}^3\boldsymbol{v}. \end{aligned} \tag{2.25}$$

Once again similar treatment is applied to obtain the energy equation. There are numerous ways to present the solution to this equation, the simplest statement yielding

$$\frac{\mathrm{d}}{\mathrm{d}t}\left(\frac{p}{\rho^\gamma}\right) = 0, \tag{2.26}$$

where γ is the adiabatic index or ratio of specific heats, introduced in section 1.4. Alternatively, for more direct comparison to equations 2.22 and 2.24, the energy equation can be written as

$$\frac{\partial e}{\partial t} + \boldsymbol{u}\cdot\nabla e + p\nabla\cdot\boldsymbol{u} = S, \tag{2.27}$$

where e is the sum of the the kinetic and thermal energies of the particles. The third term on the left hand side represents the pdV work done on the plasma. The term S is a collection of energy source and sink terms, the exact form of which is

dependent on the physics that needs to be considered for a particular problem. It can include terms such as external Ohmic heating, losses and gains from thermal conductivity, bremsstrahlung radiation losses, energy exchange between particle species due to collisions and energy from fusion produced particles [5]. These terms are described in later sections in this chapter.

2.4 The MHD Equations

In this section it will be shown how the fluid equations for the ions and electrons, derived from the moments of the Vlasov equation, lead to the magnetohydrodynamic equations. An important aspect in fast ignition is the resistivity of the plasma, and the resistive form of the MHD equations is derived later in this section. First however the ideal MHD equations are considered, where resistivity arising from the collisional term in the Vlasov-Fokker-Planck equation, equation 2.16, is neglected.

2.4.1 The Ideal MHD Equations

To obtain the ideal MHD equations, the equations for the ion and electron fluids are used, as derived in the previous section. Some approximations are then made which lead to the fluid equations that, along with Maxwell's equations given in equations 2.2 - 2.5, make up the MHD equations.

The mass density of the plasma is given by

$$\rho = n_i m_i + n_e m_e \approx n_i m_i, \tag{2.28}$$

where the subscripts i and e represent the ions and electrons respectively, and the fact that $m_i \gg m_e$ has been used to make the approximation of the mass density. The fluid velocity in the plasma can be now written as

$$\boldsymbol{v} = \frac{n_i m_i \boldsymbol{u}_i + n_e m_e \boldsymbol{u}_e}{\rho} \approx \frac{n_i m_i \boldsymbol{u}_i + n_e m_e \boldsymbol{u}_e}{n_i m_i} \approx \boldsymbol{u}_i, \tag{2.29}$$

where $\boldsymbol{v}$ is the plasma fluid velocity.

The continuity equation, found from the zeroth order moment of the Vlasov equation, equation 2.22, can now be written as

$$\frac{\partial \rho}{\partial t} + \nabla \cdot (\rho \boldsymbol{v}) = 0. \tag{2.30}$$

This is also known as the conservation of mass equation, which is what it essentially describes.

Next the momentum is considered, as shown in equation 2.24. For the ions the momentum equation is given by

$$m_i n_i \left(\frac{\partial \boldsymbol{u}_i}{\partial t} + (\boldsymbol{u}_i \cdot \nabla) \boldsymbol{u}_i \right) = Z e n_i (\boldsymbol{E} + \boldsymbol{u}_i \times \boldsymbol{B}) - \nabla p_i + \frac{\partial \boldsymbol{p}_{ie}}{\partial t}, \tag{2.31}$$

where the final term is the change in momentum of the ions due to the electrons. Similarly for the electrons

$$m_e n_e \left(\frac{\partial \boldsymbol{u}_e}{\partial t} + (\boldsymbol{u}_e \cdot \nabla) \boldsymbol{u}_e \right) = -e n_e (\boldsymbol{E} + \boldsymbol{u}_e \times \boldsymbol{B}) - \nabla p_e + \frac{\partial \boldsymbol{p}_{ei}}{\partial t}, \tag{2.32}$$

as expected. Adding these terms gives

$$\begin{aligned} \frac{\partial}{\partial t} (m_i n_i \boldsymbol{u}_i + m_e n_e \boldsymbol{u}_e) + m_i n_i (\boldsymbol{u}_i \cdot \nabla) \boldsymbol{u}_i + m_e n_e (\boldsymbol{u}_e \cdot \nabla) \boldsymbol{u}_e = \\ e (Z n_i \boldsymbol{u}_i - n_e \boldsymbol{u}_e) \times \boldsymbol{B} - \nabla (p_i + p_e) + \frac{\partial \boldsymbol{p}_{ie}}{\partial t} + \frac{\partial \boldsymbol{p}_{ei}}{\partial t}. \end{aligned} \tag{2.33}$$

The values of these terms have all been previously established. The first term on the left hand side is given by $\rho \boldsymbol{v}$, from equation 2.29. The third term is small and neglected, while the second term also uses the fact that $\boldsymbol{v} \approx \boldsymbol{u}_i$. The current in the plasma is defined as

$$\boldsymbol{J} = e (Z n_i \boldsymbol{u}_i - n_e \boldsymbol{u}_e) \tag{2.34}$$

and quasi-neutrality is assumed such that $n_e \approx Z n_i$. This results in the first term on the right hand side giving the $\boldsymbol{J} \times \boldsymbol{B}$ force. The overall pressure is simply given

by $p = p_i + p_e$. Finally, as mentioned in section 2.3.3, the collision terms must be equal and opposite, and so they vanish. This yields the momentum equation in the plasma

$$\rho\left(\frac{\partial \boldsymbol{v}}{\partial t} + (\boldsymbol{v}\cdot\nabla)\,\boldsymbol{v}\right) = \boldsymbol{J}\times\boldsymbol{B} - \nabla p. \tag{2.35}$$

Here the forces that act on the plasma, the $\boldsymbol{J}\times\boldsymbol{B}$ force and the pressure gradient, have been established. External forces, such as gravity, could also be included in this equation, if they are relevant to the problem of interest.

Finally the energy equation is considered. Equation 2.26 is used, which for the ions gives

$$\frac{\mathrm{d}}{\mathrm{d}t}\left(\frac{p_i}{\rho^\gamma}\right) = 0 \tag{2.36}$$

and for the electrons

$$\frac{\mathrm{d}}{\mathrm{d}t}\left(\frac{p_e}{\rho^\gamma}\right) = 0. \tag{2.37}$$

Once again using the fact that $p = p_i + p_e$ this simply yields

$$\frac{\mathrm{d}}{\mathrm{d}t}\left(\frac{p}{\rho^\gamma}\right) = 0. \tag{2.38}$$

This again can be written in other forms, such as that shown in equation 2.27.

Maxwell's equations also form part of the set of MHD equations. However, we have assumed quasi-neutrality, hence $\nabla\cdot\boldsymbol{E} = \rho_q/\epsilon_0$ can be neglected, as this will only be significant on length scales smaller than the Debye length. Similarly the displacement current in Ampère's Law, equation 2.5, can be neglected by a consideration of the characteristic scales involved. Taking Ohm's law as

$$\boldsymbol{E} + \boldsymbol{v}\times\boldsymbol{B} = 0 \tag{2.39}$$

then allows Faraday's law and Ohm's law to be written as

$$\frac{\partial \boldsymbol{B}}{\partial t} - \nabla\times(\boldsymbol{v}\times\boldsymbol{B}) = 0. \tag{2.40}$$

This equation for the magnetic field, along with Gauss's law for magnetism, $\nabla \cdot \boldsymbol{B} = 0$, completes the set of ideal MHD equations.

2.4.2 Resistive MHD

A key omission in the previous section, when considering the MHD equations, is the resistivity in the plasma. Here a derivation is given that finds the relationship between the electric field, $\boldsymbol{E}$, and the current density, $\boldsymbol{J}$. A completely rigorous derivation is not possible, as numerous assumptions need to be made, some of which may not always be valid [58].

Going back to the collision term, as introduced in section 2.3.3, the momentum change due to collisions between the species s and r can be written as

$$\frac{\partial \boldsymbol{p}_{sr}}{\partial t} = -\frac{\partial \boldsymbol{p}_{rs}}{\partial t} = -n_s m_s \nu_{sr} \left(\boldsymbol{u}_s - \boldsymbol{u}_r\right), \tag{2.41}$$

where ν_{sr} is the effective collision frequency between the species.

Equations 2.31 and 2.32, the momentum for the ions and electrons respectively are considered. To obtain the momentum equation these two terms were added together. Here they are multiplied by m_e and m_i respectively, and the equation for the electrons is subtracted from that for the ions, giving

$$\begin{aligned} m_i m_e &\left(\frac{\partial}{\partial t}\left(n_i \boldsymbol{u}_i - n_e \boldsymbol{u}_e\right) + \nabla \cdot \left(n_i \boldsymbol{u}_i \boldsymbol{u}_i - n_e \boldsymbol{u}_e \boldsymbol{u}_e\right)\right) \\ &= e\left(m_i n_i + m_e n_e\right)\boldsymbol{E} + e\left(m_e n_i \boldsymbol{u}_i + m_i n_e \boldsymbol{u}_e\right) \times \boldsymbol{B} - m_e \nabla p_i \\ &+ m_i \nabla p_e - m_i m_e n_i \nu_{ie}\left(\boldsymbol{u}_i - \boldsymbol{u}_e\right) + m_i m_e n_e \nu_{ei}\left(\boldsymbol{u}_e - \boldsymbol{u}_i\right). \end{aligned} \tag{2.42}$$

The final two terms here are identifiable as the current density,

$$\begin{aligned} -m_i m_e n_i \nu_{ie}\left(\boldsymbol{u}_i - \boldsymbol{u}_e\right) &+ m_i m_e n_e \nu_{ei}\left(\boldsymbol{u}_e - \boldsymbol{u}_i\right) \\ &= -\frac{m_e \nu_{ei}}{e n_e}\left(n_e\left(Z m_e + m_i\right)\right)\left(Z n_i \boldsymbol{u}_i - n_e \boldsymbol{u}_e\right) \\ &= -e\left(\frac{m_e \nu_{ei}}{n_e e^2}\right)\rho \boldsymbol{J}, \end{aligned} \tag{2.43}$$

where the fact that $m_i\nu_{ie} = m_e\nu_{ei}$ has been used, which follows from equation 2.41.

The full form of Ohm's law now becomes

$$\boldsymbol{E} + \boldsymbol{v} \times \boldsymbol{B} = \eta \boldsymbol{J} + \frac{1}{en_e}\boldsymbol{J} \times \boldsymbol{B} - \frac{1}{en_e}\nabla p_e + \frac{m_e}{n_e e^2}\left(\frac{\partial \boldsymbol{J}}{\partial t} + \nabla \cdot (\boldsymbol{J}\boldsymbol{v} + \boldsymbol{v}\boldsymbol{J})\right), \quad (2.44)$$

where the approximations have again been made that $m_i \gg m_e$ and $\boldsymbol{v} \approx \boldsymbol{u}_i$. The term η is given by

$$\eta = \frac{1}{\sigma} = \frac{m_e \nu_{ei}}{n_e e^2}, \quad (2.45)$$

which can be identified as the resistivity, which is the inverse of the conductivity, σ. The second term on the right hand side is the Hall effect, and the third term is the electric field due to the pressure gradient of the electrons, both of which will drive currents in the plasma. Both of these terms, and the final terms, again when considering the characteristic scales in the system, can usually be neglected [58]. This results in Ohm's law for a resistive plasma in the form

$$\boldsymbol{E} + \boldsymbol{v} \times \boldsymbol{B} = \eta \boldsymbol{J}. \quad (2.46)$$

Due to this, equation 2.40, the MHD equation for the magnetic field, needs to be modified. The resulting growth of the magnetic field, from Faraday's law, equation 2.4, is given by

$$\frac{\partial \boldsymbol{B}}{\partial t} - \nabla \times (\boldsymbol{v} \times \boldsymbol{B}) = -\nabla \times (\eta \boldsymbol{J}), \quad (2.47)$$

which shows that the magnetic field can grow in the system due to a resistive electric current. By taking Ampère's Law, in the form $\nabla \times \boldsymbol{B} = \mu_0 \boldsymbol{J}$, along with Gauss's Law, $\nabla \cdot \boldsymbol{B} = 0$, and the vector identity $\nabla \times (\nabla \times \boldsymbol{A}) = \nabla(\nabla \cdot \boldsymbol{A}) - \nabla^2 \boldsymbol{A}$, the evolution of the magnetic field can be re-written as

$$\frac{\partial \boldsymbol{B}}{\partial t} = \nabla \times (\boldsymbol{v} \times \boldsymbol{B}) + \frac{\eta}{\mu_0}\nabla^2 \boldsymbol{B}. \quad (2.48)$$

Here two distinct terms can be seen on the right hand side. The first, involving

the fluid velocity $\boldsymbol{v}$, is an advective term in the magnetic field. The second term describes the diffusion of the magnetic field. The magnetic Reynolds, R_M, number compares the relative strength of the advection to the diffusion of the magnetic field; it is given by

$$\frac{\frac{\eta}{\mu_0}|\nabla \times (\boldsymbol{v} \times \boldsymbol{B})|}{|\nabla^2 \boldsymbol{B}|} \sim \frac{\mu_0 v L_H}{\eta} = R_M, \tag{2.49}$$

where L_H is the hydrodynamic scale length of the phenomena of interest. If the magnetic Reynolds number goes to infinity, implying either that the resistivity is going to zero or that the scale lengths are becoming very long, then ideal MHD can be used; in this case the diffusive term becomes unimportant [61].

2.4.3 Coulomb Collisions

Coulomb collisions are collisions between the charged particles in the plasma, both due to collisions with different species and collisions between the same species. A Coulomb collision between an electron and an ion is illustrated in figure 2.1. The impact parameter, the distance of closest approach, for a 90° scatter is given by

$$b_0 = \frac{q_s q_r}{4\pi\epsilon_0 \mu_{sr} v^2}, \tag{2.50}$$

where q_s is the charge on species s, v the approach velocity and μ_{sr} the reduced mass given by $\mu_{sr} = m_s m_r/(m_s + m_r)$. The cross-section for a 90° collision is then $\sigma = \pi b_0^2$, with the mean free path given by $\lambda = 1/n\sigma$, where n is the density of the scatterers. This is related to the impact parameter, b, which gives the scattering angle, for an angle θ, as

$$b = \frac{b_0}{\tan\left(\frac{\theta}{2}\right)}. \tag{2.51}$$

Considering small angles, such that $\tan\theta \sim \theta$, a small change in velocity is given by $\Delta\boldsymbol{v}_\perp = 2\boldsymbol{v}b_0/b$. In figure 2.1 it can be seen that $\boldsymbol{v}'$ is defined such that $\boldsymbol{v}' = \boldsymbol{v} + \Delta\boldsymbol{v}_\perp$. Then, considering many such scatters over a distance λ, due to scatterers between a distance b and $b + db$, the number of collisions will be given

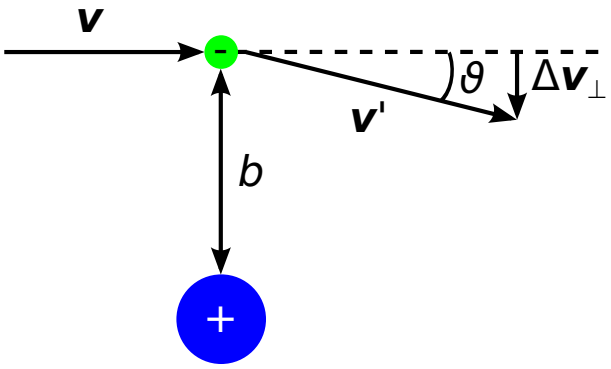

Figure 2.1: An electron-ion scattering collision. b is the distance of closest approach, $\boldsymbol{v}$ and $\boldsymbol{v'}$ the velocity before and after the scatter respectively, and θ is the scattering angle.

by $N = n\lambda 2\pi b\, db$. Given a number of such small scatters, it is found that

$$\sum \Delta v_\perp^2 = \int_{b_{min}}^{b_{max}} \left(\frac{2vb_0}{b}\right)^2 n\lambda 2\pi b\, db \tag{2.52}$$

and hence the mean free path is given by

$$\lambda = \frac{1}{8b_0^2 n\pi \ln\Lambda}, \tag{2.53}$$

where $\ln\Lambda = \ln(b_{max}/b_{min})$. The values of b_{max} and b_{min} need to correspond to the physical range of distances that are relevant. For b_{max} the Debye length, λ_D, is a suitable choice, given in equation 2.13. This was discussed in section 2.2 as the furthest distance over which charged particle interactions need to be considered. A suitable choice for b_{min} would be b_0. When these choices for b_{max} and b_{min} are used $\ln\Lambda$ is known as the Coulomb logarithm. Typical values for this in plasmas of interest are between 5 and 15 [6]. This then means that the effective mean free path due to the small angle collisions, as opposed to the 90° large angle collisions, is around 100 times higher. It is these small angle collisions that are most important to consider in the plasma.

2.4.4 The Spitzer-Härm Resistivity

By considering the small angle collisions between ions and electrons, as described in the previous section, and taking the Fokker-Planck equation, the resistivity in the plasma can be found. Assumptions are made that the ions are stationary, and that the resistivity is only due to electron-ion collisions. The full derivation is not included here, but using these considerations the plasma resistivity is found to be

$$\eta_{\parallel} = \frac{m_e^{1/2} Z e^2 \ln \Lambda}{32\pi^{1/2}\epsilon_0^2 \left(2k_B T_e\right)^{3/2}} \approx 3 \times 10^{-5} \frac{Z \ln \Lambda}{T_{eV}^{3/2}} \ \Omega\text{m}, \tag{2.54}$$

where the symbols all have their previously defined meanings and T_{eV} is the electron temperature in electron volts [62]. $\eta_{\parallel}$ denotes the resistivity parallel to the magnetic field; the perpendicular resistivity is given by $\eta_{\perp} \approx 2\eta_{\parallel}$. This equation can also be used to give a value for the electron-ion collision rate, from equation 2.45 it can be seen that $\nu_{ei} = \eta_{\parallel} n_e e^2 / m_e$. It is interesting to note that equation 2.54 does not have any strong dependence on the density, although it does have a very weak dependence through the Coulomb logarithm, $\ln \Lambda$. This can be thought of in terms of the fact that although there are more charge carriers at higher number densities, the number of collisions will similarly be increased.

The value for the resistivity given by equation 2.54 underestimates the resistivity slightly, due to the fact it does not account for electron-electron collisions. A more complete derivation of the resistivity is given by Spitzer and Härm [63], which does take these interactions into account. The electron-electron collisions act to change the overall distribution function for the population of electrons. The transverse resistivity is then well approximated as [6]

$$\eta_{\perp} = 1.03 \times 10^{-4} \frac{Z \ln \Lambda}{T_{eV}^{3/2}} \ \Omega\text{m}, \tag{2.55}$$

which is usually referred to as the Spitzer-Härm resistivity.

The Spitzer-Härm resistivity is only valid for plasmas that are fully ionised and non-degenerate; that is to say, plasmas at high temperatures and low densities. At solid density the Spitzer-Härm resistivity is valid for temperatures above approximately 100 eV. At temperatures below 10 eV it can overestimate the

true resistivity by an order of magnitude or more. Work by Lee and More [64] has modelled the resistivity in many different regimes, where different effects dominate the calculation.

2.4.5 Thermal Conductivity

So far the thermal conductivity has been neglected, but from Fourier's law it is known that a temperature gradient will lead to a heat flow in any material. Fourier's law is given by

$$\boldsymbol{Q} = -\kappa \nabla T, \tag{2.56}$$

where $\boldsymbol{Q}$ is the heat flux, with units of power per unit area, and κ the coefficient of thermal conductivity.

A straightforward way of analysing the value of the thermal conductivity is given by Boyd and Sanderson [61]. A small perturbation to the Vlasov-Fokker-Planck equation, equation 2.16, is considered in the form $f = f_0 + f_1$. This is linearised to give

$$\boldsymbol{v} \cdot \nabla f_0 = -\nu_{ei} f_1, \tag{2.57}$$

where it has been assumed that electron-ion collisions dominate the heat transfer. Here it has also been assumed that collisions drive the distribution to a Maxwellian, given by f_0, so that the collision term takes the form

$$\left(\frac{\partial f}{\partial t}\right)_{coll} = -\nu_{ei}\left(f - f_0\right) \tag{2.58}$$

and the Maxwellian f_0 is given by

$$f_0 = n(\boldsymbol{x})\left(\frac{m_e}{2\pi k_B T(\boldsymbol{x})}\right)^{3/2} e^{\frac{-mv^2}{2k_B T(\boldsymbol{x})}}. \tag{2.59}$$

Putting these back into equation 2.58 yields

$$f_0 \boldsymbol{v} \cdot \frac{\partial T}{\partial \boldsymbol{x}}\left(\frac{m_e v^2}{2k_B T} - \frac{5}{2T}\right) = -\nu_{ei} f_1. \tag{2.60}$$

The heat flux is given by

$$\boldsymbol{Q} = \int \frac{1}{2} m v^2 \boldsymbol{v} f \mathrm{d}^3 \boldsymbol{v}, \tag{2.61}$$

which leads to

$$\boldsymbol{Q} = -\frac{5 n_e k_B^2 T}{2 m_e \nu_{ei}} \nabla T, \tag{2.62}$$

from which the value for the thermal conductivity, κ, is identified as

$$\kappa = \frac{5 n_e k_B^2 T}{2 m_e \nu_{ei}}. \tag{2.63}$$

The value of resistivity was related to the electron-ion collision frequency in equation 2.45. Carrying this through for the thermal conductivity yields [65]

$$\kappa = 640 \frac{(2\pi)^{1/2} \epsilon_0^2 k_B^{7/2} T_e^{5/2}}{m_e^{1/2} Z e^4 \ln \Lambda} \epsilon \delta_T, \tag{2.64}$$

where ϵ and δ_T are corrections that depend on Z, as discussed by Spitzer [62]. A suitable fit for these values is given by $\epsilon(Z)\delta_T(Z) \approx 0.472\ Z/(Z+4)$ [66]. It can be seen that, as with the resistivity in equation 2.54, the thermal conductivity is independent of the density.

As discussed in section 2.4.4 the form of this in different regimes can have contributions from a large variety of effects. From the use of the collision frequency it can be expected that the electron-electron collisions play a roll, as they did for the resistivity. The previous more detailed calculations of the resistivity by Lee and More [64] also lead to a similarly more detailed calculation of the thermal conductivity. The coefficients are in fact linked by the equation

$$\beta = \alpha T + \frac{5 \kappa T}{2 e \eta}, \tag{2.65}$$

where the term α is an addition to the current density $\boldsymbol{J}$ in the form $\alpha \nabla T$ and the term β is an addition to the heat flow $\boldsymbol{Q}$ in the form $-\beta \boldsymbol{E}$ [62]. In other words, a temperature gradient causes an electric current, and an electric field causes a heat flow.

2.4.6 Ohmic Heating

Ohmic heating describes the heating of a plasma via electrons being driven by an electric field, as they collide with the ions [5]. Taking equations 2.31 and 2.32, the momentum equations for the ions and electrons respectively, and the collision term given in equation 2.41, gives

$$m_i \frac{\partial \boldsymbol{u}_i}{\partial t} + \boldsymbol{u}_i \cdot \nabla \boldsymbol{u}_i = ZeE + m_e \nu_{ei} \left(\boldsymbol{u}_e - \boldsymbol{u}_i \right) \tag{2.66}$$

for the ions and

$$m_e \frac{\partial \boldsymbol{u}_e}{\partial t} + \boldsymbol{u}_e \cdot \nabla \boldsymbol{u}_e = eE - m_e \nu_{ei} \left(\boldsymbol{u}_e - \boldsymbol{u}_i \right) \tag{2.67}$$

for the electrons. Here the magnetic field is neglected and the density is considered to be uniform. The solution to these equations are given by

$$u_i = \frac{ZeE}{m_i \nu_{ei}} \left(1 - e^{\nu_{ei} t} \right) \rightarrow \frac{ZeE}{m_i \nu_{ei}} \tag{2.68}$$

for the ions and

$$u_e = -\frac{eE}{m_e \nu_{ei}} \left(1 - e^{\nu_{ei} t} \right) \rightarrow -\frac{eE}{m_e \nu_{ei}} \tag{2.69}$$

for the electrons. This solution corresponds to a large t; that is to stay a steady state. These solutions also assume $m_i \gg m_e$. The power density delivered to the electrons is given by the force multiplied by the fluid velocity

$$\frac{\partial e}{\partial t} = -eE u_e n_e. \tag{2.70}$$

When instead considering the energy going to the ions, the result is reduced by a factor of m_e/m_i. As only the electrons are considered, the current density is given by $J \approx -e n_e u_e$, and it follows that

$$\frac{\partial e}{\partial t} = m_e n_e \nu_{ei}^2 = \frac{m_e \nu_{ei}}{e^2 n_e} J^2 = \eta J^2. \tag{2.71}$$

The resistivity has been identified using equation 2.45, and the value of the resistivity was considered in section 2.4.4.

2.4.7 Other Energy Transport

Two other energy transport effects were mentioned in section 2.3.4, the bremsstrahlung radiation losses and fusion energy particle heating. The bremsstrahlung radiation power loss was given in equation 1.12. This mechanism is closely related to the inverse bremsstrahlung absorption discussed in section 1.3.2. Here however the electrons emit radiation as they undergo collisions with ions, losing energy in the process. Similar power loss from the ions is negligible [5]. The power from fusion born α-particles in a DT plasma was given in equation 1.13. At temperatures below 100 keV the majority of the α-particle energy loss, as they slow down, is due to collisions with the electrons [8, 33].

2.4.8 Two Temperature Hydrodynamics

When considering laser driven plasmas the electron and ion temperatures can be significantly different. In such a case it may be preferable to treat the electrons and ions as with distinct temperatures.

Similar assumptions are made as previously in this chapter, namely that $\rho \approx \rho_i$, $n_i = Zn_e$ and that $\boldsymbol{v} \approx \boldsymbol{u}_i$. The equations obtained for the hydrodynamics of the system are then given by:

$$\frac{\partial \rho}{\partial t} + \nabla \cdot (\rho \boldsymbol{v}) = 0 \tag{2.72}$$

$$\rho \left(\frac{\partial \boldsymbol{v}}{\partial t} + \boldsymbol{v} \cdot \nabla \boldsymbol{v} \right) + \nabla \cdot (\rho \boldsymbol{v}) = 0 \tag{2.73}$$

$$\frac{\partial e_i}{\partial t} + \nabla \cdot \left((e_i + p_i) \, \boldsymbol{v} \right) = -\boldsymbol{v} \cdot \nabla p_e \tag{2.74}$$

$$\frac{\partial e_e}{\partial t} + \nabla \cdot (e_e \boldsymbol{v}) = \boldsymbol{v} \cdot \nabla p_e \tag{2.75}$$

for the mass continuity, momentum, ion energy and electron energy respectively. The energy density, e_i, is given by

$$e_i = \frac{p_i}{\gamma - 1} + \frac{1}{2} \rho_i |\boldsymbol{v}|^2 \tag{2.76}$$

and similarly for the electron energy, e_e, with $\rho_e = n_e m_e$. The only difference here from the standard hydrodynamic equations is that the electrons and ions have been allowed to have different temperatures.

Over some timescale the electrons and ions will reach equilibrium with one another. This can be expressed as

$$\frac{\partial T_i}{\partial t} = \frac{T_e - T_i}{\tau_{ie}} \tag{2.77}$$

for the ions, and similarly for the electrons. The equilibration time is discussed by Spitzer in references [67] and [62]. Here the equilibration time was found to be given by

$$\tau_{ie} = \frac{3(2\pi)^{3/2} m_i m_e \epsilon_0^2 k_B^{3/2}}{2 n_i Z^2 e^4 \ln\Lambda} \left(\frac{T_e}{m_e} + \frac{T_i}{m_i} \right)^{3/2} \tag{2.78}$$

for the ion-electron equilibration. Similarly, for the electron-ion equilibration it is apparent that

$$\tau_{ie} = \frac{n_i}{n_e} \tau_{ei} = \frac{\tau_{ei}}{Z}. \tag{2.79}$$

An approach to solving this numerically is discussed in section 2.5.5.

2.5 Numerical Methods for Solving the Ideal MHD Equations

The formulation of the MHD equations given so far is known as the Eulerian form, where the behaviour of the fluid is considered in the laboratory rest frame. Another approach is to a Lagrangian form, where the observer moves with the fluid flow. In the Eulerian approach the grid is fixed, and the fluid quantities in each cell are evolved at each time step. Conversely, in the Lagrangian approach the cell boundaries will move, causing more complexity when considering more than one dimension.

2.5.1 The Conservative Form of the MHD Equations

The general kind of problem that needs to be solved when considering the ideal MHD equations is one of the form

$$\frac{\partial \boldsymbol{u}}{\partial t} + \nabla \cdot g(\boldsymbol{u}) = 0. \tag{2.80}$$

The ideal MHD equations, as discussed in the previous section, can be re-written in this form. These are given by

$$\frac{\partial \rho}{\partial t} + \nabla \cdot (\rho \boldsymbol{v}) = 0 \tag{2.81}$$

for the continuity equation, identical to that in equation 2.30. Next

$$\frac{\partial (\rho \boldsymbol{v})}{\partial t} + \nabla \cdot \left(\rho \boldsymbol{v}\boldsymbol{v} + \left(p + \frac{1}{2\mu_0} |\boldsymbol{B}|^2 \right) I - \frac{1}{\mu_0} \boldsymbol{B}\boldsymbol{B} \right) = 0 \tag{2.82}$$

is the momentum equation, rewritten from equation 2.35. Then

$$\frac{\partial e}{\partial t} + \nabla \cdot \left(\left(e + p + \frac{1}{2\mu_0} |\boldsymbol{B}|^2 \right) \boldsymbol{v} - \frac{1}{\mu_0} (\boldsymbol{v} \cdot \boldsymbol{B}) \boldsymbol{B} \right) = 0 \tag{2.83}$$

is the energy equation, including the magnetic field, which comes from equation 2.38 (although it bears more obvious similarity to equation 2.27, with the inclusion of the magnetic field in the energy density, as given in equation 2.85). Finally

$$\frac{\partial \boldsymbol{B}}{\partial t} - \nabla \times (\boldsymbol{v} \times \boldsymbol{B}) = 0 \tag{2.84}$$

is the advection equation for the magnetic field. The constraint $\nabla \cdot \boldsymbol{B} = 0$ is also needed for completeness, and the equation of state for an ideal gas gives the energy density as

$$e = \frac{p}{\gamma - 1} + \frac{1}{2} \rho |\boldsymbol{v}|^2 + \frac{1}{2\mu_0} |\boldsymbol{B}|^2. \tag{2.85}$$

This set of equations make up the ideal MHD equations in conservative form; there are no source or sink terms.

2.5.2 The Riemann Problem

To compare the merits of different approaches to solve the conservative form of MHD equations, as shown in section 2.5.1, it is useful to consider the Riemann problem. The Riemann problem in its simplest form involves two uniform domains, which are discontinuously connected. The MHD equations permit discontinuous solutions, that is to say shocks, which can naturally develop in laser-plasma interactions. Therefore, when solving the MHD equations, a method is needed that can cope with such discontinuities.

A useful example of a Riemann type problem is Sod's shock tube [68]. This defines a problem where in one half of the grid the density and pressure are given by $\rho_L = 1, p_L = 1$ and in the other half they are given by $\rho_R = 0.125, p_R = 0.1$ at $t = 0$. The system is then allowed to evolve freely. A numerical scheme that can properly treat shocks and discontinuities, as they appear in Sod's shock tube, will be useful in considering fast ignition plasmas where shocks can be driven, which will be discussed in chapter 3.

The most straightforward approach to solving an equation of the form of equation 2.80 is to consider the amount fluid flowing into and out of one cell. The quantity of a fluid variable u in that cell at the next timestep is given by

$$u_j^{n+1} = u_j^n - \left(v_{j+\frac{1}{2}}^n u_i^n - v_{j-\frac{1}{2}}^n u_{j-1}^n \right) \frac{\Delta t}{\Delta x} \tag{2.86}$$

if $g(u) = u$ and assuming that $v_{j\pm\frac{1}{2}}^n > 0$, i.e. material is flowing into cell j from the cell $j-1$ and material is flowing out of cell j into cell $j+1$. The convention for the subscripts is illustrated in figure 2.2. Briefly, n indicates the current timestep, and j the cell number in the x-direction. Δx and Δt are the grid size in the x-direction and the timestep size respectively. The velocities have been calculated at the cell walls, again as illustrated in figure 2.2. The velocities at the cell walls are given by the average $v_{j+\frac{1}{2}}^n = (v_{j+1}^n + v_j^n)/2$.

The result from this numerical calculation of Sod's shock tube problem is illustrated in figure 2.3. Compared to the other scheme illustrated, which has a higher accuracy, it can be seen that there is some numerical diffusion, where the sharpness of the solution is lost.

A more accurate approach to solving this is given by the second order accurate

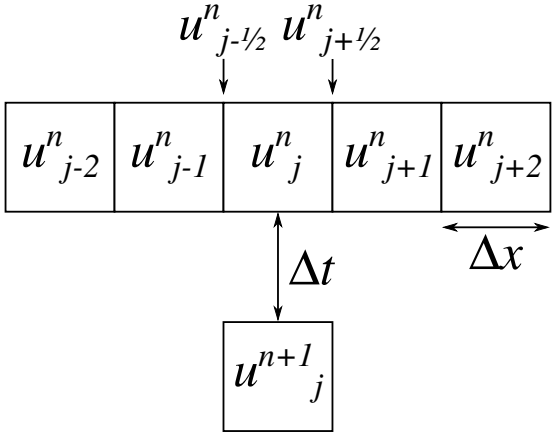

Figure 2.2: An illustration of the labelling convention for the fluid u in the differencing schemes. j refers to the cell number, while n refers to the timestep number. Δx and Δt give the cell and timestep size respectively.

form of the van Leer scheme. A complete description is not given here, but is described by Ridgers [69]. The scheme works by giving a better approximation of the value of the fluid variable across the cell, by estimating it in the form

$$u(x) = u^n_j + \left(\frac{\partial u}{\partial x}\right)^n_{j+\frac{1}{2}} x, \tag{2.87}$$

instead of treating the fluid variables as constant across a cell. It can be seen in figure 2.3 that such a scheme reduces the numerical diffusion when solving Sod's shock tube problem, but another problem has arisen. The spurious oscillations that can be seen are undesirable, and will only grow in time. They are on the order of the cell size, and are unphysical. Dissipative processes like the fluid viscosity can prevent them from building up in the code.

The are a selection of approaches to minimising the effect of these spurious oscillations, the most straightforward is to simply use an artificial viscosity. This mimics the way real viscosity would behave, although it has no physical basis. It takes the form of an extra term in the equation for pressure, giving an effective pressure, q, by

$$q_j = p_j - \epsilon \rho_j c_{sj} \Delta v_j, \tag{2.88}$$

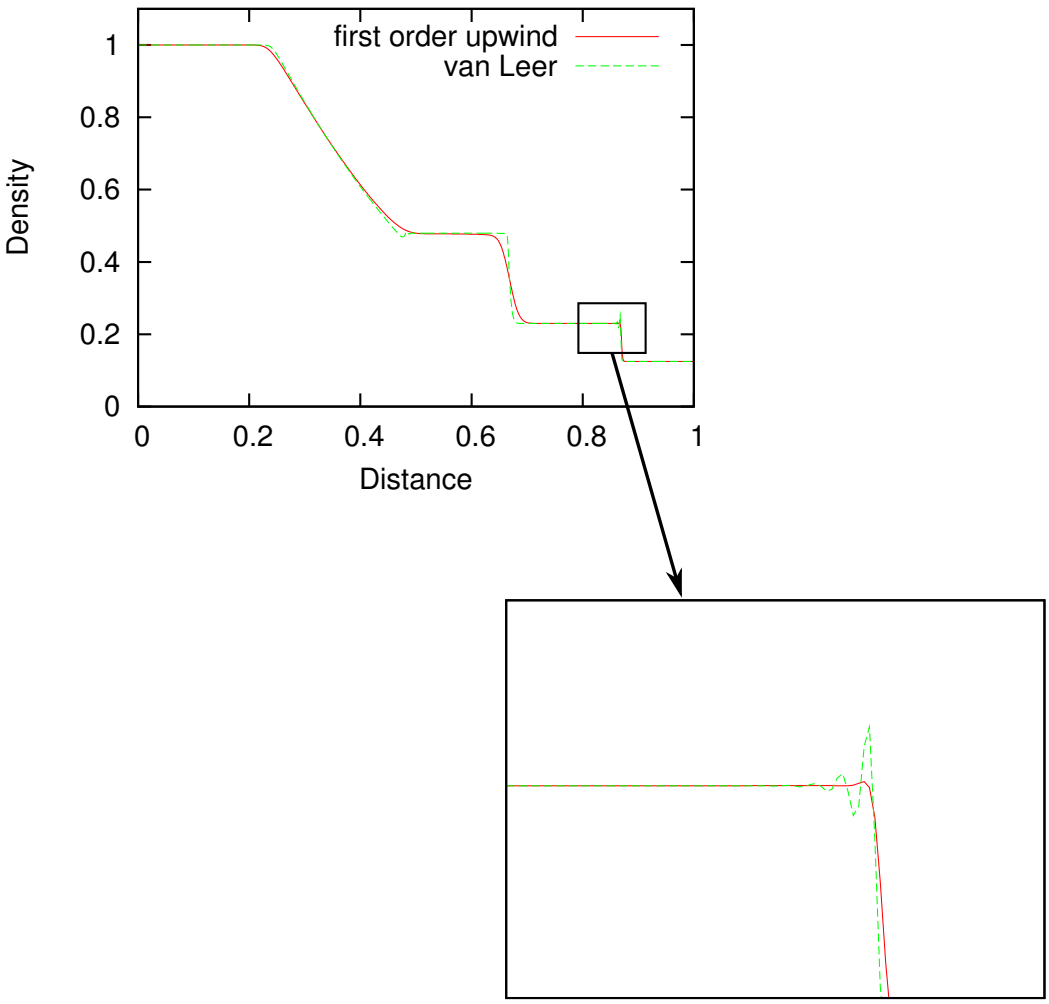

Figure 2.3: The Sod shock tube problem modelled with a first order upwind scheme and a second order van Leer scheme. The exact solution has not been included, but the lower numerical diffusion in the second order van Leer scheme compared with the first order upwind scheme can be seen. The spurious oscillations that can be seen in the van Leer scheme happen cell to cell, i.e. the wavelength is $2\Delta x$. The initial conditions are given by $\rho = 1$, $p = 1$ for $x < 0.5$ and $\rho = 0.125$, $p = 0.1$ for $x > 0.5$. Here $\gamma = 5/3$, which differs from that normally considered in the standard problem. The final time is 0.2 ps and 1000 cells are used.

where $\Delta v_j = (v_{j+1} - v_{j-1})/2$, and c_{sj} is the sound speed given by $c_{sj} = \sqrt{\gamma p_j/\rho_j}$. The effective pressure is then used in the equations for the momentum and energy. A suitable value for ϵ needs to be chosen, typically $\epsilon = 0.4$. Indeed, this reduces the spurious oscillations shown in figure 2.3 as expected. In reference [69] another scheme is used to minimise the spurious oscillations, whereby advection is turned off if any are such oscillations are detected, that is to say if $sign[v_{j+\frac{1}{2}}] \neq sign[v_{j-\frac{1}{2}}]$.

2.5.3 Godunov Schemes

The Riemann problem does have an analytic solution, although iteration is required to obtain some of the values. One more effective approach to solving the MHD equations might be to employ such a Riemann solver. Riemann solvers work by breaking the problem up, by considering a sequence of Riemann problems to solve across each cell. However, this approach can introduce a lot of complexity in the coding, and make it difficult to add extra terms in to the code such as energy transport [70]. An example of a Riemann solver is given by Roe [71].

A useful class of numerical schemes to treat the conserved quantities, as for the equations in section 2.5.1, are the Godunov type schemes [72]. These work by first defining a piecewise-constant solution, and then evolving it to the next timestep [73]. Roughly speaking, a function is defined as piecewise-constant if it is locally constant across some region, with step changes at the boundaries. The Riemann problem is then solved at the boundary, either exactly or approximately.

A particular type of Godunov scheme is described by Kurganov, Noelle and Petrova (the KNP scheme) [73]. The scheme does not involve an explicit Riemann solver, but does treat the Riemann problem properly and requires no artificial viscosity. The key equation in the scheme, in one dimension, is given by

$$\frac{\mathrm{d}}{\mathrm{d}t} u_j(t) = -\frac{H_{j+\frac{1}{2}}(t) - H_{j-\frac{1}{2}}(t)}{\Delta x}, \tag{2.89}$$

where

$$H_{j+\frac{1}{2}}(t) = \frac{a^+_{j+\frac{1}{2}} g(u^-_{j+\frac{1}{2}}) - a^-_{j+\frac{1}{2}} g(u^+_{j+\frac{1}{2}})}{a^+_{j+\frac{1}{2}} - a^-_{j+\frac{1}{2}}} + \frac{a^+_{j+\frac{1}{2}} a^-_{j+\frac{1}{2}}}{a^+_{j+\frac{1}{2}} - a^-_{j+\frac{1}{2}}} \left[u^+_{j+\frac{1}{2}} u^-_{j+\frac{1}{2}} \right]. \tag{2.90}$$

Here $u^+_{j+\frac{1}{2}}$ is the reconstructed value in the cell $j+1$, at $x_{j+\frac{1}{2}}$, and similarly $u^-_{j+\frac{1}{2}}$ is the reconstructed value in cell j at the same position. The values of $a^+_{j+\frac{1}{2}}$ and $a^-_{j+\frac{1}{2}}$ are similarly the local speeds. An implementation of this numerical scheme applied to the conservative form of the MHD equations is described by Ziegler [70].

2.5.4 Constrained Transport

As well as the advection scheme another problem with the MHD equations needs to be considered, which is how to preserve the relation $\nabla \cdot \boldsymbol{B} = 0$ to a high precision. Any deviation from this will quickly lead to unphyiscal effects, which must be avoided. The fundamentals of a scheme to conserve this relation are described by Evans and Hawley [74], while a specific description of such a scheme is given by Balsara and Spicer [75], which is implemented with the KNP scheme by Ziegler [70].

Briefly, this scheme deals with the electric and magnetic fields on the cell wall locations. A special form of Faraday's law is used, such that the discretisation of the electric field will naturally lead to Gauss's law for magnetism being satisfied. In other words, Gauss's law, equation 2.4, satisfies

$$\frac{\mathrm{d}}{\mathrm{d}t}(\nabla \cdot \boldsymbol{B}) = 0. \tag{2.91}$$

Hence, if the magnetic field divergence is initially zero, it will not grow and $\nabla \cdot \boldsymbol{B} = 0$ will be satisfied to machine precision.

2.5.5 Implicit Methods

Explicit methods, which have been discussed so far, calculate the value of a variable at the next time step based on the current information. Conversely,

implicit methods provide an equation linking the current time step and the next one, which must be solved. While implicit methods can be more computationally expensive, and more difficult to implement, they do not rely on a particular choice of time step as explicit methods do (see for example section 3.3.2).

For adding additional features to the code an implicit method can be desirable, so it does not affect the time step required in the fluid code. For the equilibration between ions and electrons, as given in equation 2.77, the implicit equations are given by

$$\frac{T_i^{n+1} - T_i^n}{\Delta t} = -n_e \beta \left(T_i^{n+1} - T_e^{n+1} \right) \tag{2.92}$$

and

$$\frac{T_e^{n+1} - T_e^n}{\Delta t} = -n_i \beta \left(T_e^{n+1} - T_i^{n+1} \right) \tag{2.93}$$

for the ions and electrons respectively, where $\beta(T_i^n, T_e^n) = 1/\tau_{ie} n_e = 1/\tau_{ei} n_i$. This is actually a mix of explicit and implicit methods, through the dependence on β. These are rearranged to yield

$$T_i^{n+1} = \frac{\left(1 + n_i \beta \Delta t\right) T_i^n + n_e \beta \Delta t T_e^n}{1 + \left(n_i + n_e\right) \beta \Delta t} \tag{2.94}$$

for the ions and

$$T_e^{n+1} = \frac{\left(1 + n_e \beta \Delta t\right) T_e^n + n_i \beta \Delta t T_i^n}{1 + \left(n_i + n_e\right) \beta \Delta t} \tag{2.95}$$

for the electrons. This problem is greatly simplified due to the fact that it can be solved for each cell, with no dependence on neighbouring cells.

An implicit method is also useful for the thermal conductivity. From equation 2.56 the thermal conductivity can be written as

$$\frac{\partial e}{\partial t} = \nabla \cdot \left(\kappa \nabla T \right), \tag{2.96}$$

which yields an implicit equation to be solved of the form

$$\frac{T_j^{n+1} - T_j^n}{\Delta t} = \frac{\gamma - 1}{n k_B} \frac{F_{j+\frac{1}{2}}^{n+1} - F_{j-\frac{1}{2}}^{n+1}}{\Delta x}, \tag{2.97}$$

where $F_{j\pm1}^{n+1}$ is the heat flux. Working this through gives the relation

$$T_j^n = T_j^{n+1} - \frac{\Delta t}{2\Delta x^2}\frac{\gamma-1}{n_j k_B}\left[\left(\kappa_{j+1}^n + \kappa_j^n\right)T_{j+1}^{n+1} - \left(\kappa_{j+1}^n + 2\kappa_j^n + \kappa_{j-1}^n\right)T_j^{n+1} + \left(\kappa_j^n + \kappa_{j-1}^n\right)T_{j-1}^{n+1}\right]. \tag{2.98}$$

This can be re-written as a tridiagonal matrix equation. This takes the form

$$\begin{pmatrix} \dots \\ T_{j-1}^n \\ T_j^n \\ T_{j+1}^n \\ \dots \end{pmatrix} = \begin{pmatrix} & & \dots & & \\ & b_{j-1}^n & c_{j-1}^n & 0 & \\ \dots & a_j^n & b_j^n & c_j^n & \dots \\ & 0 & a_{j+1}^n & b_{j+1}^n & \\ & & \dots & & \end{pmatrix} \begin{pmatrix} \dots \\ T_{j-1}^{n+1} \\ T_j^{n+1} \\ T_{j+1}^{n+1} \\ \dots \end{pmatrix}, \tag{2.99}$$

where the coefficients are given by

$$b_j^n = 1 + \alpha_j\left(\kappa_{j+1}^n + 2\kappa_j^n + \kappa_{j-1}^n\right) \tag{2.100}$$

$$a_j^n = -\alpha_j\left(\kappa_j^n + \kappa_{j-1}^n\right) \tag{2.101}$$

$$c_j^n = -\alpha_j\left(\kappa_{j+1}^n + \kappa_j^n\right) \tag{2.102}$$

and

$$\alpha_j = -\frac{\Delta t}{2\Delta x^2}\frac{\gamma-1}{n_j k_B}. \tag{2.103}$$

To solve for the values $\boldsymbol{T}^{n+1}$ the matrix needs to be inverted. Due to the fact that the matrix is tridiagonal it can be solved by the Thomas algorithm [76], which is much less computationally expensive than a full matrix inversion.

Implementation of these implicit schemes in a code will be discussed in section 3.5, with the code included in section A.2 of appendix A.

2.6 Summary

In this chapter the magnetohydrodynamic equations have been shown to follow from the Vlasov equation, which itself followed from the collisionless Boltzmann equation and the Lorentz force. The MHD equations provide a description of how an ideal plasma will behave. When collisions are taken in to account the resistivity was found to be important, which leads to magnetic diffusion in the plasma, and magnetic field generation and Ohmic heating in the presence of an electric current. Also following from the consideration of the collisions was the expression for thermal conductivity in the plasma. A change to the equation set to allow the ions and electrons to have different temperatures was shown.

The approach to solving the MHD equations numerically was also discussed, with a consideration to the advantages and drawbacks of various methods that can be used to solve them. Using implicit methods to add terms that arise from non-ideal MHD was also explored.

This provides the background to the methods, results and findings of the next chapter. The MHD equations will be used to obtain a better understanding of the physics that occurs when a fast electron current is present in a plasma, and an MHD code that was developed to explore this effect will be presented.

Chapter 3

Cavitation and Shockwave Generation in Fast Ignition Relevant Plasmas

Fast ignition (FI) [12], introduced in section 1.5, is an inertial confinement fusion scheme where a separate igniter laser pulse is fired into a compressed capsule of deuterium-tritium fuel. This creates a beam of hot electrons which heat the compressed fuel close to the centre. Once a high enough temperature is reached a self-sustaining burn-wave can propagate through the rest of the cold fuel and heat it up to fusion temperatures. The original fast ignition scheme envisaged achieving this by using the igniter laser to bore up to the critical density in a plasma, where a beam of hot electrons would be produced that heat a region of the dense fuel [36]. Recently there has been more interest in cone-guided fast ignition, where a hollow gold cone is embedded in the initial capsule, creating a clear path for the laser energy to reach the centre of the fuel [38, 39].

In either variant, and in many petawatt-scale laboratory experiments [77], the propagation of a relativistic electron beam is a critical element. The fast electron beam will rapidly heat the background plasma, creating a massively over-pressured region. This will explode, depressing the density in the heated region, a process which is often referred to as cavitation. In this chapter a simple analytic model is used which predicts the density, pressure, magnetic field and

velocity in the plasma to study the basics of cavitation in these circumstances. The plasma considered will initially be at rest, with a uniform temperature and density, and with no initial magnetic field. This model will be used to explore the strength of the cavitation over a wide range of parameter space that is of interest to fast ignition fusion. Using an MHD code created specifically to look at this problem will allow the validity of the analytic model in predicting the amount of cavitation that will occur in a plasma to be verified. The region of hot electron current density and mass density can also be found where the pressure gradient from the Ohmic heating is so extreme that a shock wave is launched into the surrounding plasma.

3.1 The Return Current

A relativistic electron beam propagating through a sufficiently dense background plasma will set-up a charge balancing resistive return current, such that

$$\boldsymbol{J}_f + \boldsymbol{J}_p \simeq 0, \tag{3.1}$$

where $\boldsymbol{J}_f$ and $\boldsymbol{J}_p$ are the forward going fast electron current and the return current respectively [78]. Here the return current is denoted with the p subscript, as it is carried by the background plasma electrons, which will be distinguished from the fast electrons. For the background plasma to be sufficiently dense, it must have an electron number density that is much larger than that in the fast electron current, that is to say $n_p \gg n_f$. A resistive electric field is formed such that $\boldsymbol{E} = \eta \boldsymbol{J}_p \simeq -\eta \boldsymbol{J}_f$, where η is the resistivity of the plasma [51, 79]. The electrons would be expected to slow down over some distance in the plasma, by collisional stopping, as discussed in section 2.4.3. However, they can be slowed down sooner, due to the inability of the background plasma to provide a sufficient return current. This scale length over which this would happen was considered in equation 1.32.

This resistive return current will create a $\boldsymbol{J}_p \times \boldsymbol{B}$ force on the plasma and a pressure gradient via Ohmic heating, both of which would be expected to push the plasma away from the centre of the electron beam. 2D-3V Vlasov-Fokker-

Planck simulations of this effect have previously been performed by Kingham *et al.* [80], which showed collimation of such an electron beam. A similar problem applied to cosmic rays passing through low density plasma has been considered by Bell [81].

3.1.1 The Effect of a Resistive Return Current on a Background Plasma

To understand what happens to the background plasma the effects of a collisionless fast electron current and resistive return current need to be added to the MHD equations. To do this the derivation of the momentum equation needs to be reconsidered, including the extra terms that will be required. The momentum equation was given in equation 2.35, and was obtained from the first order moment of the Vlasov equation, equation 2.24.

An extra species now needs to be considered, that of the fast electrons, denoted by the subscript f, in addition to the ions and background electrons that were originally considered when deriving the MHD equations. The species will be treated as distinguishable, so there can be no transfer between the background plasma electrons and the fast electrons. For the fast electrons the following momentum equation is then obtained

$$m_e n_f \left(\frac{\partial \boldsymbol{u}_f}{\partial t} + (\boldsymbol{u}_f \cdot \nabla) \boldsymbol{u}_f \right) = -e n_f (\boldsymbol{E} + \boldsymbol{u}_f \times \boldsymbol{B}) - \nabla p_f + \frac{\partial \boldsymbol{p}_f}{\partial t}. \tag{3.2}$$

Taking the MHD equation for the momentum, equation 2.35, reads

$$\rho \frac{d\boldsymbol{v}}{dt} = \boldsymbol{J_p} \times \boldsymbol{B} - \nabla p \tag{3.3}$$

using the approximations that $\rho \approx n_i m_i$ and $\boldsymbol{v} \approx \boldsymbol{u}_i$ as established in section 2.5.

Now the contribution due to the fast electron current is considered. The limit is taken where $n_f \ll n_e$, but $n_f \boldsymbol{u}_f$ remains finite, due to the fact the fast electrons will have a velocity such that $\boldsymbol{u}_f \gg \boldsymbol{u}_e$. The fast population does not affect the electric field in the limit $n_f \ll n_e$. It does make a contribution to the

total current density however, $\boldsymbol{J}_{total}$, which is now given by

$$\boldsymbol{J}_{total} = Zen_i\boldsymbol{u}_i - en_e\boldsymbol{u}_e - en_f\boldsymbol{u}_f = \boldsymbol{J}_p + \boldsymbol{J}_f. \tag{3.4}$$

The quasi-neutrality assumption here still holds, such that $Zen_i - en_e = en_f \simeq 0$, from equation 3.1. Ampère's Law, equation 2.5, now takes a hybrid approximation of the form

$$\nabla \times \boldsymbol{B} = \mu_0 \boldsymbol{J}_{total} = \mu_0 \left(\boldsymbol{J}_p + \boldsymbol{J}_f\right) \tag{3.5}$$

and combining this with equation 3.3 gives

$$\rho\left(\frac{\partial \boldsymbol{v}}{\partial t} + \left(\boldsymbol{v}\cdot\nabla\right)\boldsymbol{v}\right) = \frac{1}{\mu_0}\left(\nabla\times\boldsymbol{B}\right)\times\boldsymbol{B} - \boldsymbol{J}_f\times\boldsymbol{B} - \nabla\cdot\boldsymbol{p}. \tag{3.6}$$

Note that there have been no assumptions about the return current exactly cancelling the fast electron current here, however if it does, that is to say if $\boldsymbol{J}_p + \boldsymbol{J}_f = 0$, then $\boldsymbol{J}_{total} = (\nabla\times\boldsymbol{B})/\mu_0 = 0$

A similar equation is used by Bell [81], but applied to cosmic rays (protons) passing through a supernova remnant. The basic physical principles remain the same, though the limits of applicability of this equation in the context of fast ignition require consideration.

This limit is generally valid for the parameters considered in this chapter, although in the most extreme cases it begins to break down. The lowest ion density considered here is $n_i = 6.0\times10^{27}$ m^{-3}, if we assume a hydrogen plasma. The highest current density considered in is 10^{17} A m^{-2}. Taking $n_f = J_f/q_e c$ gives $n_f = 2.1\times10^{27}$ m^{-3} (assuming $v_e \approx c$, 1 MeV electrons for example have $v_e = 0.81c$). In this extreme case the fast electron density is significant, but in the less extreme regimes generally considered throughout this chapter it will be true that n_f will be orders of magnitude less than n_i. It is a difficult problem to show exactly how small n_f must be for this model to remain accurate, but over the vast majority of parameters considered the condition $n_f \ll n_i$ will easily be satisfied. This means that the assumption that there is negligible contribution from the fast electrons to the electric field is valid, while current density, $\boldsymbol{J}_f$, does still need to be considered.

3.2 Derivation of Approximate Analytic Model

In this section the application of a return current to a background plasma is considered. As stated in the introduction to this chapter, the initial density and temperature are taken to be constant, and the plasma initially at rest.

3.2.1 Resistive Return Current

The resistive form of Ohm's law, as found in equation 2.46, that needs to be considered here for the background plasma is

$$\boldsymbol{E} + \boldsymbol{v} \times \boldsymbol{B} = \eta \boldsymbol{J}_p. \tag{3.7}$$

Here there is a contribution to the electric field due to the resistive return current, but none due to the collisonless fast electron current.

In addition the return current will cause Ohmic heating in the plasma, as established in equation 2.71, which, for a temperature T_p in the background plasma is given by

$$\frac{\partial T_p}{\partial t} = \frac{(\gamma - 1)}{n_i k_B} \eta(T_p) J_p^2. \tag{3.8}$$

Here the contribution of thermal conduction to the energy has been neglected.

The Spitzer-Härm resistivity is used [62], which was discussed in section 2.4.4 and is given by

$$\eta(T_p) = 10^{-4} \frac{Z \ln \Lambda}{T_p^{3/2}} \left(\frac{e}{k_B} \right)^{3/2} \ \Omega\text{m}. \tag{3.9}$$

This is equation 2.55, for the resistivity perpendicular to the magnetic field, which will be the type that is relevant for the work presented in this chapter. The validity of Spitzer-Härm resistivity was also discussed in section 2.4.4, where it was found to be valid for temperatures in the plasma above 100 eV at solid density, and is valid at lower temperatures for lower mass densities. The plasma is assumed to be fully ionised. In reality other effects, for example ion acoustic turbulence [82], could also make a contribution to the form of the resistivity, but this is not considered here.

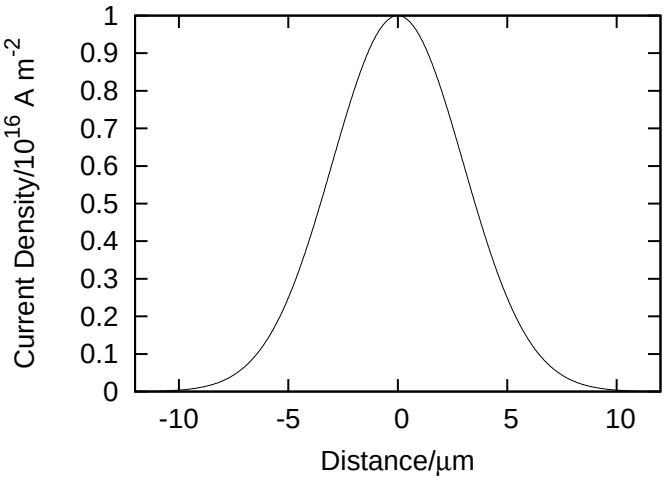

Figure 3.1: The current density, as shown in equation 3.10, for $J_0 = 10^{16}$ A m^{-2} and $R_f = 3$ µm.

The return current is modelled as a one dimensional rigid beam, with a Gaussian profile such that

$$\boldsymbol{J}_p = J_p(x)\hat{\boldsymbol{y}} = -J_f(x)\hat{\boldsymbol{y}} = J_0 e^{\frac{-x^2}{2R_f^2}}\hat{\boldsymbol{y}}, \tag{3.10}$$

where R_f determines the width of the fast electron beam. The unit vector notation is dropped in the rest of this chapter, but the current density is only ever considered in the y-direction. An example of this current density profile is illustrated in figure 3.1.

By taking the return current to be in the y-direction, and combining Faraday's law given in equation 2.4 with the form of Ohm's law given in equation 3.7, it is found that only the z-component of the magnetic field contains a source term,

$$\frac{\partial B_z}{\partial t} + \frac{\partial\left(B_z v_x\right)}{\partial x} = -\frac{\partial\left(\eta J_p\right)}{\partial x}, \tag{3.11}$$

which is a one dimensional form of equation 2.47. This means that, provided they are zero initially, B_x and B_y will always be zero.

3.2.2 The Temperature and Pressure

The functions $J_p(x)$ and $\eta(T_p)$, for current density and resistivity respectively, were given in equations 3.10 and 3.9. An analytic estimate of the temperature can be made by neglecting advection in the plasma. This results in the separable, partial differential equation

$$\left.\frac{\partial T_p}{\partial t}\right|_x = 10^{-4}\frac{Z\ln\Lambda}{T_p^{3/2}}\left(\frac{e}{k_B}\right)^{3/2} J_p^2\frac{(\gamma-1)}{n_0 k_B}, \tag{3.12}$$

where the approximation that the density is constant, $n_i(x,t) = n_0$, has been made, which is equivalent to no advection. The notation on the right hand side states that the function is being solved for a fixed value of x. The function to be solved can be equivalently written as

$$\int_{T_0}^{T_p} T_p'^{3/2}(x,t')dT_p' = \int_0^t 10^{-4}Z\ln\Lambda\left(\frac{e}{k_B}\right)^{3/2} J_p^2(x)\frac{(\gamma-1)}{n_0 k_B}dt', \tag{3.13}$$

where the integration is performed from $t' = 0$ to t and from $T_p' = T_0$, the initial temperature, to T_p, the temperature at time t. This results in a function for temperature given by

$$T_p(x,t) = \left(T_0^{5/2} + \frac{5}{2}10^{-4}Z\ln\Lambda\left(\frac{e}{k_B}\right)^{3/5} J_p^2\frac{(\gamma-1)}{n_0 k_B}t\right)^{2/5}. \tag{3.14}$$

From this an expression for the pressure can also be found, by re-using the approximation that the density is constant and taking the ideal gas equation of state. This gives

$$p(x,t) = n_0 k_B T_p(x,t). \tag{3.15}$$

This approximation is reasonable because, as illustrated in equation 3.14, the heating is proportional to $t^{2/5}$, so the initial temperature and pressure increase is most significant very early on, before the plasma begins to move.

3.2.3 The Magnetic Field

A similar treatment is applied to the magnetic field. Taking equation 3.11, and once again neglecting advection, an expression for the magnetic field can be found by solving

$$\left.\frac{\partial B_z}{\partial t}\right|_x = -\frac{\partial(\eta J_p)}{\partial x} = -J_p\frac{\partial \eta}{\partial x} - \eta\frac{\partial J_p}{\partial x}, \tag{3.16}$$

where the function $J_p(x)$ was given by equation 3.10, $\eta(T_p(x,t))$ by equation 3.9 and $T_p(x,t)$ by equation 3.14. The expression for B_z is then found to be given by

$$B_z(x,t) = \frac{x}{J_p R_f^2}\left(2\eta J_p^2 t - \frac{n_0 k_B}{(\gamma-1)}\left(T_p - T_0\right)\right). \tag{3.17}$$

The growth of the magnetic field is restricted by the balancing of the two gradient terms in equation 3.16. From the form of the imposed current, J_p, there is a positive growth term for positive x, and a negative growth term due to the gradient of the resistivity arising from the Ohmic heating. For the values considered in this paper these two terms generally act to cancel each other out in the central region of the beam. Further towards the edges, as $J_p^2 \to 0$, the equation for temperature can be expanded using the binomial approximation, giving

$$B_z(x,t) = x\frac{\eta J_p t}{R^2}. \tag{3.18}$$

An example of the form of the magnetic field will be shown in section 3.4.

3.2.4 The Momentum

A similar treatment is given to the momentum equation,

$$\rho\left.\frac{\partial v_x}{\partial t}\right|_x = J_p B_z - \frac{\partial p}{\partial x}, \tag{3.19}$$

using the pressure given by equation 3.15. Once again the advection term from the full momentum equation has been neglected. This leads to an acceleration of

the plasma due to the pressure gradient and the $J_p \times B$ force.

The acceleration from the $J_p \times B$ force is actually relatively weak, it was found from equation 3.17 that the two terms in equation 3.16 act to oppose each other, so the most significant magnetic field growth in the plasma occurs towards the edge of the current beam, where the current is small. It can be shown that the pressure gradient is always larger by taking the ratio between the $J_p \times B$ force, using the approximate expression for B_z in equation 3.17, and the expression for the pressure gradient, from equation 3.15. This eventually yields the expression

$$\frac{J_p B_z}{-\nabla p} = \frac{1}{4}\left(2\frac{n_0 k_B (T_p^{3/2} - T_0^{3/2})}{T_0^{1/2}(\gamma-1)^2 \eta_0 J_p^2 t} - \frac{1}{\gamma - 1}\right), \tag{3.20}$$

where η_0 is the initial value of the resistivity, that is $\eta_0 = \eta(T_0)$.

This equation can be understood by most straightforwardly by taking the extreme cases, where $J_p^2 t/n_0 \to 0$ and $J_p^2 t/n_0 \to \infty$. In the former case, weak cavitation, the ratio of the $J \times B$ force to the pressure gradient becomes $(2(\gamma-1))^{-1}$ and in the latter case, strong cavitation, the ratio becomes $(-4(\gamma-1))^{-1}$. For a monatomic gas with $\gamma = 5/3$ the ratio will go from $3/4$ in the weak case to $-3/8$ in the strong case. This function is plotted in figure 3.2, which illustrates that the function varies smoothly between the two extremes. The variable ξ is given by $\xi = J_p^2 t/n_0$, which can be singled out as the variable equations 3.14 and 3.17 are dependent upon. It can be seen that the pressure gradient is always larger. The low values of ξ correspond to weak cavitation, meaning early time, low current density or high density. The higher values correspond to strong cavitation of the plasma.

Although the values for the $J_p \times B$ force compared to the pressure gradient are not insignificant, ∇p is always larger, and therefore the ansatz will be made that the $J_p \times B$ force can be neglected. The validity of this will be tested in section 3.4, where the expression for the momentum can be compared against that obtained from the MHD code.

Hence, by neglecting the $J_p \times B$ force, the momentum equation due to the

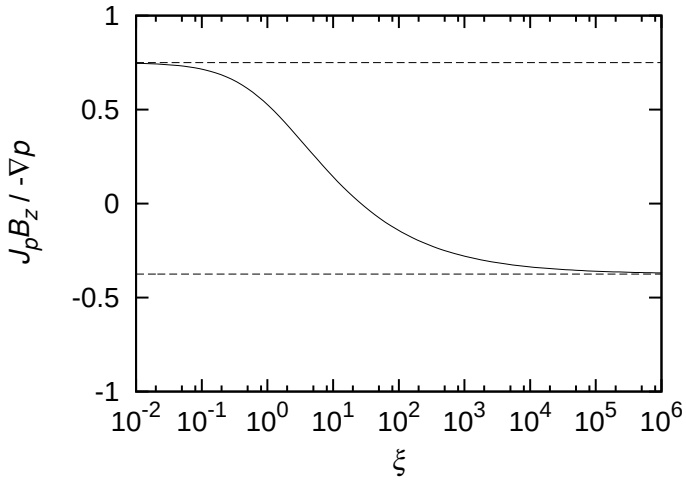

Figure 3.2: A plot of equation 3.20, the ratio of the $J_p \times B$ force to the ratio of the pressure gradient force for a plasma heated by a return current. The plot uses dimensionless units, the variable ξ is given by $\xi = J_p^2 t/n_0$. The dashed lines are at $3/4$ and $-3/8$. The initial temperature is $T_0 = 1$ and $\gamma = 5/3$.

pressure gradient is given by

$$\rho_0 v_x(x,t) = \frac{4}{7}\frac{x}{R_f^2}\left(n_0 k_B T_p t - \frac{1}{\eta_0 J_p^2}\frac{(n_0 k_B)^2}{\gamma - 1} T_0 \left(T_p - T_0\right)\right). \tag{3.21}$$

3.2.5 The Density

Finally, from the previous equations an approximate function can be obtained for the density. This is done by solving the mass continuity equation, and using the estimate that was obtained for the velocity in the plasma in equation 3.21. The equation to be solved then is

$$\left.\frac{\partial \rho}{\partial t}\right|_x = -\frac{\partial(\rho_0 v_x)}{\partial x}, \tag{3.22}$$

where once again the approximation has been made that the density term in the mass continuity equation can be taken as the initial density. This means the resulting function for $\rho(x,t)$ is only valid for weak cavitation in the plasma. The

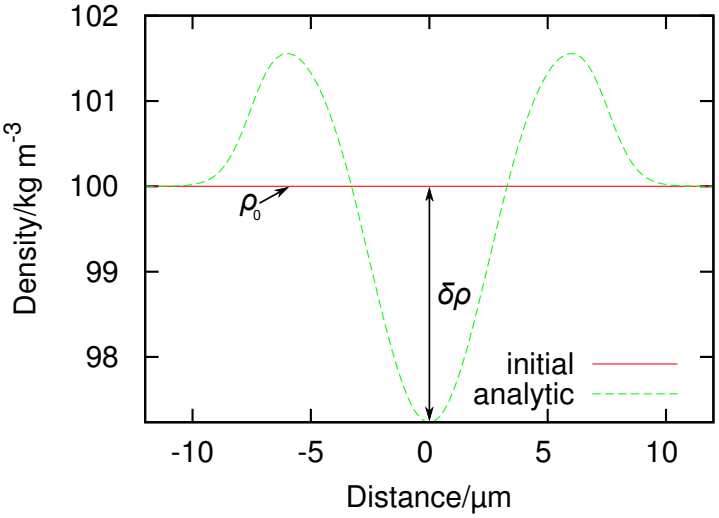

Figure 3.3: An illustration of the parameters $\delta\rho$ and ρ_0. This parameters in this density profile are $J_0 = 10^{16}$ A m^{-2}, $T_0 = 100$ eV, $R_f = 3$ µm, $Z = 1$ and $\ln\Lambda = 10$. The profile is shown after $t = 3$ ps.

density change, $\delta\rho(x,t) = \rho_0 - \rho(x,t)$, is found to be given by

$$\begin{aligned}\delta\rho(x,t) = \frac{4}{21}\frac{1}{R_f^4}\Bigg[&\frac{1}{(\eta_0 J_p^2)^2}(R_f^2+4x^2)\frac{(n_0k_B)^3}{(\gamma-1)^2}T_0^2(T_p-T_0)\\ &+\frac{t}{\eta_0 J_p^2}\frac{(n_0k_B)^2}{\gamma-1}T_0\left(2(R_f^2+x^2)T_p-3(R_f^2+2x^2)T_0\right)\\ &-\frac{t^2}{4}(5R_f^2-4x^2)n_0k_BT_p\Bigg].\end{aligned} \tag{3.23}$$

This expression for the change in density will be used in the next section to show the significance of cavitation over a wide parameter space. In section 3.4 specific plots of $\rho(x)$ will be shown. A plot of $\delta\rho/\rho_0$ is shown in figure 3.3, along with an illustration of the parameter $\delta\rho$.

3.2.6 Parameter Scans

Figure 3.4 shows a plot of $\delta\rho/\rho_0$, at $x = 0$, across a range of values for the initial mass density, ρ_0, and peak current density, J_0 (which occurs at $x = 0$,

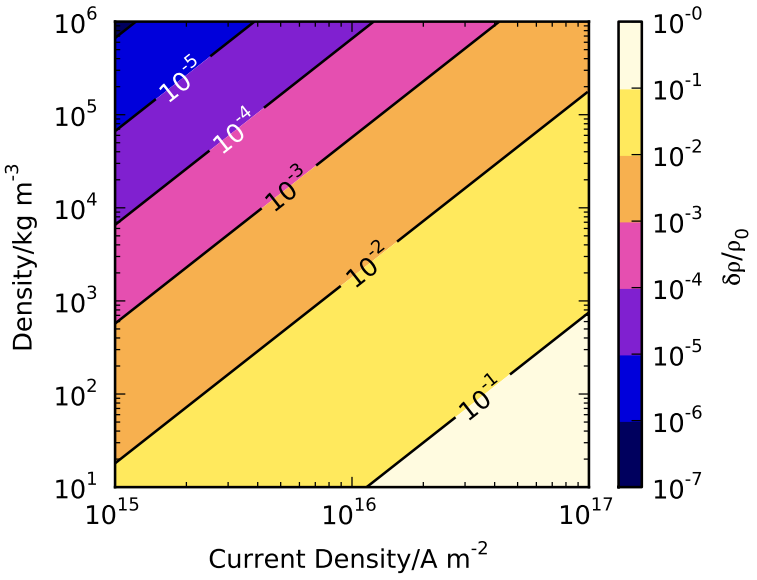

Figure 3.4: A parameter scan across density and current from the model. The initial parameters are $T_0 = 100$ eV, $R_f = 3$ µm, $Z = 1$ and $\ln\Lambda = 10$, at a time $t = 3$ ps. The contour lines show increases of a factor of 10.

from equation 3.10). The amount of cavitation in the plot is dependent on the ratio J_0^2/ρ_0. The dependence on J_0^2 comes about due to the power going into the plasma, ηJ_p^2, from the Ohmic heating given in equation 2.71. The ρ_0 dependence is related to the heat capacity of the plasma, more precisely this dependence is on the parameter $(\gamma-1)/(n_0 k_B)$. This can be seen from equation 3.23, for $\delta\rho$, by dividing throughout by n_0. In this equation the function T_p, equation 3.14, itself has the same dependence on J_0^2/ρ_0. At the highest values of hot electron current, and the lowest values of mass density, the cavitation becomes quite significant. At values of the cavitation approaching unity on the parameter scan it should be noted that the analytic model developed will have limited applicability, as the cavitation is strong enough that the approximation of a constant ρ_0 is no longer valid. Nevertheless, the parameter scan still shows where the cavitation is expected to be particularly strong.

The critical surface in a hole boring fast ignition scheme starts off around 1 mm from the central region of the target. After the hole boring prepulse,

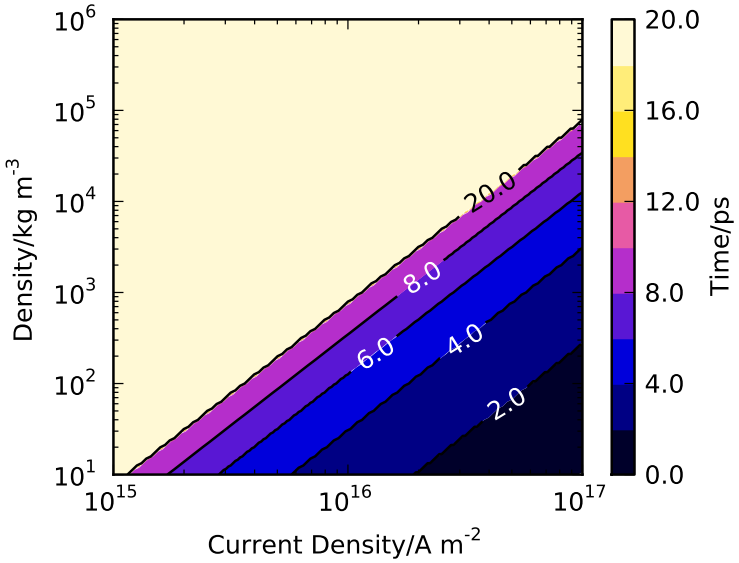

Figure 3.5: The time taken for shocks to form for different values of current density and mass density. The initial parameters are the same as in figure 3.4. Above the 20 ps contour the plot is saturated, so a shock would take more than 20 ps to form, if it would ever form at all.

which lasts for hundreds of picoseconds, this is reduced to ∼35 µm [36]. The hot electrons have to cross this region, which has a range of densities from 10 kg m^{-3} up to 10^6 kg m^{-3} [83]. When comparing this range to figure 3.4, it can be seen that the cavitation effect will be significant over much of this density range. In typical experiments done today at around solid density, the duration of the electron beam is short; typically less than 1 ps. In this regime the cavitation effect will not be significant compared to, for example, the expansion of the plasma.

In this work a rigid beam has been used to represent the electrons. In a real fast ignition target, magnetic collimation of the electron beam may occur, as discussed in references [84] and [85]. However, so long as the width of the collimated beam is similar to the width of the rigid beam considered here, the results will remain valid.

A similar treatment can be applied to find the parameters for which shocks are expected to form in the plasma. Equation 3.21 gives the velocity expected

in the plasma, so it can be determined when $v_{max} > c_{s0}$, where c_{s0} is the initial sound speed, given by $c_{s0} = \sqrt{\gamma k_B T_0}$. Whether or not a shock is formed, and how quickly if it is, is once again determined by the ratio J_0^2/ρ_0; for larger values shocks will form much more rapidly.

Figure 3.5 shows a parameter scan across the same range of values as in figure 3.4. The colour scale shows the time at which a shock would form in the plasma, which is at an initial temperature of 100 eV. At the top end of the colour scale times are >20 ps, meaning that no shock would be formed within 20 ps, if it would ever form at all. It can be seen that the region of shock formation for times longer than 8 ps become very narrow. This a transition is being made into the region in parameter space where a shock would never form.

In the section 3.4 these analytic results will be compared against a fully numerical solution of the model.

3.3 Code Description

The 1D MHD code that was developed is based on the method by Ziegler [70], this method was described in detail in sections 2.5.3 and 2.5.4. Including the $J_p \times B$ term, from the resistive growth of the field, and the pressure gradient, from the Ohmic heating, the set of equations to solve are

$$\frac{\partial \rho}{\partial t} + \frac{\partial(\rho v_x)}{\partial x} = 0 \tag{3.24}$$

$$\frac{\partial(\rho v_x)}{\partial t} + \frac{\partial(\rho v_x^2)}{\partial x} = J_y B_z - \frac{\partial p_{tot}}{\partial x} \tag{3.25}$$

$$\frac{\partial e}{\partial t} + \frac{\partial(e v_x)}{\partial x} = \eta J_y^2 + \frac{B_z}{\mu_0}\frac{\partial(\eta J_y)}{\partial x} + J_y B_z v_x - \frac{\partial(p_{tot} v_x)}{\partial x} \tag{3.26}$$

$$\frac{\partial B_z}{\partial t} + \frac{\partial(B_z v_x)}{\partial x} = -\frac{\partial(\eta J_y)}{\partial x} \tag{3.27}$$

$$e = \frac{p}{\gamma - 1} + \frac{1}{2}\rho v_x^2 + \frac{B_z^2}{2\mu_0}, \tag{3.28}$$

where e is the total energy density, $J_y = J_p(x)$ and p_{tot} is the total pressure, given by $p_{tot} = p + B_z^2/2\mu_0$. In equation 3.26, for the energy density, the first three terms on the right-hand side come from the imposed electron current, they are for the Ohmic heating, magnetic field growth and the $J_p \times B$ force respectively.

As the problem here is only one dimensional, the enforcement of $\nabla \cdot \boldsymbol{B} = 0$ is straightforward to implement. It would be permissible to have x and y-direction magnetic fields in the one dimensional code, and in such cases serious consideration does again have to be given to preserve $\nabla \cdot \boldsymbol{B} = 0$. However, here only z-direction magnetic fields are considered. Otherwise the implementation used here is as described by Ziegler, with Runge-Kutta 2 [86] integration of the MHD equations. Numerical diffusion is low due to the method of interpolation onto the cell walls, and open boundary conditions were used.

This section contains a description of the additional considerations to the Ziegler scheme, and the full code listing is provided in section A.1 of Appendix A.

3.3.1 Test of Code Fundamentals

A useful set of tests for one dimensional MHD problems are provided by Ryu and Jones [87]. Here they considered a range of problems, mostly similar to Sod's shock tube described in section 2.5.2, but with magnetic fields both in the x-direction and perpendicular to it. A useful test case to consider has the initial conditions

$$\begin{bmatrix} \rho \\ v_x \\ p_{tot} \\ B_z \end{bmatrix}_L = \begin{bmatrix} 1 \\ -1 \\ 1 \\ 1 \end{bmatrix} \qquad \begin{bmatrix} \rho \\ v_x \\ p_{tot} \\ B_z \end{bmatrix}_R = \begin{bmatrix} 1 \\ +1 \\ 1 \\ 1 \end{bmatrix} \tag{3.29}$$

such that the initial momentum is given by $\rho v_x = 1$ and the initial internal energy $e = 2.5$. As previously, the subscript L denotes the left-hand side, $x < 0.5$, and the subscript R denotes $x > 0.5$. For this example only dimensionless units are used, where $\mu_0 = 1$, for consistency with the examples given by Ryu and Jones.

The results, along with the initial conditions are shown in figure 3.6. These

closely match the results given by Ryu and Jones [87], which are also shown, where the simulations were performed both by an explicit finite difference scheme and a Riemann solver. The regions where the fluid quantities are constant have an analytic solution, which also matches the results from the MHD code. Small errors at $x = 0.5$ are visible in the density, pressure and magnetic field, which were also seen by Ryu and Jones, and are common to shock tube simulations where there is a strong rarefaction wave.

3.3.2 Choice of Time Step in the Code

The usual use of time step in explicit finite difference schemes is given by the Courant-Friedrichs-Lewy (CFL) condition [88]. In one dimension this is given by

$$\Delta t_{CFL} = C\frac{\Delta x}{v_{max}}, \tag{3.30}$$

where C is the Courant number, usually chosen to be just less than unity. The velocity, v_{max}, is the maximum velocity in the entire grid. In the work presented in this chapter a Courant number of $C = 0.7$ is used, except where otherwise stated. This corresponds physically to restricting the time step to 0.7 of the time it takes for information to propagate across a single cell on the grid.

The fast electron current is added into the code via the return current given in equation 3.10. Spitzer-Härm resistivity, equation 3.9, is used, along with the resistive magnetic field growth and Ohmic heating terms. One additional problem this creates is the necessity to resolve the initial rapid heating of the plasma due to the temperature growing as $T_p \propto t^{2/5}$. To ensure this growth is well resolved a characteristic temperature doubling time is determined from equation 3.14

$$\Delta t_{Ohm} = \frac{\left(2^{5/2} - 1\right) T_{max}^{5/2}}{\alpha}, \tag{3.31}$$

where T_{max} is the maximum temperature in the plasma at a particular time step and α is given by

$$\alpha = \frac{5}{2}\frac{10^{-4} Z \ln\Lambda \left(\gamma - 1\right) J_0^2 m_i}{k_B \rho_{max}} \left(\frac{e}{k_B}\right)^{3/2}. \tag{3.32}$$

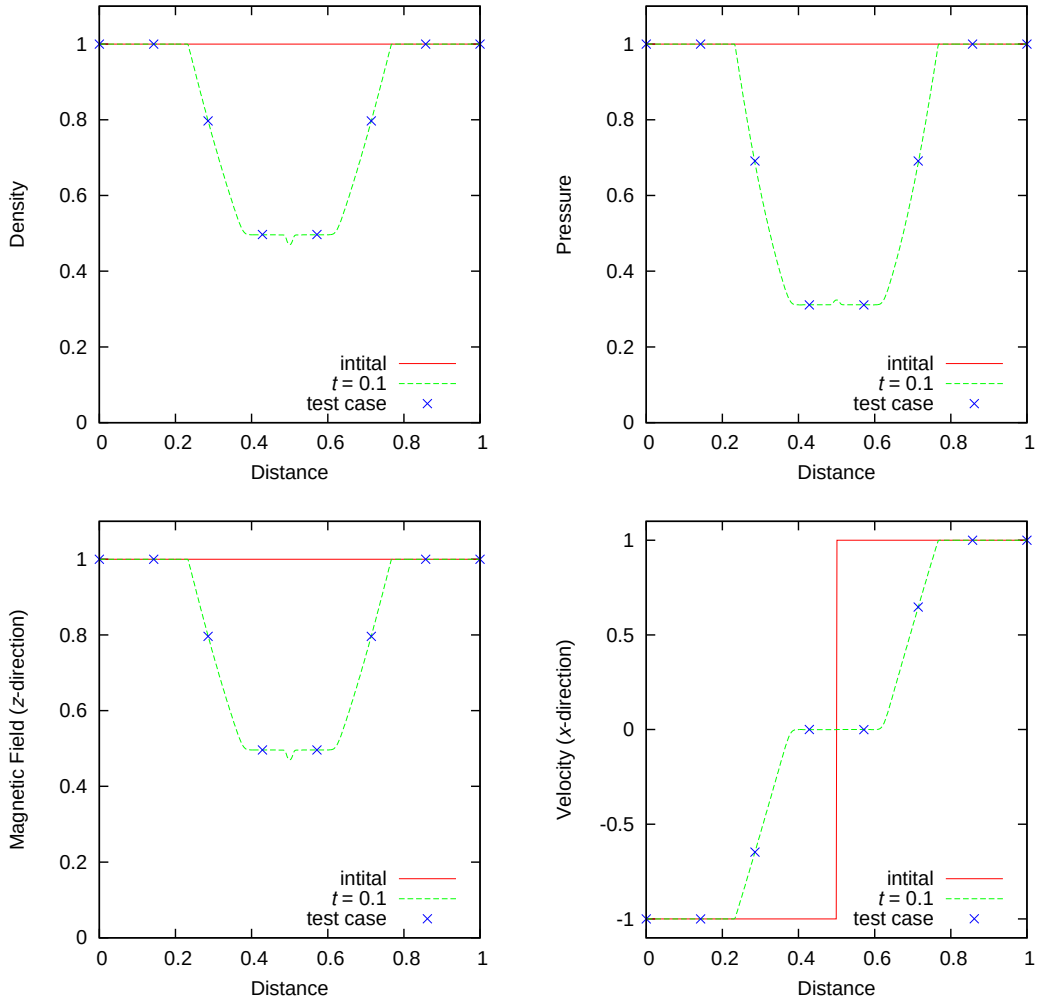

Figure 3.6: Plots of the density, pressure, magnetic field and velocity at $t = 0.1$, for a test case given by Ryu and Jones [87], with the initial values also shown. A comparison with the results from Ryu and Jones is shown, which gives the same result as the analytic solution (except for the points at $x = 0.3$ and 0.7, where no analytic solution is available). For direct comparison to the work they presented 512 grid cells and a Courant number of 0.8 were used (see section 3.3.2). Here $\gamma = 5/3$, and the results presented are for a system of units were $\mu_0 = 1$.

The lowest value between Δt_{Ohm} and the usual CFL condition is then chosen. This means that for the first few time steps in the simulation Δt_{Ohm} restricts the time step, and later the usual CFL criterion is responsible for the restriction. Using a smaller fraction of Δt_{Ohm} as the minimum time-step was found to make no difference to the results from the code.

3.4 Tests and Examples of Analytic Model against the 1D MHD Code

To begin with a typical case of interest to fast ignition is used to compare the results from the code with the results predicted by the analytic model. In figure 3.7 the results are compared for the case where $J_0 = 10^{16}$ A m^{-2} and $\rho_0 = 100$ kg m^{-3}, up to a time of 3 ps.

From figure 3.7 it can be seen that the analytic model and the MHD code give very good agreement. The plot for pressure shows a small increase in the analytic case compared with the code result, as would be expected from advection of the plasma and $p\,dV$ cooling. The analytic prediction for the magnetic field from equation 3.17 is extremely close to the full numerical solution.

The plot for the velocity shows that the pressure gradient term alone gives a reasonable estimate of the velocity in the plasma. It can be seen that the $J_p \times B$ force is inclined to pinch the plasma in the centre, while causing cavitation towards the edge of the imposed current beam. The contribution to the velocity from the magnetic field remains small, which means that the ansatz made in section 3.2.4 that the $J_p \times B$ force can be neglected in the analytic model is reasonable.

Overall the estimate of the cavitation in the plasma is quite good, it gives a reasonable idea of the amount of cavitation that can be expected in the plasma, although, in total, it will always be an overestimate at the centre of the beam. Figure 3.8 shows the amount of cavitation expected across a wide range of the parameter J_0^2/ρ_0, again up to 3 ps. Good agreement can be seen, even in the most extreme case the analytic model is still giving a reasonable estimate of the magnitude of the cavitation at this time. Going beyond this, either by going to a

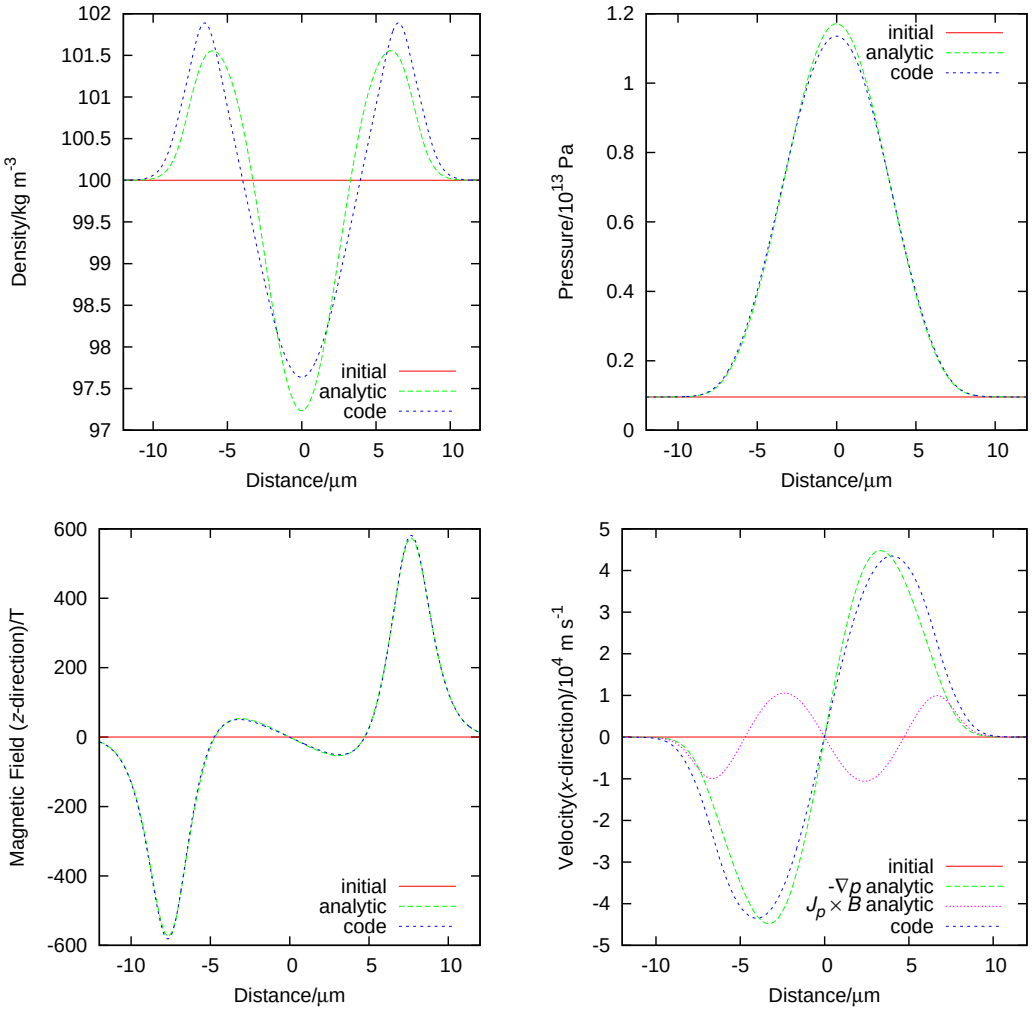

Figure 3.7: Plots of the density, pressure, magnetic field and velocity after 3 ps for $J_0 = 10^{16}$ A m^{-2} and $\rho_0 = 100$ kg m^{-3}. Otherwise the same values are used as in figure 3.4. In the plot for velocity the analytic contribution from the pressure gradient and $J_p \times B$ force are shown separately, demonstrating the dominance of the pressure gradient.

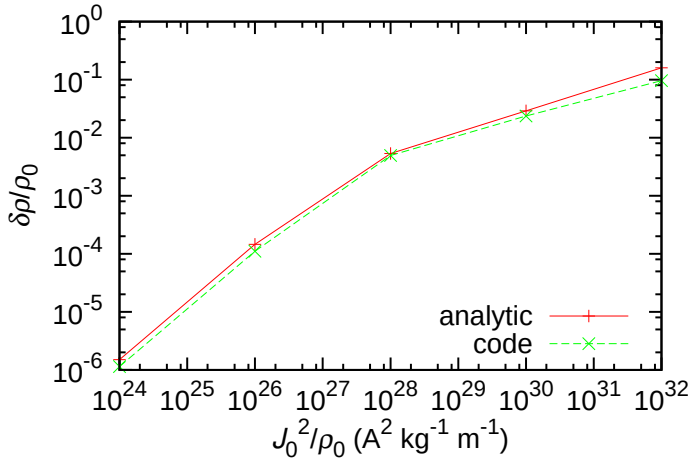

Figure 3.8: A comparison of the parameter $\delta\rho/\rho_0$ for the analytic consideration against the MHD code. The profile is again compared at $t = 3$ ps, and other parameters are as used in figure 3.4.

later time or increasing J_0^2/ρ_0 means the analytic model will start to break down.

3.4.1 Shocks

If the return current is driven for long enough, at a high enough current density and low enough mass density, shocks can form in the plasma. In figure 3.9 an example is shown for a return current of 10^{17} A m^{-2} and a mass density of 10 kg m^{-3}. The return current however is only applied for 3 ps, and after that it is switched off. At 5 ps the beginning of the shock formation can be seen by the steepening of the density gradient, at 7 and 9 ps the shock front has become very steep, and finally by 11 ps a sharp shock front has been formed. Because of the extreme amount of cavitation in this situation the analytic model can not be expected to give sensible results here.

From figure 3.9 it can be seen that essentially a blast wave has been produced in in this case. This is not unexpected, as a lot of energy has rapidly been dumped into a small volume. It should be noted that figure 3.5 shows only the time taken for $v_{max} > c_s$, and not the time for a well defined shock to form, as is only seen after $\sim$7 ps in figure 3.9. Not included in the MHD code is the effect of radiative

heating, in this regime it will certainly have an effect on the form of the shock front obtained [34].

The results from the MHD code can be compared to the self-similar solution for a blast wave. This is a problem first considered by Sedov [89], to determine energy yield given a shock wave at a radius r after some time t. The similarity solution is possible because the gas motion is determined solely by the initial energy, E_0 and the density of the gas the blast wave is moving in to, ρ. These parameters do not combine to give a distance or time, so the flow looks the same at all temporal and spatial points. The solution to the self-similar motion, for a planar blast wave, is given by [90]

$$r = K \left(\frac{E_0}{\rho} \right)^{1/3} t^{2/3}, \tag{3.33}$$

where K is a dimensionless parameter, given by [34]

$$K = \left(\frac{75}{16\pi} \frac{(\gamma - 1)(\gamma + 1)^2}{(3\gamma - 1)} \right)^{1/3}, \tag{3.34}$$

also for a planar blast wave.

Figure 3.10 shows the results from the code, for the problem shown in figure 3.9, compared against the results from the analytic self-similar solution shown in equation 3.33. The radius of the blast wave from the code is shown from 10 ps, when the shock becomes well formed, up to 100 ps. Good agreement between the analytic case and the code is seen. The small discrepancy is likely due to the fact that the blast wave simulated in the code is not a true point explosion, but the energy is deposited over 3 ps and across a width on the order of 3 µm. The energy used in the analytic solution is the total energy deposited, which is 2.6 $\times 10^8$ J m^{-2}.

3.5 Two Dimensional Hydrocode

One challenge to overcome with fast ignition is the problem of the large divergence angle of the electrons that are created by the laser pulse [91]. These will not efficiently heat the core of the fuel, as much of their energy will be wasted.

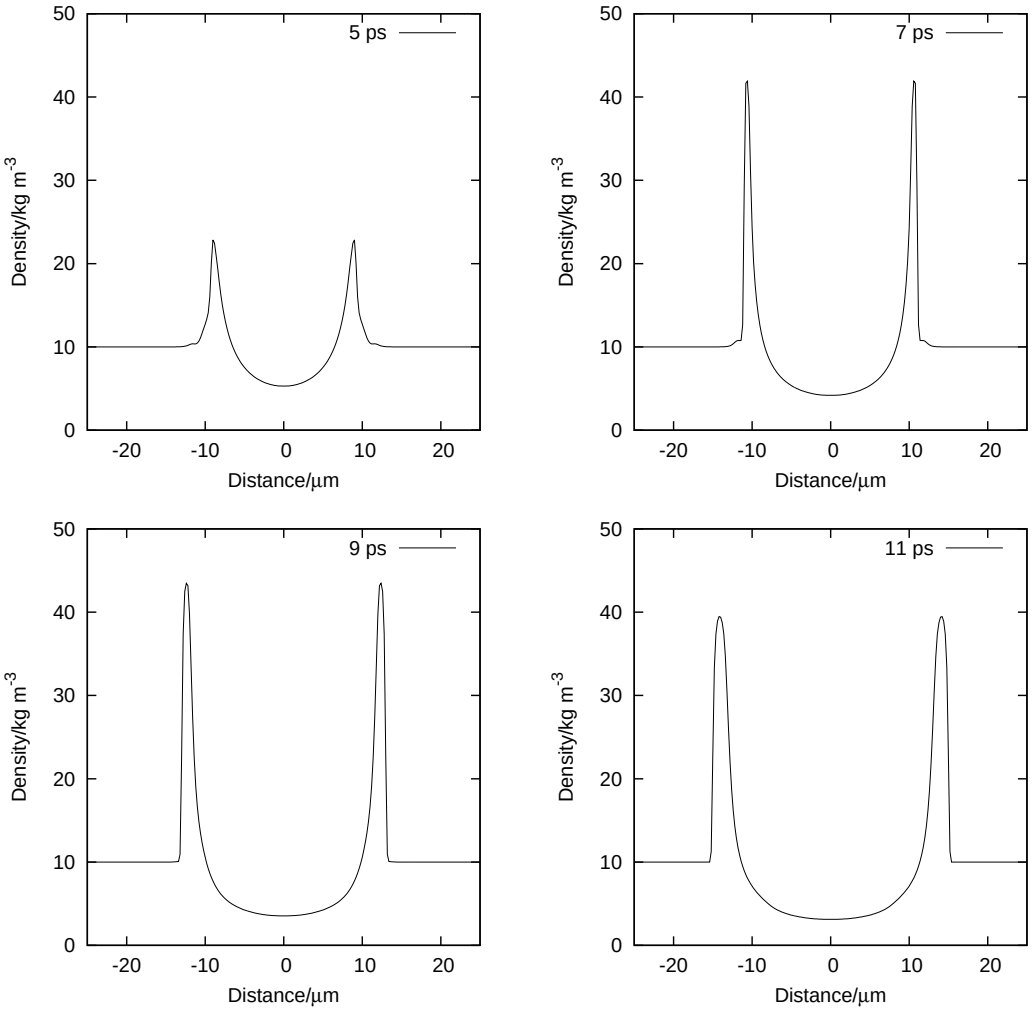

Figure 3.9: Density plots from the MHD code showing shock formation caused by the resistive return current. The initial parameters in this case were $J_0 = 10^{17}$ A m^{-2} and $\rho_0 = 10$ kg m^{-3}, other parameters were the same as for the results shown in figure 3.4. After 3 ps the fast electron current was switched off, such that $J_0 = 0$ for $t > 3$ ps.

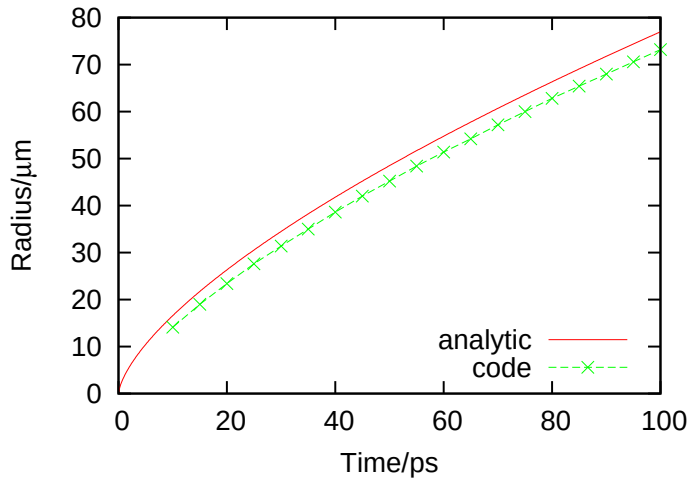

Figure 3.10: A comparison of the radius of the blast wave from the code against the analytic self-similar solution. The initial set up is the same as that shown in figure 3.9, such that $\rho = 10$ kg m^{-3}, $E_0 = 2.5 \times 10^8$ J m^{-2} and $K = 1.2$.

One way to overcome this problem would be to use a structured collimator to control the spread of the electrons. This is achieved by through resistivity gradients, for example in a solid cone shaped target [85, 92]. It has been shown that such a resistivity gradient can successfully restrict the spread of the electrons [93].

One potential problem is what would happen to the structured collimator itself, over the duration of the high-powered laser pulse. Over the 10 - 20 ps duration of the laser pulse the collimator will undergo extremely rapid Ohmic heating, due to the resistive return current induced by the forward going relativistic electrons.

Hydrodynamic simulations of such structured collimators are necessary to explore this effect. A two dimensional version of the code discussed in section 3.3 was created to look at this problem. Magnetic fields were not included, which is justified on the basis of the relative strength of the $J_p \times B$ force compared with the Ohmic heating established in section 3.2.4. Thermal conduction, detailed in section 2.4.5, is included in the code. Also, the difference in temperatures for the ions and electrons can be of importance in laser produced plasmas, so separate temperatures are used for the ions and electrons, as discussed in section 2.4.8.

Implicit methods, as described in section 2.5.5, were used for both the thermal conduction and the ion-electron thermal equilibration. The full code is not included here, due to the fact that it broadly follows the same Ziegler scheme as shown in section A.1 of appendix A, albeit without the mangetic fields, and with Euler's method replacing the Runge-Kutta 2 method previously used. The modules to solve the thermal conductivity and ion-electron equilibration terms have been included in section A.2 of appendix A.

3.5.1 Comparison of 1D and 2D Hydrocodes

One method to check the two dimensional hydrocode was working as expected was to run problems that were inherently one dimensional and compare them against the results from the 1D MHD code. Figure 3.11 shows the results from such a comparison. The initial conditions are given by

$$\begin{bmatrix} \rho \\ v_x \\ p_{tot} \end{bmatrix}_L = \begin{bmatrix} 1 \\ 0 \\ 1 \end{bmatrix} \qquad \begin{bmatrix} \rho \\ v_x \\ p_{tot} \end{bmatrix}_R = \begin{bmatrix} 0.125 \\ 0 \\ 0.1 \end{bmatrix}, \tag{3.35}$$

where dimensionless units are again used, and there are no magnetic fields. This is a standard problem known as Sod's shock tube [68]. In the two dimensional hydrocode thermal conduction was switched off for this test. The ions and electrons were initialised with the same temperature, and with $Z = 1$, such that $p_i = p_e = p_{tot}/2$. $\gamma = 5/3$ is used in this case.

The two dimensional runs each had a grid size of 200×200. Two runs were done, one with the left and right hand sides of the problem as $x < 0.5$ and $x > 0.5$ respectively (the x run), and one with the left and right hand sides of the problem as $y < 0.5$ and $y > 0.5$ respectively (the y run). As there was no initial variation along the y-axis for the x run, the values along the y-axis were identical for a given x, and vice-versa for the y run. The results from these two runs and the one dimensional run shown in figure 3.11 demonstrate good agreement.

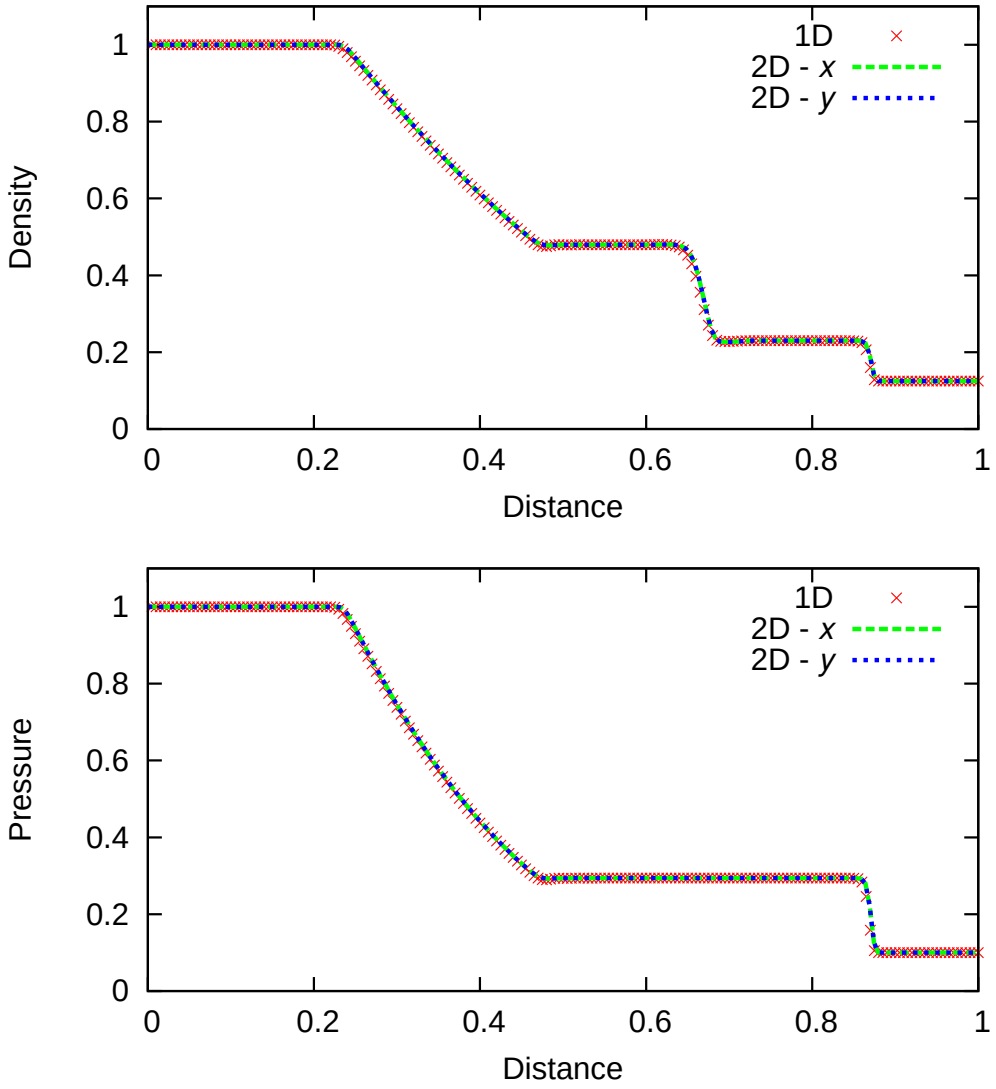

Figure 3.11: A comparison of the 1D and 2D code results, where the 2D code was set up with the same one dimensional problem in the x and y directions, to verify the code was working correctly. The initial set up is for $\rho = 1$, $p = 1$ for $x \leq 0.5$, $\rho = 0.125$, $p = 0.1$ for $x > 0.5$. 200 grid cells were used.

3.5.2 Sample Result

Figures 3.12 and 3.13 show a selected problem used to test the code. This was for a set-up where the electron temperature profile is given by the equation

$$T_e = 400e^{-\frac{x^2}{2\sigma^2}} + 100 \text{ eV}, \tag{3.36}$$

where $\sigma = 25$ µm, while the ions and electrons outside this strip have a temperature of 100 eV. The density in this region was 2700 kg m^{-3}, while the rest of the background was at 2.7 kg m^{-3}. The atomic number was fixed at $Z = 1$ and the Coulomb logarithm at $\ln \Lambda = 10$. Although this is intended as a demonstration simulation, the temperature profile and density would be of relevance for a structured collimator at solid density, within a low density background plasma. For example, the values used here can be compared with the temperatures and scale lengths in figures 4.15 and 4.9, shown in chapter 4. The figures demonstrate a difference in the ion and electron temperatures, due to the thermal conductivity of the electrons.

There are still outstanding stability issues with the code, meaning the Courant number, as described in equation 3.30, was reduced to $C = 0.0007$. This outstanding issue needs to be resolved before doing further simulations. An example of the instability growth for a Courant number of 0.7 is shown in figure 3.14, where a cell to cell instability can be seen. The instability has been shown where the plasma is expanding in the $x - y$ direction, the initial problem being set up as a square of hot dense plasma expanding into a cooler, lower density plasma. The instability seen forming disappears when a smaller Courant number is used.

3.6 Summary

In this chapter a simple analytic model has been used to widely explore the parameter space where cavitation is likely to occur. The accuracy of this model has been verified by a comparison with the 1D MHD code that has been developed.

The analytic model has shown that the pressure gradient term, due to Ohmic

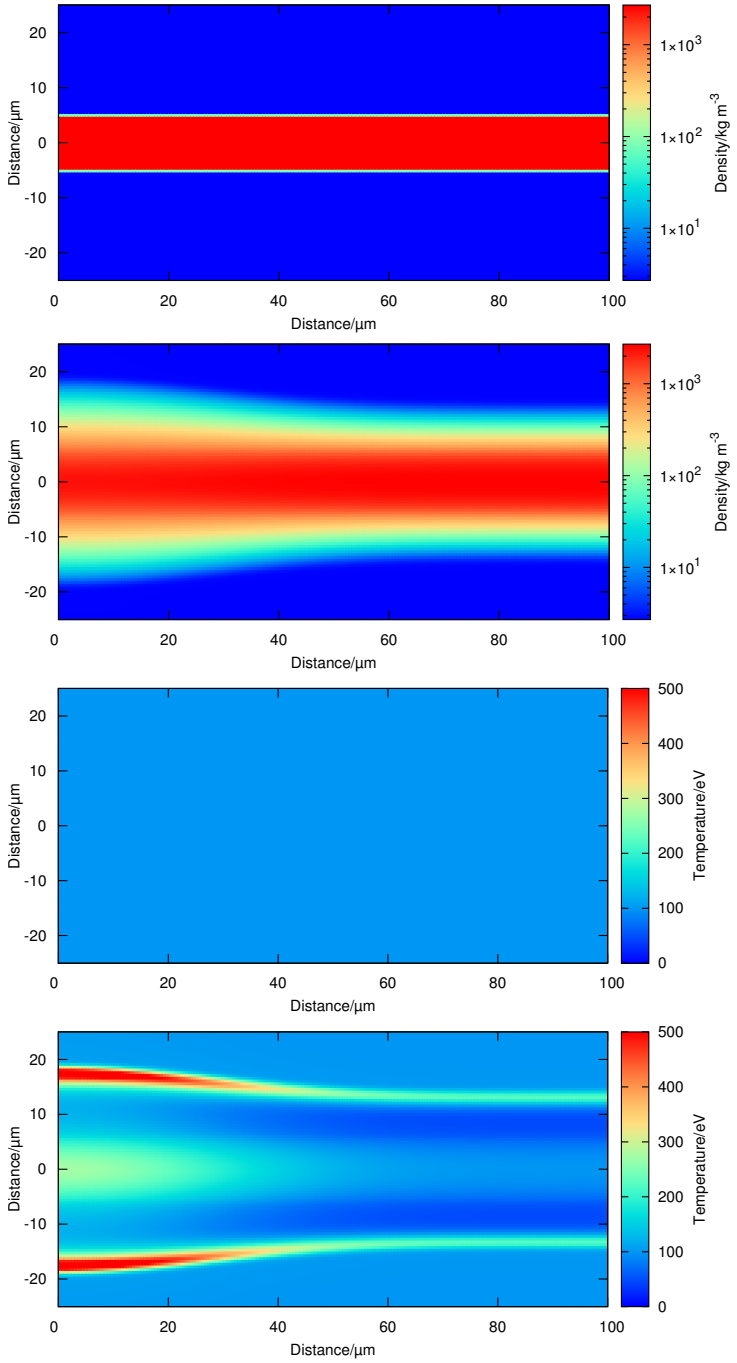

Figure 3.12: From top to bottom: the density at $t = 0$, the density at $t = 20$ ps, the ion temperature at $t = 0$ and the ion temperature at $t = 20$ ps for the set-up described in section 3.5.2.

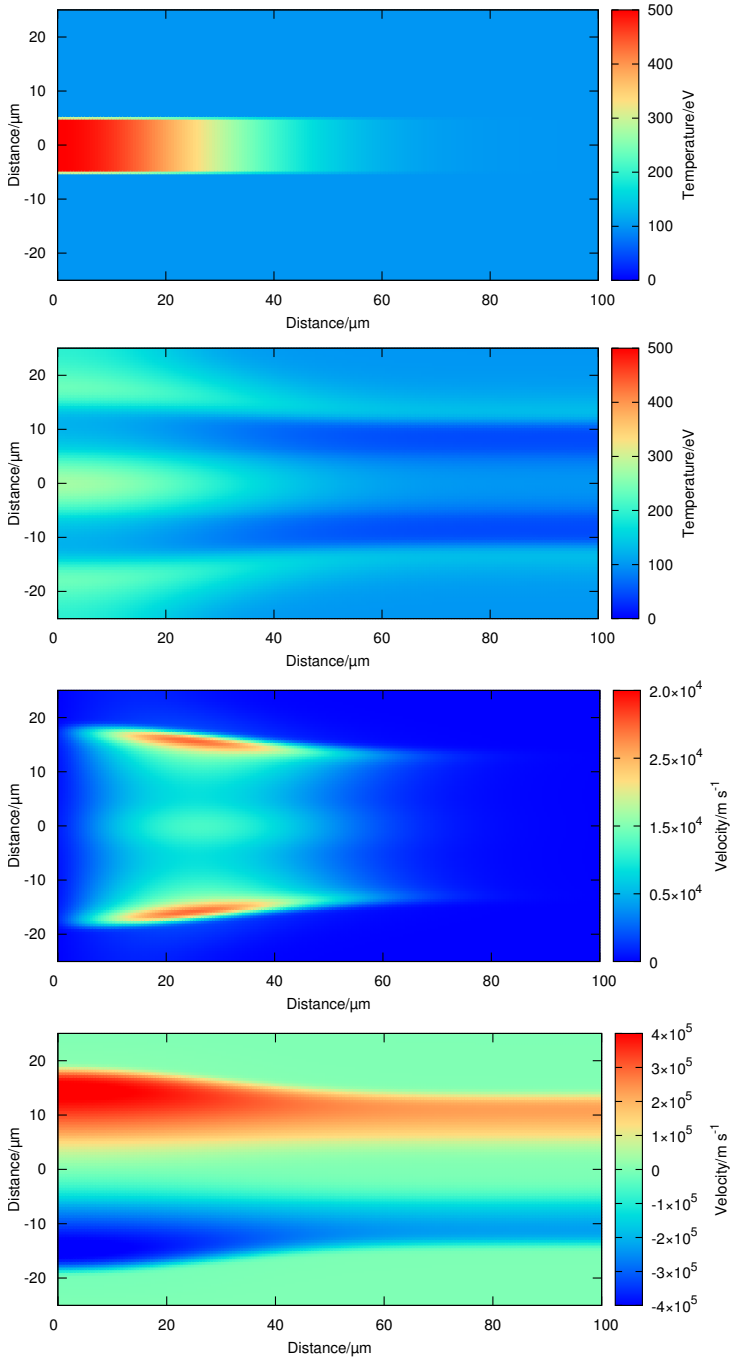

Figure 3.13: From top to bottom: the electron temperature at $t = 0$, the electron temperature at $t = 20$ ps, the x-direction velocity at $t = 20$ ps and the y-direction velocity at $t = 20$ ps for the set-up described in section 3.5.2.

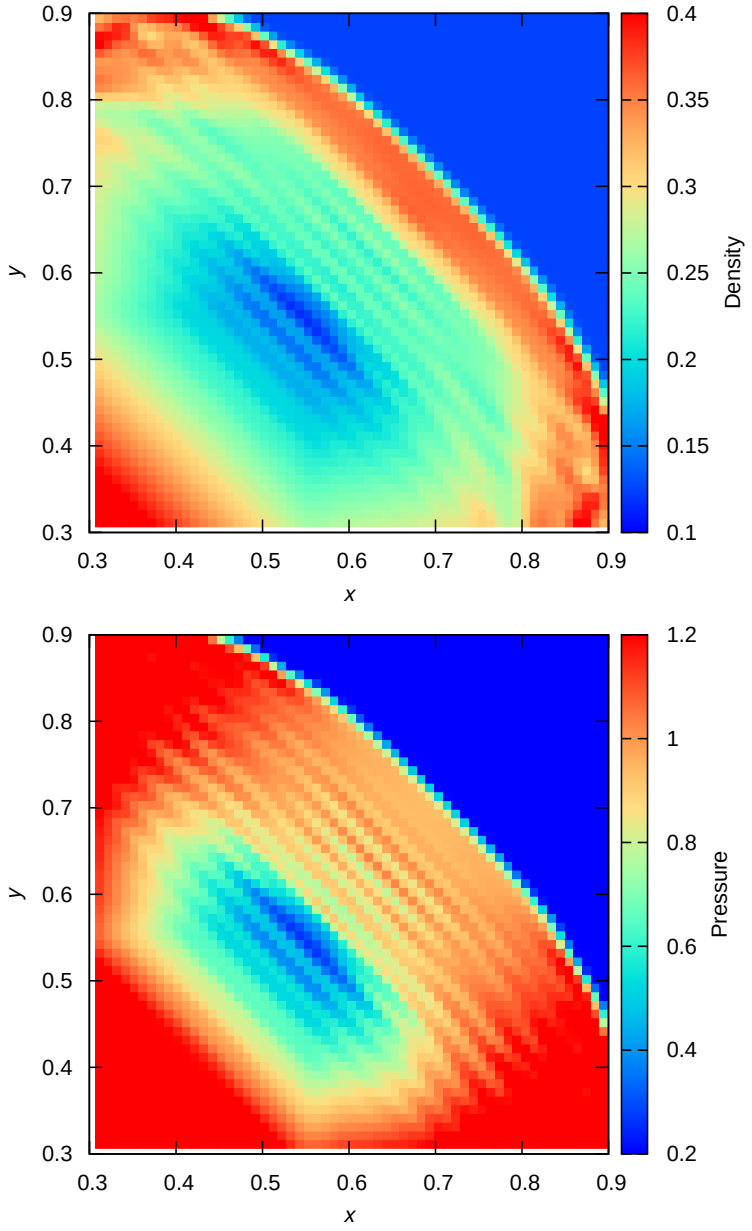

Figure 3.14: Top: the density for the simulation run showing the cell to cell instability, at $t = 0.09$. Bottom: the pressure showing the same instability at the same time. The run initially had $\rho = 1$ and $p_i = p_e = 5$, for $(-0.5 < x < 0.5) \wedge (-0.5 < y < 0.5)$, $\rho = 0.1$ and $p_i = p_e = 0.05$ otherwise, and $v_x = v_y = 0$ everywhere. The run used 200×200 cells over a spatial grid of -1 to 1. No thermal conduction is included, and dimensionless units are used. The Courant number was 0.7.

heating, dominates the cavitation process. The $J_p \times B$ force is less significant, and towards the centre of the electron beam actually opposes the cavitation process. Good predictions from the analytic model were obtained for the density, pressure, magnetic field and velocity.

It has been shown that for parameters of interest to fast ignition the cavitation effect can be significant, even after just 3 ps. The good agreement between analytic theory and fully non-linear MHD simulations gives confidence that cavitation is relevant to fast ignition. Similarly shocks can be formed in fast ignition relevant plasmas after just a few ps. These were predicted by the analytic model and an example from the MHD code has been shown.

Some work was undertaken in looking at the two dimensional hydrodynamic response of plasma to a return current. Further work is needed to ensure the stability of the code, and it would be desirable to add magnetic fields into the code to perform similar simulations to those for one dimensional code. The ability to model materials with a mixed Z would also be useful to more accurately model structured collimators.

Chapter 4

Effect of Defocusing on Laser-Coupling into Gold Cones

4.1 Motivation

Cone-guided fast ignition was introduced in section 1.5, and is illustrated in figure 1.9. The coupling of laser light to hot electrons via the cone is important in cone-guided fast ignition; in terms of both the total energy in the hot electrons and their energy spectrum. If there is insufficient energy in the hot electrons to heat the hotspot, or the electrons do not deposit their energy in the compressed core of the target, then ignition will not be achieved. In section 1.3.6 it was stated that the areal density of the hotspot needs to be greater than $\sim$0.3 g cm^{-2}, to ensure that the fusion borne α-particles deposit a significant amount of their energy within the hotspot, causing it to self-heat. However, the mass of the hotspot must be limited in order to allow for useful levels of gain, therefore having a hotspot with an areal density greater than the minimum required is undesirable. Electrons with an energy of 0.5 - 1 MeV will have a comparable range to 3.5 MeV α-particles, as produced by the DT reaction, in the hotspot [36]. The electron kinetic energy for a given laser intensity was discussed in section 1.5.2. To produce hot electrons at the cone tip with a suitable range in the hotspot requires that the value of $I\lambda_L^2$, for the igniter laser, is less than 10^{20} W µm^2 cm^{-2}.

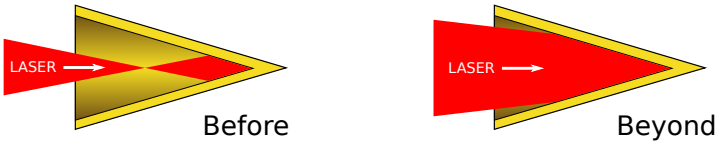

Figure 4.1: Focusing the laser before the cone tip and beyond the cone tip. In this chapter the convention is used that a negative defocus position is before the cone tip and a positive defocus position is beyond the cone tip.

To achieve sufficient heating of the hotspot, the heat flux must be around 10^{20} W cm^{-2}. This is determined by the hotspot size, which has a diameter of $\sim$10 µm, and the fact that the fuel only stays assembled for 10 - 20 ps, due to its non-isobaric configuration. The intensity of the laser required is higher still, at 10^{21} W cm^{-2}, due to limited coupling efficiency of the laser light into hot electrons. This causes an inconsistency in the laser requirement for laser light with a wavelength around 1 µm; what is required is a method of keeping the electron temperature low, while still maintaining the required heating power to the hotspot. This could be achieved by using shorter wavelength laser light; for long pulse lasers frequency tripled 3ω light can be generated at efficiencies of up to 80% [94]. However, for high intensity short pulse lasers of the type required for fast ignition this has not yet been attempted. The results in this chapter show a way of softening the energy spectrum of the hot electrons, while maintaining the laser to hot electron energy coupling. However, these experiments are conducted for much lower energy pulses, of much shorter duration, than those which are required for fast ignition, so caution must be exercised in extrapolating the findings to that scale.

To better understand the physics of the laser energy coupling, and the resulting spectrum of the fast electrons, experiments looking at the electron production from a high powered laser interacting with a gold cone are of interest. There are a variety of diagnostic techniques that can be used to give information about the total laser energy coupling and the spectrum of the hot electrons that are produced. This chapter concentrates on an experiment that took place during November - December 2008, on the Vulcan Petawatt laser at the Central Laser Facility, STFC Rutherford Appleton Laboratories in the UK.

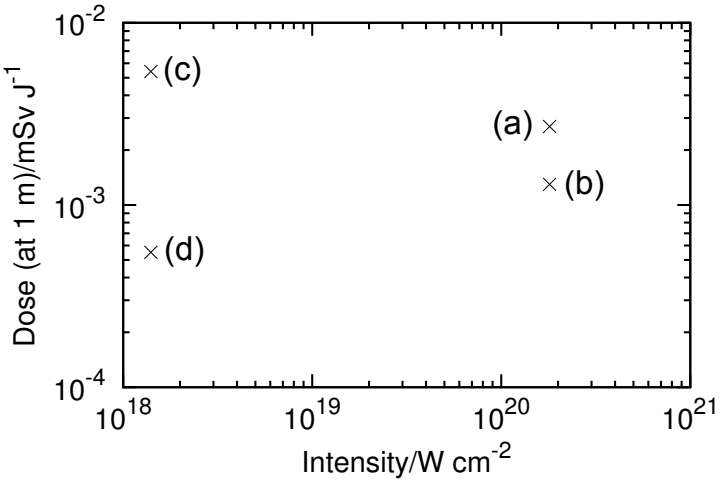

Figure 4.2: Results from the Titan laser show unexpectedly good coupling when the laser is focused beyond the cone tip. (a) and (b) show tight focus shots, (c) shows a shot where the laser was focused before the cone tip and (d) a shot where the laser was focused beyond the cone tip. Results included courtesy of R. Clarke. Data is unpublished, but the experimental set-up is described in reference [95].

This experiment was motivated by results from a different experiment on the Titan laser, at the Jupiter Laser Facility, Lawrence Livermore National Laboratory in the US. In the Titan experiment a high powered laser was fired into copper cones, with 25 µm thick walls [95]. Some shots were taken with the position of the cone such that the laser was not focused tightly to the cone tip, but before or after it, as shown in figure 4.1. Figure 4.2 shows the results from this experiment. Although there was only one shot each for the before and after defocus geometries, the surprising result was that when the focus of the laser was beyond the cone tip, the energy coupling appeared to be enhanced. The energy coupling was inferred by a TLD (Thermoluminescent Dosimeter) diagnostic, which measures the hard X-ray dose emitted from the target [96]. The TLD is sensitive to photons with energies of 6 keV and above, so it can be inferred that the higer does is due to enhanced K_α emission from the cone, which itself is due to increased coupling of laser energy to hot electron energy. The Vulcan Petawatt experiment aimed to further investigate the energy coupling where the laser was not focused tightly on the cone tip.

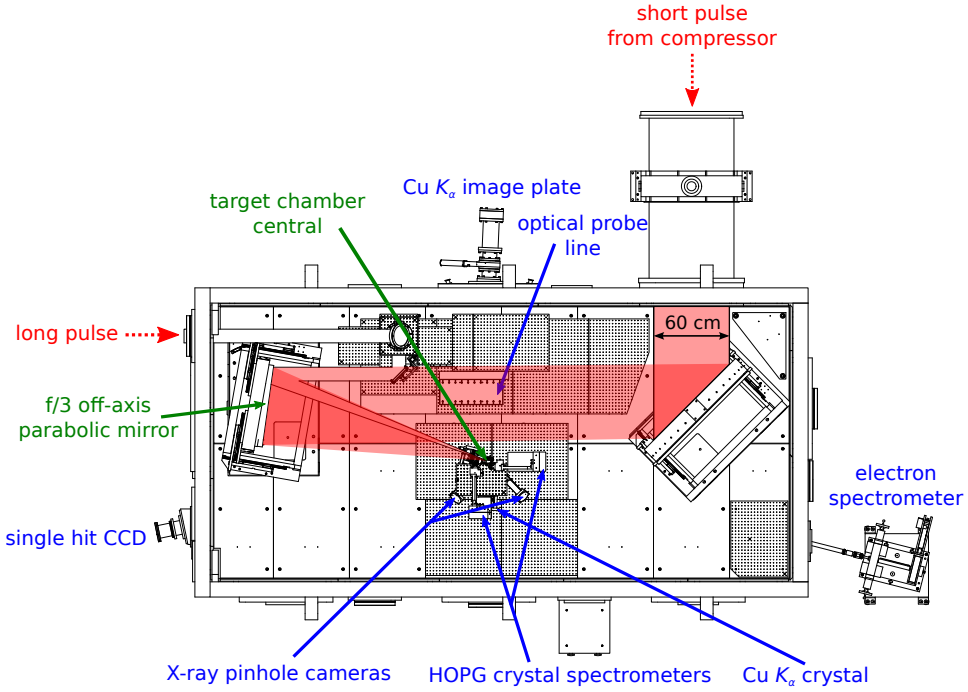

Figure 4.3: Layout of the target chamber for the experiment. Image adapted from engineering plan created by P. Brummitt.

4.2 Experimental Set-Up

The experimental set-up in the target chamber is shown figure 4.3. The targets used were gold cones, with copper wires attached to act as a diagnostic for the hot electrons. The diagnostics used were a copper K_α imager, a pair of HOPG spectrometers, an electron spectrometer, X-ray pinhole cameras, a single hit charge coupled device and an optical probe. Image plates were used in most of these diagnostics to record the data.

The target chamber was under a vacuum of $\sim 10^{-6}$ mbar during the experiment. It took approximately one hour for the target chamber to reach this vacuum level. All of the diagnostics were able to record data for four shots without letting the chamber up. This was achieved by using a combination of motorised drives and gate valves to change the image plates. The targets were mounted onto a target wheel, and by the use of a motorised translation stage they could be aligned using the laser retro system, as described in section 4.2.2.

4.2.1 The Vulcan Petawatt Laser

Vulcan Petawatt [97] is a neodymium glass laser, with a wavelength of 1.053 µm. Pulse lengths used in the experiment were 1 ps and shot energies were 600 ± 100 J, giving powers of $\sim 10^{15}$ W. The laser was focused by an f/3 off-axis parabolic mirror, into an 8 µm FWHM Gaussian focal spot, giving a peak intensity of up to 2×10^{21} W cm^{-2}. Measurements made during the experiment showed the intensity contrast for the main pulse was 10^{-7}, and the energy contrast 10^{-4}, with the pre-pulse lasting for approximately 1 ns. Linear polarisation of the laser was used.

4.2.2 Targets

The targets used in the experiment were gold cones with copper wires attached to the cone tip. Dimensions of the targets are shown in figure 4.4, along with a photograph of one of the targets used. The length of the cone was 1.5 mm, and they had a half angle of 20°, giving an entrance size of around 1 mm. The tip of the cone was a flat surface, 30 µm in diameter inside the cone. Outside the cone the tip diameter was 51 µm. Along the length of the cone the walls were 20 µm thick, and at the tip the thickness was 6 µm.

Over 50 were shot in total during the experiment. The targets were manufactured by the Target Fabrication group at the Central Laser Facility, where a new manufacturing technique was developed for the mass production of the cones [98]. A high-precision CNC mill was used to create a 5 × 5 array of copper mandrels in the shape of the cone, the mandrel was then plated with gold to the desired thickness. The process was refined to give a low surface roughness, around 1 µm inside the cone.

Attached to the end of each cone, by glue, was a copper wire, 40 µm in diameter and 1±0.2 mm long. The actual wire length for each target was recorded before each shot. The hot electrons generated in the cone tip travel down the wire and produce copper K_α X-ray emission. Details about the diagnostics employed to look at this emission are given in the following section.

The target alignment was performed using a retro system, which looked at the reflection of an infra-red alignment laser from the cone targets. The alignment

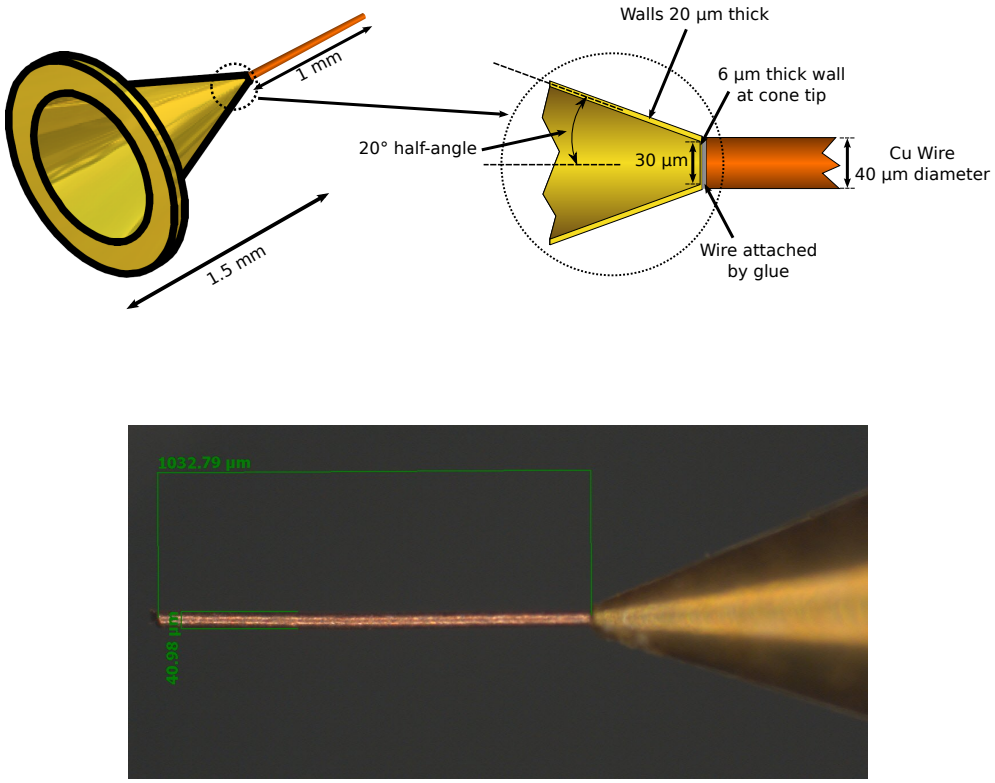

Figure 4.4: Top: diagram showing the dimensions of the cone-wire targets used in the experiment. Bottom: photograph of one of the cone-wire targets used in the experiment, courtesy of C. Spindloe.

laser followed the same path through the compressors as the main pulse, and the reflected light was imaged after passing back through the compressors. As the interior of the cone had a low surface roughness, of around 1 µm, the specular reflection made it clear whether the retro beam was on the cone wall, on the flat edge by the entrance of the cone, or on the cone tip. The targets were mounted on a translation stage to allow them to be moved to the best focal position of the parabola. For the defocused shots the alignment laser was initially focused tightly on the cone tip, and the target was then moved on the translation stage by the amount required for defocusing.

4.2.3 Copper K_α Imager

K_α emission is created by the transition of electrons from the second innermost (L) shell in an atom, to the innermost (K) shell. There are actually two lines, $K_{\alpha 1}$ and $K_{\alpha 2}$, due to the spin-orbit effect shifting the lines for different electron spins. In copper these occur at 8.048 keV and 8.028 keV respectively. The next closest line to K_α in terms of energy is the K_β line, due to transition from the third innermost (M) shell, at 8.905 keV [99].

The copper K_α imager employed in the experiment consisted of a Bragg reflecting crystal and an image plate (see section 4.2.7 for details about the image plates used). The crystal acts much like a curved mirror, focusing a very narrow spectral bandwidth of the X-ray emission. The crystal used in the experiment was quartz, SiO_2, with Miller indices of 2131. The crystal was 40 mm in diameter, but apertured to 20 mm. It was placed with a side on view to the target, perpendicular to the wire. The radius of curvature of the crystal was 500 mm, giving a focal distance of 250 mm. In the experiment it was placed 281 mm from the target, and the distance to the image plate was 2268 mm, resulting in an 8× magnification. A 20 µm thick copper filter was placed before the image plate.

The $2d$ spacing between the lattices of SiO_2 2131 is 3.082 Å. Using Bragg's law the the angle of the X-ray reflection can be determined,

$$n\lambda = 2d \sin\theta, \tag{4.1}$$

where n is an integer which determines the order the crystal is working in, λ the wavelength of the radiation being reflected, d the lattice spacing and θ the Bragg angle, which is the angle between the incoming radiation and the reflecting planes in the crystal. Figure 4.5 shows a schematic view of Bragg reflection from the planes in the crystal lattice. When the two rays are reflected such that their path difference is a multiple of λ, constructive interference occurs, resulting in a strong emission signal.

By applying this equation the Bragg angle for copper K_α emission, at 8.048 keV (λ = 1.540 Å), is found to be 88.7° in the second order, $n = 2$, as used in this experiment. Some details on the alignment and performance of such

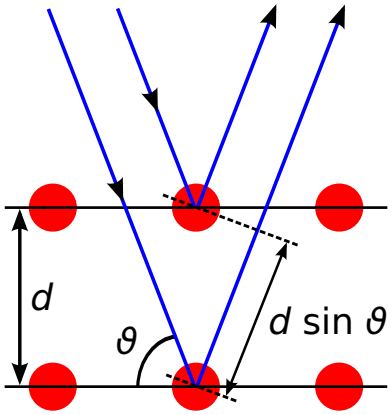

Figure 4.5: Illustration of Bragg reflection from the planes in a crystal. The path difference between two incoming rays, reflecting off different planes, has a total distance of $2d \sin \theta$.

a crystal are given by Koch *et al.* [100].

The imaging crystal has a narrow energy bandwidth, in an experiment with a similar copper K_α imager diagnostic by Akli *et al.* [101] the bandwidth was found to be 6 eV. This is due the limited size of the crystal, meaning only a small range of Bragg angles can be satisfied. This limited bandwidth poses a problem, as at high temperatures in the copper target the K_α emission line shifts in frequency and the bandwidth broadens. This prevents the imager from being a useful diagnostic for measuring the total yield of copper K_α radiation, although a correction can be made to account for this if the temperature in the wire is known [101].

4.2.4 HOPG Spectrometers

The HOPG (Highly Oriented Pyrolitic Graphite) spectrometers [102] that were fielded are also Bragg reflecting crystals. The crystals used however are mosaic, meaning the planes in the crystal are randomly distributed over a range of angles. This gives more chance for the the X-ray radiation to be diffracted by different mosaic blocks inside the crystal, increasing the efficiency of the spectrometer.

There are a number of effects that will lead to a broadening of the spectral lines detected by the HOPG crystal. The most straightforward is diffraction, due

to the finite size of the source (the copper wire), and the copper K_α line itself has a natural linewidth of 2.11 eV and 2.17 eV for copper $K_{\alpha 1}$ and $K_{\alpha 2}$ respectively [103]. The HOPG itself is not a perfect crystal and this has a defocusing effect, which can be determined by the rocking curve of Bragg reflections from the crystal. The dominant effect however is volume diffraction in the crystal, due to the fact there is a range over which the high energy photons penetrate into the crystal before being reflected. Higher energy photons will penetrate further into the crystal, with the mean free path $\propto \nu^3$, where ν is the X-ray frequency. This leads to broadening on the higher frequency side of the line [104].

In the experiment two identical HOPG crystals were used, with the planes in the crystal having a Gaussian distribution, with a FWHM of 0.4°, known as a ZYA crystal type. The spacing between the crystal planes was 3.354 Å. Equation 4.1 can again be used to find the Bragg angle. The crystals were operating in third order, $n = 3$, resulting in a Bragg angle of 43.6° for X-rays at 8.048 keV. The HOPG spectrometers were positioned above the target, perpendicular to each other, at a distance of 40 cm from the target. The results from the two spectrometers were averaged. The spectrometers had a spectral range of 800 eV, centred at 7.9 keV. This meant that both the copper $K_{\alpha 1}$, at 8.048 keV, and copper $K_{\alpha 2}$, at 8.028 keV, lines could be resolved. The spectral lines were recorded onto image plates, see section 4.2.7.

4.2.5 Electron Spectrometer

An electron spectrometer was used in the experiment. The spectrometer was aligned with the laser direction, as shown in figure 4.3, and contains a strong electromagnet to deflect the high energy electrons. The amount the electrons are deflected by is dependent on their energy as they enter the electron spectrometer. The electron spectrum was recorded on to Fujifilm BAS-MS image plates, similar to those described in section 4.2.7, but with a slightly different composition.

4.2.6 Pinhole Cameras

Pinhole cameras were used in the experiment to obtain an image of the X-ray emission. A pinhole camera consists of a small pinhole, with the X-ray image

being formed on an image plate. The clearest image from the pinhole cameras were obtained using an array of 20 µm diameter holes. The array was constructed from 250 µm thick tantalum, to help reduce background noise.

4.2.7 Image Plates

The image plates that were used in the experiment were Fujifilm BAS-SR, with the exception of the image plates used in the electron spectrometer, which were BAS-MS. In BAS-SR image plates the sensitive part of the image plate is a phosphor layer, made of 112 µm thick BaFBR:Eu^{2+} [105]. Above this is a Mylar ($C_{10}H_8O_4$) layer, 8 µm thick, to protect the sensitive layer. Below this there is a support layer to keep the IP rigid, and a magnetic layer to allow the IP to be placed into a scanner. A blue dye is added to the phosphor layer, which acts to absorb scattered light when scanning the image plates. This helps reduces the spread of the emitted light and prevents the spatial resolution being decreased [106]. The spatial resolution of the image plates is determined by the size of the scanning laser, which is 70 µm in diameter. The BAS-MS image plates differ slightly, full details are given by Meadowcroft *et al.* [105].

When X-rays or electrons interact with the image plate the Eu^{2+} sites are oxidised to Eu^{3+}. The electron is then trapped in the conduction band of the phosphor crystal. When the image plate is placed in a scanner it is scanned by a laser, with a wavelength $\lambda = 632.8$ nm, which excites the electrons to recombine and restore the Eu^{2+} sites. This decay is known as photostimulated luminescence (PSL) and releases photons, with a wavelength $\lambda = 400$ nm, which are recorded by the scanner. Random recombinations of the electrons with Eu^{3+} also occur, which are dependent on temperature and time. Fading times for BAS-SR image plates have been characterised by Tanaka *et al.* [107] and further characterisation for a variety of different image plates was done by Meadowcroft *et al.* [105].

The image plate response per incident X-ray photon varies with photon energy in a non-trivial way, peaking at around 15 keV. Previous work by others has looked at characterising this response for the different image plate types available [105, 106]. Similar work has looked at characterising the image plate PSL response for incident electrons over a range of energies [107].

With the exception of the copper K_α imager, the image plates were covered in aluminium foil, with a thickness of ∼20 µm. This acted as a filter and prevented the image plates being wiped from light in the room between consecutive shots. With knowledge of the X-ray or emission frequency, and the fade time, and the filtering used the total number of photons recorded on the IP can be determined. Fading times were particularly important in this experiment, as described in section 4.2 image plates could not be removed between shots, except for the copper K_α imager. This meant the fading time needed to be accounted for to compare the signal strength between shots.

4.2.8 Single Hit CCD

A single hit charge coupled device (SHCCD) is capable of detecting single X-ray photons, and recording their energy. Placing the camera a long distance from the target and using filtering is necessary to make sure that most exposed pixels on the CCD chip are seeing single photons from the laser shot only. Then, by taking into account the filtering and solid angle that the camera sees, the total copper K_α emission from the plasma can be determined. The use of a single hit camera in a petawatt environment is described in detail by Stoeckl *et al.* [108]. An SHCCD can also be used to determine the electron temperature in the plasma, by looking at the bremsstrahlung emission.

In this experiment the wire is not being directly illuminated by the laser, but heated by the hot electrons. This meant that the background noise on the shots for the cone-wire targets was very high, and made it difficult to determine the K_α yield on the SHHCD directly. However, shots were taken on copper foils, which could be cross-calibrated with the HOPG spectrometers. This allowed the HOPG spectrometer to determine the variation in copper K_α yield from shot to shot. Further information on determining the total yield seen by an SHCCD are given by Maddox *et al.* [109]

The SHCCD used in the experiment was a Princeton Instruments SX1300, with a chip consisting of 1300 × 1340 pixels, each 20 µm square in size. The filtering for the SHCCD consisted of 2 beryllium windows, totalling a thickness of 1 mm, 95 cm of air, 100 µm of copper and 50 µm of aluminium. Other materials

were present for the photons to pass through, but these were transparent to 8 keV X-rays. The SHCCD camera was situated at a distance of 4.36 m from the target.

4.2.9 Optical Probe

The optical probe took a small portion of the laser beam via a periscope, before it reached the parabolic mirror. This light was then converted to 2ω, with a wavelength of 527 nm, by a potassium dihydrogen phosphate (KDP) crystal. The optical light is then sent past the target to create a shadowgraph, with the light only being able to pass below the critical density, as given by equation 1.6. For the 527 nm light the critical density would be at 4×10^{20} cm^{-3}. However, refraction in the plasma and the finite size of the imagining optics means the cut-off for the highest density that can be imaged is actually lower than the critical density [110]. At densities above the cut-off density no optical probe light can be collected, so the shadowgraph will be dark. The setup used in this experiment gave a cut-off density of 5×10^{19} cm^{-3}; an identical setup was previously used by Lancaster *et al.* [111]. The images for the optical probe were recorded onto CCDs.

Light travels at 30 cm ns^{-1} in a vacuum, so the time at which the probe light passes over the target can be adjusted, relative to the timing of the main pulse, by moving the probe optics by modest distances. In this experiment the optical probe was constantly delayed 400 ps relative to the main pulse. Its view was side on to the target, and 2 channels were used, one for high magnification, one for low magnification. The light can propogate through the plasma up to the critical density (equation 1.6), . The wire expansion at 400 ps can be seen in the shadowgrams, and this can be used to infer the heating in the wire by comparing with simulation results.

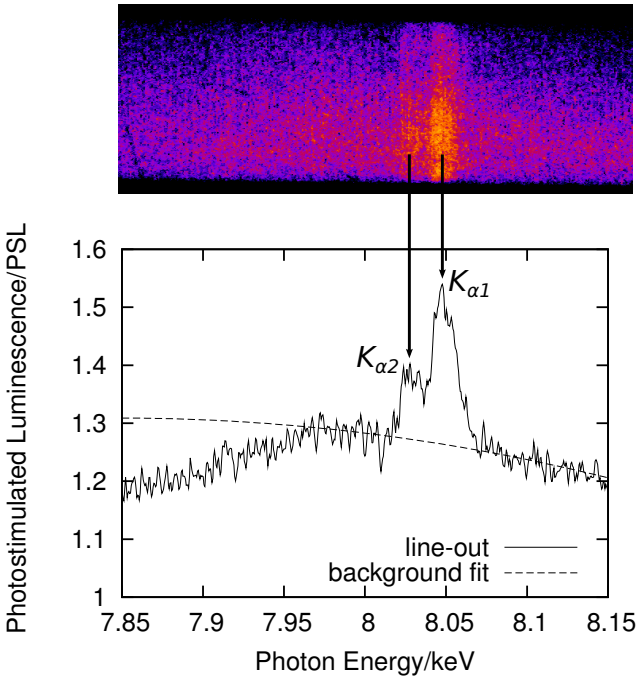

Figure 4.6: Image plate scan and raw line-out from one of the HOPG spectrometers. Copper $K_{\alpha 1}$ and copper $K_{\alpha 2}$ emission lines can be seen, as well as the bremsstrahlung background emission, which is fitted in the line-out by a polynomial. This is for a shot where the laser was focused 400 µm beyond the cone tip.

4.3 Results and Analysis

4.3.1 HOPG Spectrometer and SHCCD Cross-Calibration

A line-out from one of the HOPG spectrometers is shown in figure 4.6. Two emission lines, one for copper $K_{\alpha 1}$ and one for copper $K_{\alpha 2}$ can be seen. The line-out shown is the raw pixel value in PSL, averaged across the width of the recorded spectrum. To compare the yield between shots a correction for the bremsstrahlung background must be made, which was done by fitting a polynomial to the background of the X-ray spectrum, which is also shown in figure 4.6.

The signal on the SHCCD was too weak on the cone-wire targets to determine the copper K_α yield directly, as the copper wire was not being directly heated by

the laser. Two copper foils were shot to get a sufficient signal on the SHCCD, which were then used to calibrate the readings on the HOPG spectrometers. These copper foils were 1 mm squares, 25 µm thick, and mounted at a 45° angle to the laser normal.

Figure 4.7 shows a sample of raw data from the SHCCD, for such a copper foil shot, and a histogram of the events from the image. To start with a background image, taken on the SHCCD before the laser shot, was subtracted from the shot image. The events recorded on the SHCCD usually cover more than one pixel, due to some bleeding. The individual pixels need to be isolated from each other, so to separate out the X-ray events from background noise a slice value is chosen. Here it was chosen to be 100, and the camera records 1 count per 8.3 eV, so this corresponds to a photon energy of 830 eV. In this case the calibration of energy per count had already been determined on a previous experiment for the SHCCD camera, and it is verified by identifying the copper K_α, He_α and the copper K_β lines shown in figure 4.7.

Pixels that remain neighbouring to each other after the slicing are taken to be from the same event, up to a maximum group size, chosen to be 10. Any group bigger than 10 are assumed to be multiple events and are ignored. The events are then binned into discrete groups, here chosen to be every 10 counts. This process was automated in IDL, based on a program created by Andrew Ash, and further developed by Erik Wagenaars at the University of York.

The background signal is then subtracted from the copper K_α peak, as shown in figure 4.7. This gives the total number of copper K_α photons detected by the SHCCD. Correction factors must be added to this to determine the total number of photons emitted from the target. In this case 370 individual events were identified. However, only 2.5% of the counts were used in the analysis, due to multiple overlapping events, so from this 15,000 copper K_α events were inferred to be arriving at the chip. To get the total copper K_α emission the filtering, distance to target, and chip size, as described in section 4.2.8, need to be taken into account. The attenuation from the filtering was obtained from data provided by the Centre for X-ray Optics [112], and the chip efficency was 18%. The total was found to be 2.5 $\times 10^{13}$ K_α photons for the copper foil shot.

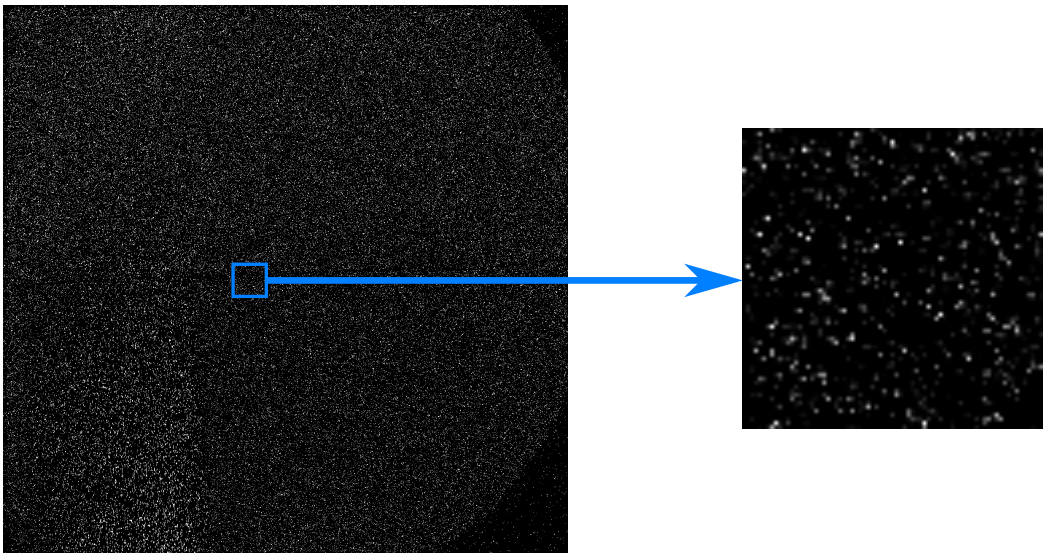

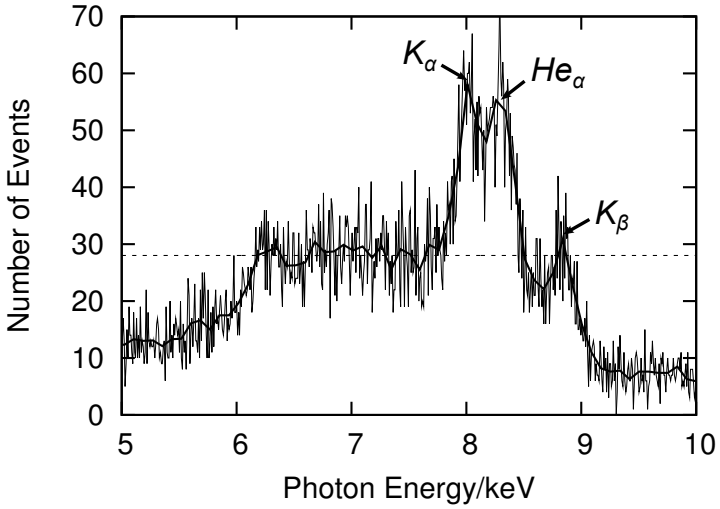

Figure 4.7: A raw segment of the SHCCD image for a shot on a copper foil. The graph shows the number of events for each pixel value recorded on the SHCCD. At around 8.0 keV the line can be seen for copper K_α, at 8.3 keV the He_α peak is seen, and at 8.9 keV the copper K_β line can be seen. The thicker line shows the binning for the histogram, and the dashed line shows the level taken as the background when finding the number of copper K_α events.

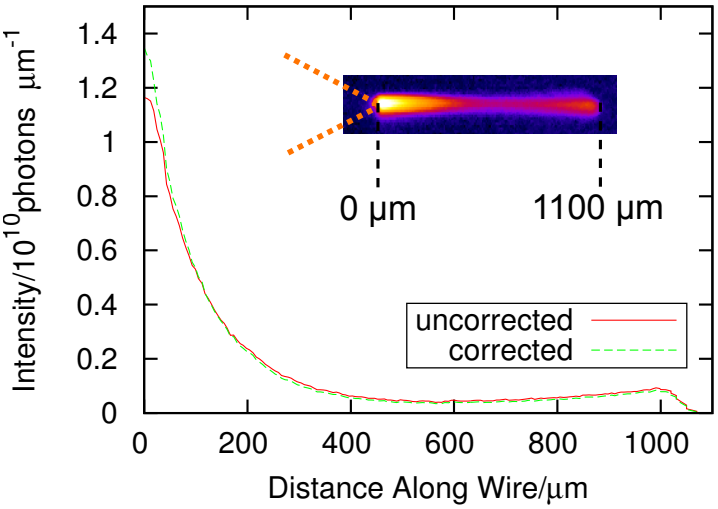

Figure 4.8: Image plate scan and line-out for the copper K_α imager, including the profile corrected for the shift in K_α emission at higher temperatures. There is an exponential fall-off with intensity along the wire, and an increase in brightness at the end due to refluxing. This result is for the same shot as shown in figure 4.6.

4.3.2 Other Diagnostic Results

Figure 4.8 shows a line-out and image plate scan for the copper K_α imager. This was for a shot where the defocus position was +400 µm, i.e. focused 400 µm beyond the cone tip, as shown in figure 4.1. To obtain the line-out the background signal was first subtracted by taking an average along the length of the wire above and below the region of emission. This was then subtracted from the average emission along the length of the wire. There is an exponential fall off in the copper K_α emission, starting from the cone tip, followed by a brightening at the end. The reason for the brightening again at the end is likely due to refluxing in the wire; as the hot electrons reach the end of the wire, still carrying a large amount of energy, they can escape. This causes a charge imbalance and an electric field to build up, slowing the electrons in this region [113].

As mentioned in section 4.2.3, the signal for the copper K_α emissions shifts and broadens at higher temperatures. A correction must be made for this, so that the scale length of the exponential fall-off can be determined between shots.

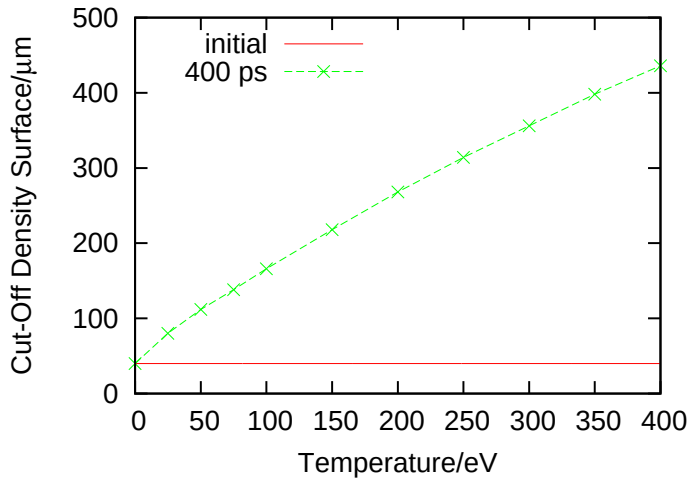

Figure 4.9: Simulation results from HYADES, performed by J. Pasley. The graph shows the diameter of the cut-off density surface, at 5×10^{19} cm^{-3}, after 400 ps, for a copper wire heated to a range of temperatures.

In particular the part of the copper wire closest to the cone, which undergoes the most heating, will underestimate the copper K_α emission the most. To correct for this simulations were performed by John Pasley, using the 1D radiation-hydrodynamics code HYADES [114]. By taking a uniform initial temperature through a copper wire for a range of temperatures, the position of the cut-off density, as discussed in section 4.2.9, at 400 ps was found. These values are shown in figure 4.9. This could then be compared against the data from the optical probe, and a correction factor based on work by Akli *et al.* [101] was applied. The corrected profile is shown alongside the uncorrected profile in figure 4.8. Both the corrected and uncorrected line-outs have the same area, or total photon yield, which was determined as described in the previous section.

Figure 4.10 shows a result from the optical probe. In the image at 400 ps the expansion of the wire and cone can be seen, due to plasma ablation at the target surface. To obtain the line-out a cut-off value was used, in terms of pixel brightness, such that the extent of the dark shadow could be determined.

Figure 4.11 shows the raw results from the pinhole camera used in the experiment with an array of pinholes. Emission from the outline of the cone can be seen.

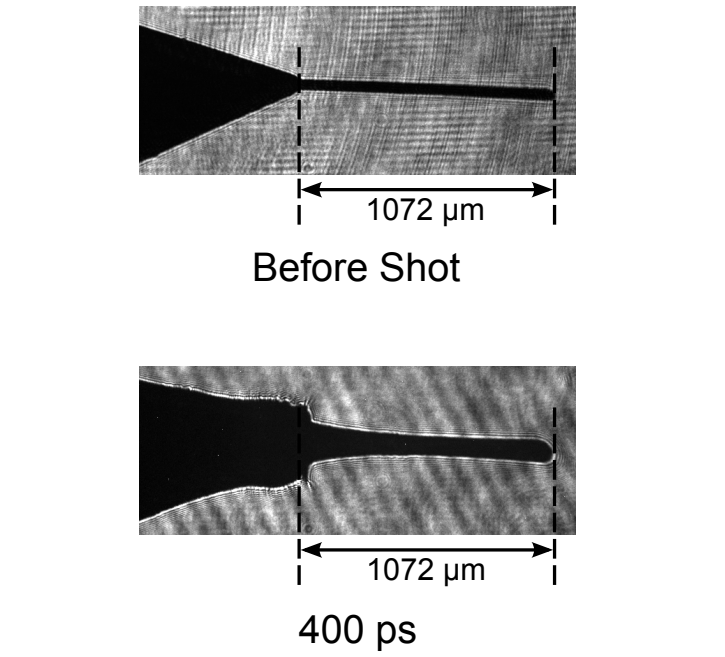

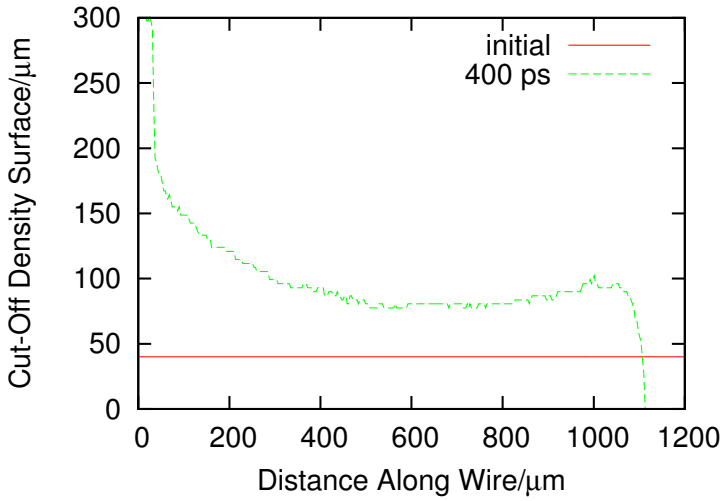

Figure 4.10: Images from the optical probe. Before and low magnification images are shown, the target was not moved between these images being taken. The lineout shows the expansion of the cut-off density surface, at 5×10^{19} cm^{-3} for 2ω laser light. This result was from the same shot as the results shown in figures 4.6 and 4.8.

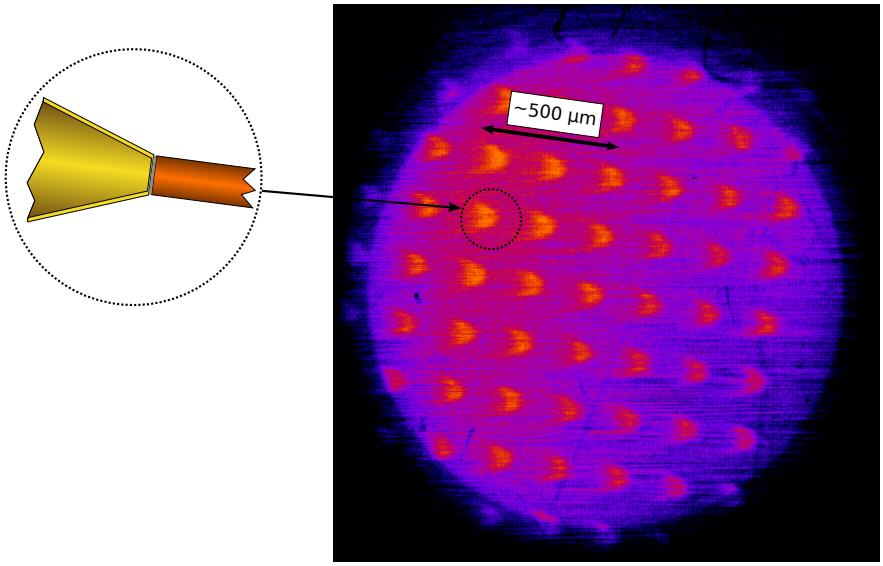

Figure 4.11: Image from the pinhole camera. The same image is repeated, showing the emission from the cone tip and very feint emission from the start of the wire. The cone-wire targets were shown in more detail in figure 4.4.

4.3.3 Total Copper K_α Yield

The fast electrons that enter the wire are well fitted by a two temperature distribution [115]. The colder temperature component is of most relevance; the hotter portion contains electrons with energies above the ∼1 MeV energy required for fast ignition. The copper K_α emission from the first few hundred microns in the wire is dominated by the colder temperature component of the fast electrons, while the hotter component is mainly responsible for the increase in emission at the end of the wire, as seen in figure 4.8.

Figure 4.12 shows the variation of total copper K_α yield from the target, in the first 250 µm of the wire, against the defocus distance, determined from the HOPG spectrometers as detailed previously in this section. The errors on the graph indicate the uncertainty between different shots, due to the high signal-to-noise ratio in the spectrum. The systematic calibration error from the SHCCD is larger, estimated to be ± 50%. In addition there would have been shot to shot variation, due to factors such as alignment of the targets, changes in the laser pulse and differences between the targets. The fraction of the emission from the

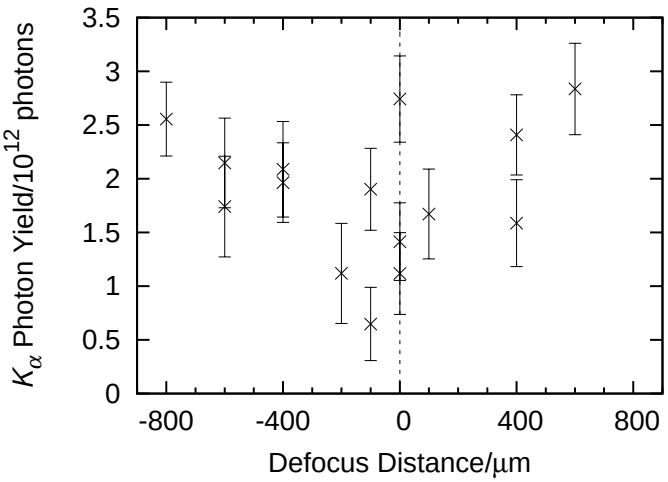

Figure 4.12: Copper K_α yield for a variety of laser shots. The data is based on the yield from the HOPG spectrometers, cross-calibrated against the SHCCD data, with a correction applied from the K_α imager to obtain the emission from the first 250 µm of the wire. Negative values indicate a focus before the cone tip, and positive values a focus beyond the cone tip, as shown in figure 4.1. The error bars show the uncertainty between shots, the total error from the calibration via the SHCCD is larger.

first 250 µm of the wire was determined from the corrected spatial information obtained by the K_α imager.

The total copper K_α yield has been shown to increase with increasing electron temperature, for a fixed energy, in simulations performed by Alec Thomas using the 2D hybrid Vlasov-Fokker-Planck (VFP) code, FIDO [116]. VFP codes work by evolving an electron distribution function in accordance with the VFP equation, as shown in equation 2.16. Copper K_α photon density production was calculated using relativistic binary-encounter cross sections [117] directly from the hot electron distribution function [118]. The total photon yield from the FIDO simulations ranged from 10.4×10^{12} photons at an intensity of 0.1×10^{21} W cm^{-2} up to 17.0×10^{12} photons at 1×10^{21} W cm^{-2}. These results are shown in figure 4.13. Ponderomotive (Wilks) scaling, as shown in equation 1.30, was assumed to determine the electron temperatures from the intensity. The peak intensity that corresponds to a particular defocus distance is shown in figure 4.14, these results

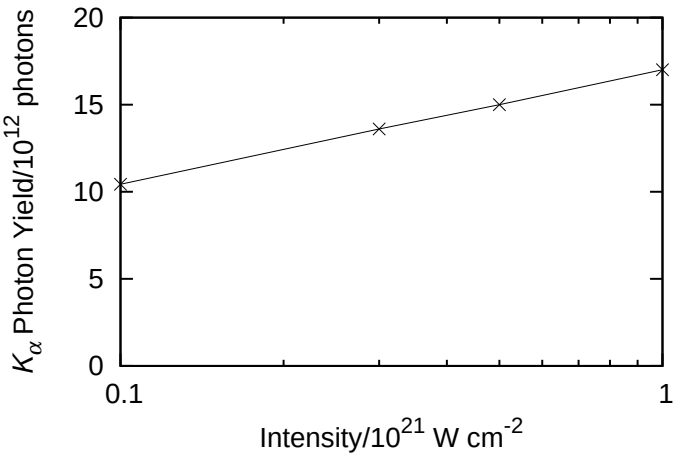

Figure 4.13: Calculated K_α yields in the first 250 µm of the wire, across a range of intensities, from the FIDO Vlasov-Fokker-Planck code. The total electron energy is held constant. Simulations performed by A. Thomas.

are from a ray tracing code that is detailed in section 4.3.5.

4.3.4 Copper K_α Emission Scale Length

In figure 4.15 the variation in the length along the wire over which the copper K_α emission falls to $1/e$ of its original value is shown. The $1/e$ scale length will become longer for higher energy electron distributions, as the electrons will travel further before being slowed by collisional stopping, as discussed in section 2.4.3. This is expected on the basis of previous studies which show the variation of hot electron temperature in a laser-solid target interaction as a function of laser intensity, as discussed in section 1.5.2.

Also shown in figure 4.15 are the scale lengths derived from the FIDO simulations. These are at intensities of 0.1, 0.3 and 1.0×10^{21} W cm^{-2}, corresponding to $\pm$800 µm, $-$275 µm and tight focus respectively, as shown in figure 4.14 and detailed in section 4.3.5. The FIDO results in figure 4.15 were convolved with a Gaussian with a standard deviation of 35 ± 10 µm, to account for the limited experimental resolution of the copper K_α imager. The line-outs for these results, with the convolution, are shown in figure 4.16. In these simulations

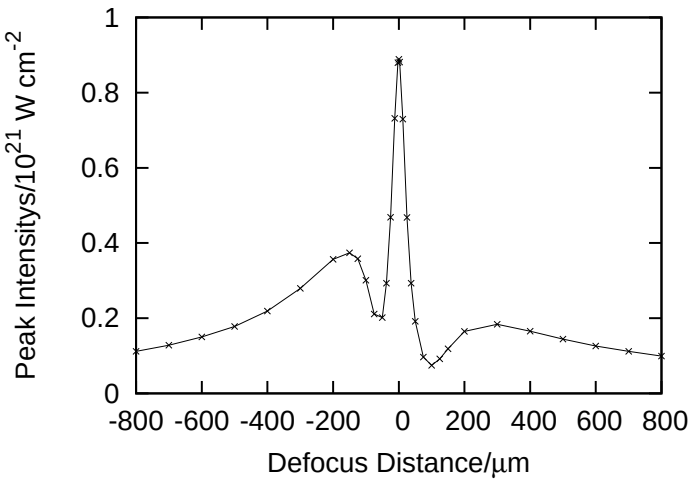

Figure 4.14: The variation of peak intensity inside the cone with defocus distance. The results shown are from a ray tracing code which is outlined in section 4.3.5, with a complete description given in appendix B.

-

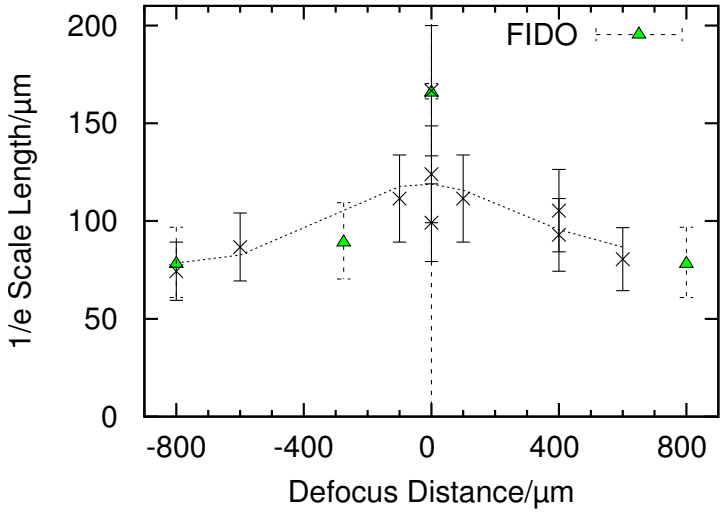

Figure 4.15: $1/e$ lengths from the copper K_α imager. The dotted line shows a moving average across ±400 µm for the experimental results. Also shown are the results obtained from the FIDO simulations.

a wire length of 250 µm was used, to keep the simulation run time reasonable. There is some discrepancy between the results shown in figure 4.8 and figure 4.16, especially towards the end of the wire. This is due to the sharp cut-off after 250 µm in FIDO. This means the fall off of the K_α emissions is artificially increased towards the end of the wire, after the convolution is performed to account for the detector resolution. This does not affect the validity of the code for finding the $1/e$ scale lengths however, as these values are all much less than 250 µm.

A correction also had to be applied to account for the 6 µm gold cone tip. This was done by comparing the electron stopping power of copper to gold, using the values given in the ESTAR database [119]. The ratio of the stopping powers is shown in figure 4.17. The corresponding amount, 6 µm, was multiplied by the ratio of the stopping power between gold and copper at the appropriate temperature, as given by ponderomotive scaling. The copper K_α emission over this distance was then cut off from the FIDO simulation results. Only a narrow bandwidth of bremsstrahlung emission from the cone would be seen by the copper K_α imager, which was much weaker than the copper K_α emission from the copper wire.

An electron spectrometer was also used in the experiment, and the results from this are shown in figure 4.18. This data was analysed be Sehar Sarfraz at the University of York. However the electrons that the electron spectrometer sees can be substantially different from the electrons generated by the interaction of the laser with the cone tip. This is due to electric fields that are created within the target as electrons escape, causing refluxing, as seen in figure 4.8 [49, 120]. In particular low energy electrons are less likely to escape the target, and high energy electrons will have their energy reduced, complicating the analysis of the electron spectrum. For this reason the $1/e$ lengths shown in figure 4.15 are a more robust indicator of the electron spectrum than the electron spectrometer data. Despite this the data shown in both of these figures is mutually supporting, showing the same overall trend. More data points are given for the electron spectrometer, this is because on some shots the CCD cameras used for the optical probe failed to trigger.

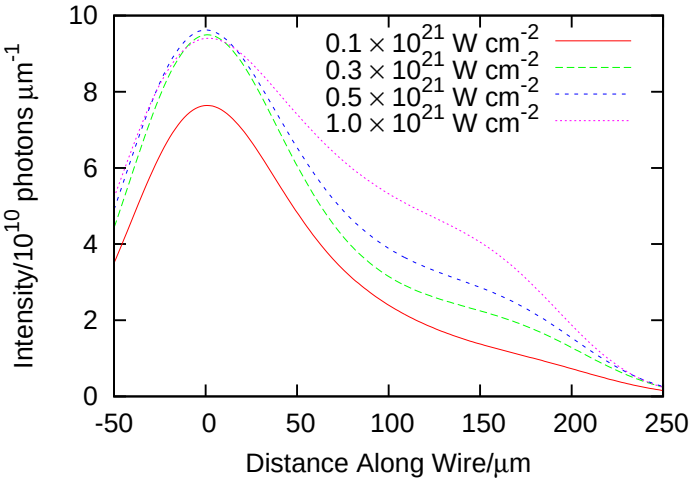

Figure 4.16: Profiles of the copper K_α yield along the wire over the range of intensities used in the experiment. Simulations performed by A. Thomas. The simulation results were convolved with a Gaussian with a standard deviation of 35 µm to account for the limited experimental resolution of the copper K_α imager, and a correction was made for the gold cone tip. The peak of the copper K_α emission is taken to be at the start of the wire, i.e. zero on the x-axis. The wire length in these simulations was 250 µm.

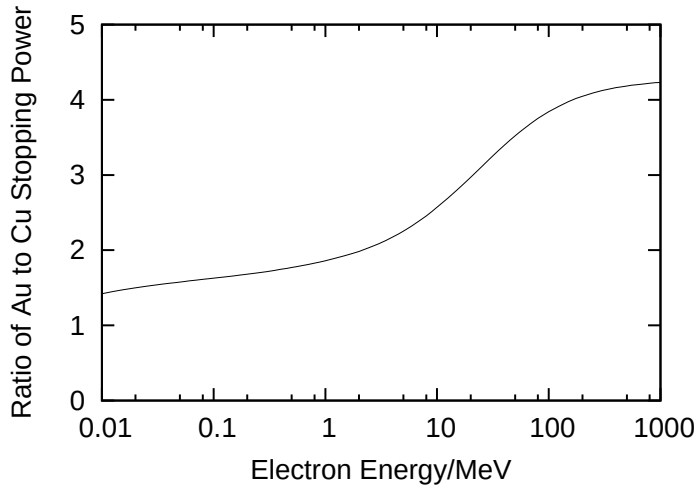

Figure 4.17: The ratio of the fast electron stopping power in gold to copper. Values obtained from the ESTAR database [119].

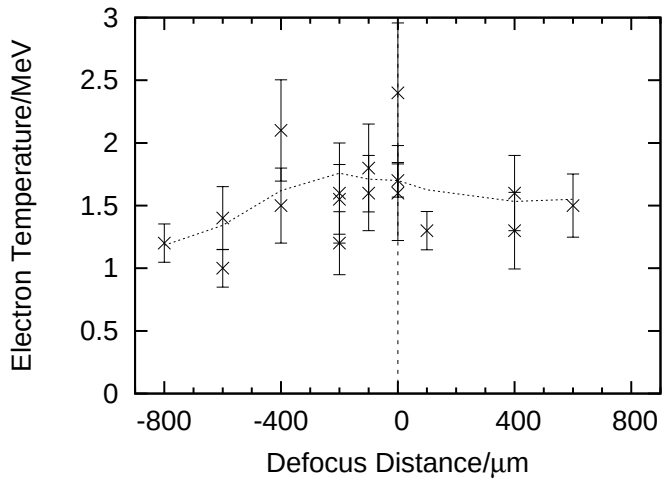

Figure 4.18: Electron spectrometer derived temperatures for the fast electrons. The dotted line shows a moving average across ±400 µm. Data analysed by S. Sarfraz.

4.3.5 Ray Tracing

To determine the change in intensity along the cone walls in the defocused cases a ray tracing program was created. This works by analytically determining the intersection of the rays with the cone wall. A similar method is described by Rinker and Bohannon [121], however in the code created the intersections and reflections of the rays are calculated in a 3D geometry. The reflectivity and absorption were modelled in the same way as by Woerkom *et al.* [95], having 35% reflectivity for all angles at 55° to the surface normal or less, and a linear increase to 100% reflectivity at glancing angles. Full details of how the code works and the source code are given in appendix B.

The filling of pre-plasma in the cone was not taken into account, but could have a significant effect on the way the laser light is absorbed and reflected, especially close to the cone tip. For example, in a similar experimental set up by Baton *et al.*, at an intensity of 10^{19} W cm^{-2} with a contrast ratio of 10^{-7}, a 100 µm plasma was seen extending from a cone-like target [122]. During the nanosecond laser pre-pulse the intensity is high enough to produce some pre-plasma, even in the defocused case. This effect will be strongest for the tightly

focused cases, close to the cone tip, where the absorption and reflection of the laser pulse will be moved out from the cone tip. Phase effects were also not taken into account in the ray tracing code. These can create local hotspots along the wall of the cone [123], which could potentially alter the physics, but the ray tracing code will still give accurate mean intensities on longer scale lengths. Similarly, far-field effects when defocusing the laser will mean the laser profile does not have a pure Gaussian profile, but again this effect will be less significant on longer scale lengths.

Figure 4.19 shows the results from the ray tracing code. For the case where the laser is focused tightly to the cone tip the ray tracing code reproduces a Gaussian with a FWHM of 8 µm and a peak of $\sim 10^{21}$ W cm^{-2}, as expected from the input. When the laser is focused at -275 µm, that is before the cone tip, the peak intensity falls to 0.3×10^{21} W cm^{-2}. Similarly with the focus at +275 µm, beyond the cone tip, the intensity drops even more, to approximately 0.2×10^{21} W cm^{-2}. At $\pm$800 µm the intensity drops to 0.1×10^{20} W cm^{-2}. The intensity along the cone wall for the defocused cases was found to be $\sim 10^{18} - 10^{19}$ W cm^{-2}, many orders of magnitude higher than for the tight focus case where the intensity along the wall is $< 10^{16}$ W cm^{-2}.

If the reflections in the code are turned off, then for the $\pm$275 µm defocus cases the intensity at the cone tip is reduced by a factor of $\sim$100. This suggests the cone is acting as an efficient light guide for the laser energy, by reflecting the beam from the cone walls onto the cone tip. Some small perturbations from the general trend of decreasing intensity with distance from the cone tip can be seen in figure 4.19. These perturbations are caused by reflections from the flat cone tip.

The overall reduction in intensity is consistent with the data presented for the change in electron scale length in the wire, figures 4.15 and 4.18, if the hot electron scaling is between $(I\lambda^2)^{0.3}$ and $(I\lambda^2)^{0.5}$, as discussed in section 1.5.2.

4.4 Summary

The results for the total copper K_α yield shown in figure 4.12, along with the results from the FIDO simulations shown in figures 4.13 and 4.16, indicate that

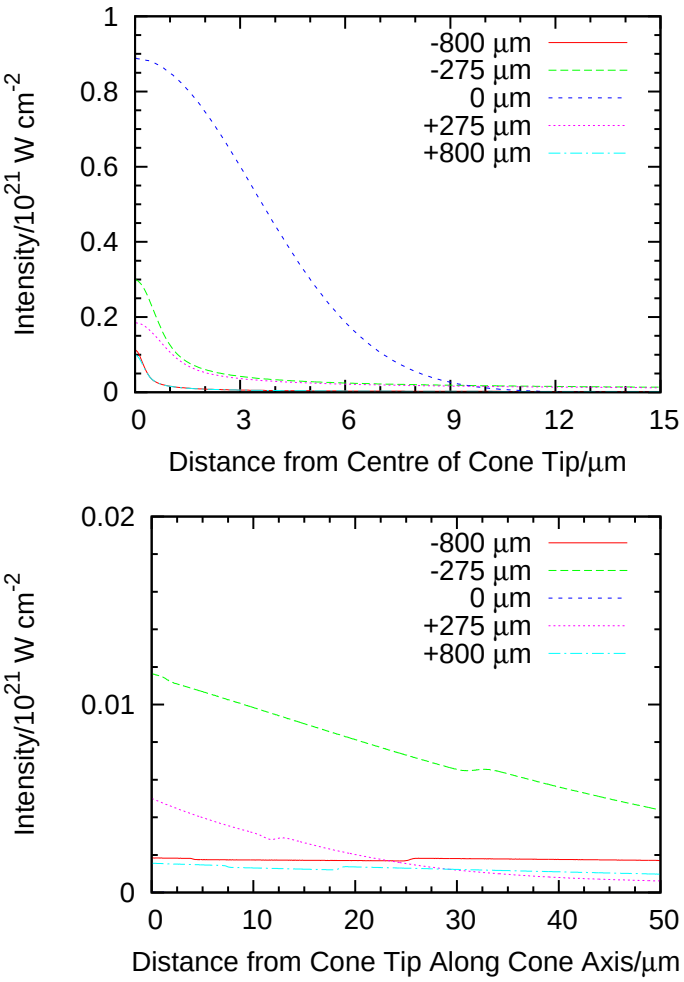

Figure 4.19: Top: laser intensity across the cone tip from the ray tracing code for five different defocus positions. Bottom: intensity along the cone wall for the same defocus positions.

the energy coupling is maintained when defocusing the laser. In the defocused cases there does not appear to be a drop off in the total copper K_α photon yield measured, despite the FIDO simulation results showing that at lower electron temperatures there is a lower total copper K_α yield for a given total fast electron energy. The data presented in figure 4.15 from the copper K_α imager shows that the electron spectrum is softened, which is supported by the results from the electron spectrometer in figure 4.18. The softening of the electron spectrum is in agreement with the results from ray tracing code, as shown in figure 4.19.

It is expected that the reduced pre-pulse intensities result in a substantial reduction in pre-plasma formation at the cone tip. Therefore, although the laser intensity at the tip is lower, more energy reaches the wire since the point of laser absorption is now moved closer to the cone tip. For the tight focus case it is expected that the pre-plasma will increase the total laser energy absorption in the target [124], but fewer of the hot electrons in this case will enter the copper wire. An ability to have some control of the electron spectrum, without a large drop in laser-energy coupling, could be useful in fast ignition by virtue of permitting the creation of a more compact hotspot.

Care must be taken in extrapolating these results to a full scale cone guided fast ignition scheme. Although there are a number of technologies that are presently being explored to increase laser contrast, the substantially higher laser energy that would be employed in fast ignition fusion experiments might well still have a higher level of pre-pulse associated with it than that which was used here. While it could be anticipated that the electron spectrum may be softened in this case, the integrity of the cone surface may be compromised sooner in the case of a higher energy pre-pulse, resulting in a reduction in coupling. Furthermore, the main pulse in a full scale fast ignition scheme would be around 20 ps. It is not clear how long into the laser pulse the light guiding effect of the cone may last, as in the experiment described in this chapter pulse lengths were only around a picosecond.

Chapter 5

Summary and Conclusions

5.1 Overview

In this thesis work has been presented which gives consideration to the generation and transport of fast electrons in fast ignition relevant plasmas. In chapter 1 an overview of both inertial confinement fusion and fast ignition fusion was given, explaining the physical considerations that lead to the basic fuel assemblies required. One of the aspects that is not well understood in fast ignition, but is of critical importance, is the generation and transport of the electrons needed to heat the hotspot. The work in this thesis has looked at two main themes, the first being the transport of the electrons through the plasma. The response of the background plasma was found by a consideration of the magnetohydrodynamic equations. In the second part experimental results were presented for the generation of electrons in a gold cone, and the effect of defocusing the laser on the energy coupling and spectrum of the fast electrons was established.

5.2 Cavitation and Shockwave Generation in Fast Ignition Relevant Plasmas

In chapter 2 the magnetohydrodynamic equations were introduced as a simplified way of understanding the macroscopic behaviour of a plasma. The

basic equations of ideal MHD were shown to follow from the Vlasov equation, while in plasmas of interest to fast ignition it was seen that collisions were important, as given by the Vlasov-Fokker-Planck equation. The numerical approach to solving the MHD equations was explored, including some aspects of the terms in non-ideal MHD.

In chapter 3 the MHD equations were used to understand the physics that occurs when a plasma is subjected to a fast electron beam. While such an analytic model has limitations, it is a very useful tool in understanding how significant cavitation can be in a fast ignition relevant plasma. The Ohmic heating from the resistive return current was demonstrated to be the dominant method by which cavitation occurs in the plasma, meaning the $J_p \times B$ force can be neglected for basic approximations. Using this analytic model it was seen that the important parameter, that determines the amount of cavitation in the plasma, is the current density squared divided by the mass density. This is effectively due to the amount of energy going into the plasma from Ohmic heating, and the heat capacity in the plasma.

The results from the analytic model were verified and compared to the results from a numerical MHD code. In order to study this problem the extra terms required in the MHD equations were established, and added into a code based on a method by Ziegler. The Ohmic heating was seen to increase the temperature in the plasma rapidly at early times, such that a further restriction of the time step was required. This MHD code helped to establish that some of the assumptions made in the derivation of the analytic model were indeed reasonable for much of the parameter space considered. In cases where more extreme cavitation was expected to occur the numerical code was required to determine the precise form of shocks in the plasma. The analytic model was useful for an approximate understanding of the parameter space where shocks would occur, and on what timescales.

There is further work to be done in this area, especially with proposals to use more advanced targets, such as ones with a structured collimator. In this case 2D hydrodynamic modelling is required, and including a consideration of the magnetic fields would be preferable. Effects such as thermal conductivity and ion-electron equilibration are important, and provide a more accurate picture of

the physics that will occur, especially when considering the magnitude of the heating, and the resulting pressure gradients, in fast ignition plasmas. More care must be taken in 2D to ensure the stability of the code.

5.3 Effect of Defocusing on Laser-Coupling into Gold Cones

In chapter 4 an experiment was described which looked at the coupling of laser energy into hot electrons in a gold cone, while defocusing the laser. This was motivated by a previous result where defocusing the laser apparently caused an enhancement in the radiation dose, as seen by a thermoluminescent dosimeter, in such a case.

The results from this experiment did not appear to show any drop in the copper K_α radiation yield when the laser was defocused. It was established from simulations performed with a Vlasov-Fokker-Planck code that at lower laser intensities the copper K_α yield would be expected to decrease, for a given energy in the hot electrons. This shows that the coupling of laser energy into hot electrons is maintained, even when the laser is defocused. The ray tracing code that was developed established a definite idea of the intensities when defocusing by different amounts, demonstrating the importance of the cone acting as a light guide and reflecting the laser energy towards the cone tip. Wilks scaling was used to establish the temperature of the hot electrons used in the Vlasov-Fokker Planck code, for a given defocus distance, from the intensities determined by the ray tracing code.

While the overall coupling energy of the laser into hot electrons was maintained, the electron spectrum was softened. This was established in the data from the copper K_α imager, and backed up by the results from the electron spectrometer. This softening of the electron spectrum was consistent with previous scaling laws of fast electron temperature with intensity, with the intensity established from the ray tracing code. The scale lengths found in the experiment were also consistent with the results from the Vlasov-Fokker-Planck simulations.

This result was understood on the basis of the reduced pre-pulse intensity leading to a reduced pre-plasma at the cone tip. This allows laser energy to be absorbed much closer to the cone tip, and, despite the fact that the intensity is lower, this will allow more of the electrons to enter the copper wire.

5.4 Conclusions

The work looking at the response of a plasma to a fast electron beam highlights an area that consideration must be given to in fast ignition schemes. If the target is blown apart by the resistive return current, before sufficient heating of the hotspot, then the areal density criterion would not be met and ignition would not occur. Consideration of this hydrodynamic response is needed, especially if more advanced cone-target designs are used, where the current is confined to an even narrower region.

The result from the experimental work is potentially useful in fast ignition, as it allows some control of the fast electron temperature, without any significant drop in the energy in the fast electrons. Some care must be taken in extrapolating the results to a full cone guided fast ignition scheme, where the pulse length is up to 20 times longer, as the light guiding effect may not continue for this duration.

Appendix A

Fluid Codes

A.1 One Dimensional MHD Code Including a Resistive Return Current

This code was written in Fortran 90 and complied with the GNU Fortran Compiler. The setup shown here is for the results discussed in chapter 3, specifically those shown in figure 3.7. The time taken to perform this run was 1.6 s, with 2000 cells and 93 time steps, on a single core of an Intel Core 2 Duo processor. Note that this code is run with the compiler flag `-fdefault-real-8` when compiling with the GNU Fortran Compiler, to ensure double precision floating point numbers are used.

```
program ziegler_return
implicit none

  ! USEFUL CONSTANTS

  real, parameter :: mu = 1.256637061e-6   ! mu = 4.0 * pi / 1.0e-7
  real, parameter :: qe = 1.602176487e-19  ! elementary charge
  real, parameter :: mp = 1.672621637e-27  ! proton mass
  real, parameter :: kB = 1.3806504e-23    ! Boltzmann's constant
  real, parameter :: spitzer = 1.0e-4      ! for Spitzer-Harm resistivity

  ! CHOICE OF PLASMA SETUP

  real, parameter :: gamma = 5.0/3.0  ! adiabatic index
  real, parameter :: Z = 1.0          ! atomic charge
  real, parameter :: lnLambda = 10.0  ! Coulomb logarithm
  real, parameter :: j0 = 1.0e16      ! peak current density
  real, parameter :: rbeam = 3.0e-6   ! fast electron beam width
```

```
  real, parameter :: T_init = 100.0   ! initial temperature in eV
20
  ! EULERIAN GRID SETUP

  integer, parameter :: n_cells = 2000
  real, parameter :: x_min = -25.0e-6, x_max = 25.0e-6
  real :: dx
  integer :: n ! to be used for counting cell number

  ! TIME STEPS

30 real :: t = 0.0                      ! current time
  real :: dt                            ! time step size
  real :: dt_ohmic                      ! max time step due to Ohmic heating
  real, parameter :: t_max = 3.0e-12    ! end time
  integer :: n_steps = 0                ! counter for number of time steps

  real, parameter :: dt_output = 0.1e-12  ! interval to output data
  integer :: n_outputs                    ! counter for number of outputs

  ! ARRAYS FOR FLUID VARIABLES
40
  ! subscripts _e, _w are East and West values (see paper)
  ! subcripts _s are u* fluid values for Runge-Kutta scheme

  ! density
  real, dimension(:), allocatable :: rho, rho_e, rho_w, &
                                     & rho_s, rho_s_e, rho_s_w
  ! energy
  real, dimension(:), allocatable :: e, e_e, e_w, &
                                     & e_s, e_s_e, e_s_w
50 ! momenutm (x-direction)
  real, dimension(:), allocatable :: mx, mx_e, mx_w, &
                                     & mx_s, mx_s_e, mx_s_w
  ! magnetic field (z-direction)
  real, dimension(:), allocatable :: Bz, Bz_e, Bz_w, &
                                     & Bz_s, Bz_s_e, Bz_s_w
  ! hot electron current (y-direction)
  real, dimension(:), allocatable :: Jy

  ! ARRAYS FOR DERIVED VALUES
60
  ! pressure
  real, dimension(:), allocatable :: p, p_e, p_w, &
                                     & p_s, p_s_e, p_s_w
  ! velocity (x-direction)
  real, dimension(:), allocatable :: vx, vx_e, vx_w
  ! magnetosonic speed (x-direction)
  real, dimension(:), allocatable :: cf_e, cf_w, cf
  ! resistivity
  real, dimension(:), allocatable :: eta, &
70                                   & eta_s

  ! FOR ZIEGLER SCHEME

  real :: u_e, u_w, f_e, f_w
  real :: u_e_m, u_w_m, f_e_m, f_w_m

  ! allocate arrays

  ! note that cells 0, n_cells+1 are ghost cells used for boundary conditions
80
```

```
  allocate(rho(0:n_cells+1), rho_e(0:n_cells+1), rho_w(0:n_cells+1), &
        & rho_s(0:n_cells+1), rho_s_e(0:n_cells+1), rho_s_w(0:n_cells+1))
  allocate(e(0:n_cells+1), e_e(0:n_cells+1), e_w(0:n_cells+1), &
       & e_s(0:n_cells+1), e_s_e(0:n_cells+1), e_s_w(0:n_cells+1))
  allocate(mx(0:n_cells+1), mx_e(0:n_cells+1), mx_w(0:n_cells+1), &
        & mx_s(0:n_cells+1), mx_s_e(0:n_cells+1), mx_s_w(0:n_cells+1))
  allocate(Bz(0:n_cells+1), Bz_e(0:n_cells+1), Bz_w(0:n_cells+1), &
        & Bz_s(0:n_cells+1), Bz_s_e(0:n_cells+1), Bz_s_w(0:n_cells+1))
  allocate(Jy(0:n_cells+1))

  allocate(p(0:n_cells+1), p_e(0:n_cells+1), p_w(0:n_cells+1), &
        & p_s(0:n_cells+1), p_s_e(0:n_cells+1), p_s_w(0:n_cells+1))
  allocate(vx(0:n_cells+1), vx_e(0:n_cells+1), vx_w(0:n_cells+1))
  allocate(cf_e(0:n_cells+1), cf_w(0:n_cells+1), cf(0:n_cells+1))
  allocate(eta(0:n_cells+1), &
        & eta_s(0:n_cells+1))

  ! initial setup

  dx = (x_max - x_min)/real(n_cells)  ! grid spacing

  rho(0:n_cells+1) = 100.0  ! initial density, uniform

  do n = 0, n_cells+1
    e(n) = T_init * qe * rho(n) / (mp * (gamma - 1.0)) ! internal energy
  end do

  mx = 0.0  ! initially stationary
  Bz = 0.0  ! no initial magnetic field

  call calculate_p    ! calculates pressure, in array p
  call calculate_eta  ! calculates resistivity, in array eta

  do n = 0, n_cells+1  ! Gaussian current density initialisation
    Jy(n) = j0*exp(-(dx*real(n)-dx*real(n_cells/2))**2/(2.0*rbeam**2))
  end do

  call output_all  ! write out starting values
  n_outputs = 1

  print*, 'Starting Ziegler scheme...'

  do while (t .lt. t_max)

    ! calculate East and West cell wall values

    call calculate_east_west(rho, rho_e, rho_w)
    call calculate_east_west(e, e_e, e_w)
    call calculate_east_west(mx, mx_e, mx_w)
    call calculate_east_west(Bz, Bz_e, Bz_w)

    ! update useful quantities, calcuale East and West cell wall values

    call calculate_p
    call calculate_east_west(p, p_e, p_w)

    call calculate_vx
    call calculate_east_west(vx, vx_e, vx_w)

    call calculate_cf
    call calculate_east_west(cf, cf_e, cf_w)
```

```
    call calculate_eta

    call calculate_dt_ohmic  ! calculate maximum time step from Ohmic heating
    ! choose maximum time step, either CFL condition or dt_ohmic
    dt = 0.7 * min(dx / (maxval(abs(vx))+maxval(abs(cf))), dt_ohmic)

    do n = 1, n_cells
150
      ! Ziegler scheme, calculate u* values

      ! density
      u_e = rho_e(n)
      u_w = rho_w(n+1)
      f_e = mx_e(n)
      f_w = mx_w(n+1)
      u_e_m = rho_e(n-1)
      u_w_m = rho_w(n)
160   f_e_m = mx_e(n-1)
      f_w_m = mx_w(n)

      rho_s(n) = rho(n) + dt * &
               & ziegler_flux(u_e, u_w, f_e, f_w, u_e_m, u_w_m, f_e_m, f_w_m)

      ! energy
      u_e = e_e(n)
      u_w = e_w(n+1)
      f_e = (e_e(n) + p_e(n) + &
170       &  Bz_e(n)**2 / (2.0 * mu)) * mx_e(n) / rho_e(n)
      f_w = (e_w(n+1) + p_w(n+1) + &
          &  Bz_w(n+1)**2 / (2.0 * mu)) * mx_w(n+1) / rho_w(n+1)
      u_e_m = e_e(n-1)
      u_w_m = e_w(n)
      f_e_m = (e_e(n-1) + p_e(n-1) + &
            &  Bz_e(n-1)**2 / (2.0 * mu)) * mx_e(n-1) / rho_e(n-1)
      f_w_m = (e_w(n) + p_w(n) + &
            &  Bz_w(n)**2 / (2.0 * mu)) * mx_w(n) / rho_w(n)

180   e_s(n) = e(n) + dt * &
             & (ziegler_flux(u_e, u_w, f_e, f_w, u_e_m, u_w_m, f_e_m, f_w_m) &
             & + eta(n) * Jy(n)**2 - &
             & (Bz(n) / mu) * (eta(n+1) * Jy(n+1) - eta(n-1) * Jy(n-1)) / &
             & (2.0 * dx) + Jy(n) * Bz(n) * mx(n) / rho(n))
             ! additional terms to account for energy from Ohmic heating and
             ! resistive magnetic field generation

      ! momentum (x-direction)
      u_e = mx_e(n)
190   u_w = mx_w(n+1)
      f_e = mx_e(n)**2 / rho_e(n) + p_e(n) + &
          & Bz_e(n)**2 / (2.0 * mu)
      f_w = mx_w(n+1)**2 / rho_w(n+1) + p_w(n+1) + &
          & Bz_w(n+1)**2 / (2.0 * mu)
      u_e_m = mx_e(n-1)
      u_w_m = mx_w(n)
      f_e_m = mx_e(n-1)**2 / rho_e(n-1) + p_e(n-1) + &
            & Bz_e(n-1)**2 / (2.0 * mu)
      f_w_m = mx_w(n)**2 / rho_w(n) + p_w(n) + &
200   &       Bz_w(n)**2 / (2.0 * mu)

      mx_s(n) = mx(n) + dt * &
              & (ziegler_flux(u_e, u_w, f_e, f_w, u_e_m, u_w_m, f_e_m, f_w_m) &
              & + Jy(n) * Bz(n))
```

```
    end do

    ! enforce open boundary conditions
    rho_s(0) = rho_s(1)
    rho_s(n_cells+1) = rho_s(n_cells)
    e_s(0) = e_s(1)
    e_s(n_cells+1) = e_s(n_cells)
    mx_s(0) = mx_s(1)
    mx_s(n_cells+1) = mx_s(n_cells)

    do n = 1, n_cells

      ! magnetic field (z-direction)
      u_e = Bz_e(n)
      u_w = Bz_w(n+1)
      f_e = (mx_e(n) / rho_e(n)) * Bz_e(n)
      f_w = (mx_w(n+1) / rho_w(n+1)) * Bz_w(n+1)
      u_e_m = Bz_e(n-1)
      u_w_m = Bz_w(n)
      f_e_m = (mx_e(n-1) / rho_e(n-1)) * Bz_e(n-1)
      f_w_m = (mx_w(n) / rho_w(n)) * Bz_w(n)

      Bz_s(n) = Bz(n) + dt * &
            & (ziegler_flux(u_e, u_w, f_e, f_w, u_e_m, u_w_m, f_e_m, f_w_m) &
            & - (eta(n+1) * Jy(n+1) - eta(n-1) * Jy(n-1)) / (2.0 * dx))

    end do

    ! enforce open boundary conditions
    Bz_s(0) = Bz_s(1)
    Bz_s(n_cells+1) = Bz_s(n_cells)

    ! now calculate East and West cell wall values for u*

    call calculate_east_west(rho_s, rho_s_e, rho_s_w)
    call calculate_east_west(e_s, e_s_e, e_s_w)
    call calculate_east_west(mx_s, mx_s_e, mx_s_w)
    call calculate_east_west(Bz_s, Bz_s_e, Bz_s_w)

    ! update useful quantities, calcuale East and West cell wall values for u*

    call calculate_vx_s
    call calculate_east_west(vx, vx_e, vx_w)

    call calculate_p_s
    call calculate_east_west(p_s, p_s_e, p_s_w)

    call calculate_cf_s
    call calculate_east_west(cf, cf_e, cf_w)

    call calculate_eta_s

    do n = 1, n_cells

      ! Ziegler scheme, calculate u^(n+1) values

      ! density
      u_e = rho_s_e(n)
      u_w = rho_s_w(n+1)
      f_e = mx_s_e(n)
      f_w = mx_s_w(n+1)
```

```
      u_e_m = rho_s_e(n-1)
      u_w_m = rho_s_w(n)
      f_e_m = mx_s_e(n-1)
      f_w_m = mx_s_w(n)

      rho(n) = 0.5 * rho(n) + 0.5 * (rho_s(n) + dt * &
             & ziegler_flux(u_e, u_w, f_e, f_w, u_e_m, u_w_m, f_e_m, f_w_m))

      ! energy
      u_e = e_s_e(n)
      u_w = e_s_w(n+1)
      f_e = (e_s_e(n) + p_s_e(n) + &
          &  Bz_s_e(n)**2 / (2.0 * mu)) * mx_s_e(n) / rho_s_e(n)
      f_w = (e_s_w(n+1) + p_s_w(n+1) + &
          &  Bz_s_w(n+1)**2 / (2.0 * mu)) * mx_s_w(n+1) / rho_s_w(n+1)
      u_e_m = e_s_e(n-1)
      u_w_m = e_s_w(n)
      f_e_m = (e_s_e(n-1) + p_s_e(n-1) + &
            &  Bz_s_e(n-1)**2 / (2.0 * mu)) * mx_s_e(n-1) / rho_s_e(n-1)
      f_w_m = (e_s_w(n) + p_s_w(n) + &
            &  Bz_s_w(n)**2 / (2.0 * mu)) * mx_s_w(n) / rho_s_w(n)

      e(n) = 0.5 * e(n) + 0.5 * (e_s(n) + dt * &
         & (ziegler_flux(u_e, u_w, f_e, f_w, u_e_m, u_w_m, f_e_m, f_w_m) &
         & + eta_s(n) * Jy(n)**2 - &
         & (Bz_s(n) / mu) * (eta_s(n+1) * Jy(n+1) - eta_s(n-1) * Jy(n-1)) &
         & / (2.0 * dx) + Jy(n) * Bz_s(n) * mx_s(n) / rho_s(n)))

      ! momentum(x)
      u_e = mx_s_e(n)
      u_w = mx_s_w(n+1)
      f_e = mx_s_e(n)**2 / rho_s_e(n) + p_s_e(n) + &
          & Bz_s_e(n)**2 / (2.0 * mu)
      f_w = mx_s_w(n+1)**2 / rho_s_w(n+1) + p_s_w(n+1) &
          & + Bz_s_w(n+1)**2 / (2.0 * mu)
      u_e_m = mx_s_e(n-1)
      u_w_m = mx_s_w(n)
      f_e_m = mx_s_e(n-1)**2 / rho_s_e(n-1) + p_s_e(n-1) + &
            & Bz_s_e(n-1)**2 / (2.0 * mu)
      f_w_m = mx_s_w(n)**2 / rho_s_w(n) + p_s_w(n) + &
            & Bz_s_w(n)**2 / (2.0 * mu)

      mx(n) = 0.5 * mx(n) + 0.5 * (mx_s(n) + dt * &
             & (ziegler_flux(u_e, u_w, f_e, f_w, u_e_m, u_w_m, f_e_m, f_w_m) &
             &  + Jy(n) * Bz_s(n)))

    end do

    ! enforce open boundary conditions
    rho(0) = rho(1)
    rho(n_cells+1) = rho(n_cells)
    e(0) = e(1)
    e(n_cells+1) = e(n_cells)
    mx(0) = mx(1)
    mx(n_cells+1) = mx(n_cells)

    do n = 1, n_cells

      ! magnetic field (z-direction)
      u_e = Bz_s_e(n)
      u_w = Bz_s_w(n+1)
      f_e = (mx_s_e(n) / rho_s_e(n)) * Bz_s_e(n)
```

```
      f_w = (mx_s_w(n+1) / rho_s_w(n+1)) * Bz_s_w(n+1)
      u_e_m = Bz_s_e(n-1)
      u_w_m = Bz_s_w(n)
      f_e_m = (mx_s_e(n-1) / rho_s_e(n-1)) * Bz_s_e(n-1)
      f_w_m = (mx_s_w(n) / rho_s_w(n)) * Bz_s_w(n)

      Bz(n) = 0.5 * Bz(n) + 0.5 * (Bz_s(n) + dt * &
            & (ziegler_flux(u_e, u_w, f_e, f_w, u_e_m, u_w_m, f_e_m, f_w_m) &
            & - (eta_s(n+1) * Jy(n+1) - eta_s(n-1) * Jy(n-1)) / (2.0 * dx)))

    end do

    ! enforce open boundary conditions
    Bz(0) = Bz(1)
    Bz(n_cells+1) = Bz(n_cells)

    call calculate_p

    if(floor(t / (dt_output * real(n_outputs))) .gt. 0) then
      call output_all
      n_outputs = n_outputs + 1
    end if

    t = t + dt              ! increment time step
    n_steps = n_steps + 1   ! increment time steps counter

    print*, 'time =', t, 'step size =', dt

  end do

  call output_all

  call calculate_vx
  print*, '... finished!'
  print*, 'Number of time steps taken =', n_steps

contains

subroutine calculate_p  ! calculates pressure and returns array of values

  integer :: n2

  do n2 = 0, n_cells+1
    p(n2) = (gamma - 1.0) * (e(n2) - &
          & 0.5 * mx(n2)**2 / rho(n2) - Bz(n2)**2 / (2.0 * mu))
  end do

end subroutine calculate_p

subroutine calculate_p_s  ! as calculate_p, for p*

  integer :: n2

  do n2 = 0, n_cells+1
    p_s(n2) = (gamma - 1.0) * (e_s(n2) - &
            & 0.5 * mx_s(n2)**2 / rho_s(n2) - Bz_s(n2)**2 / (2.0 * mu))
  end do

end subroutine calculate_p_s

subroutine calculate_vx  ! calculates velocity (x-direction) and returns array
                         ! of values
```

```
  integer :: n2

  do n2 = 0, n_cells+1
    vx(n2) = mx(n2)/rho(n2)
  end do

end subroutine calculate_vx

subroutine calculate_vx_s  ! as calculate_vx, for vx*

  integer :: n2

  do n2 = 0, n_cells+1
    vx(n2) = mx_s(n2)/rho_s(n2)
  end do

end subroutine calculate_vx_s

subroutine calculate_cf ! calculates magnetosonic speed and returns array of
                        ! values
  integer :: n2

  do n2 = 0, n_cells+1
    cf(n2) = sqrt(gamma * p(n2) / rho(n2) + Bz(n2)**2 / (mu * rho(n2)))
  end do

end subroutine calculate_cf

subroutine calculate_cf_s  ! as calculate_cf, for cf*

  integer :: n2

  do n2 = 0, n_cells+1
    cf(n2) = sqrt(gamma * p_s(n2) / rho_s(n2) + Bz_s(n2)**2 / &
                                                & (mu * rho_s_w(n2)))
  end do

end subroutine calculate_cf_s

subroutine calculate_eta  ! calculates resistivity and returns
                          ! array of values
  integer :: n2

  real :: temperature

  do n2 = 0, n_cells+1
    temperature = p(n2) * mp / (rho(n2) * qe)
    eta(n2) = spitzer * Z * lnLambda / (sqrt(temperature))**3
  end do

end subroutine calculate_eta

subroutine calculate_eta_s  ! as calculate_eta, for eta*

  integer :: n2

  real :: temperature

  do n2 = 0, n_cells+1
    temperature = p_s(n2) * mp / (rho_s(n2) * qe)
    eta_s(n2) = spitzer * Z * lnLambda / (sqrt(temperature))**3
  end do
```

```
end subroutine calculate_eta_s

subroutine calculate_dt_ohmic  ! calculate temperautre doubling time due to
                               ! Ohimc heating
  real :: T_max
  real :: t2
  real :: alpha

  alpha = (qe / kB)**(3.0/2.0) * (5.0 / 2.0) * ((spitzer * Z * lnLambda * &
                          & (gamma - 1.0) * j0**2 * mp) / (kB * maxval(rho)))

  T_max = (maxval(p) / minval(rho)) * (mp / kB)

  t2 = (2.0**(2.0/5.0) - 1.0) * T_max**(5.0/2.0) / alpha

  dt_ohmic = t2 ! could make dt_ohmic a smaller or larger fraction of
                ! temperature doubling time, but equal verified as being good

end subroutine calculate_dt_ohmic

function ziegler_flux(u_ed, u_wd, f_ed, f_wd, u_e_md, u_w_md, f_e_md, f_w_md)

  ! Ziegler flux calculation

  real :: ziegler_flux
  real, intent(in) :: u_ed, u_wd, f_ed, f_wd
  real, intent(in) :: u_e_md, u_w_md, f_e_md, f_w_md

  real :: F_p, F_m
  real :: a_p, a_m

  a_p = max(vx_w(n+1) + cf_w(n+1), vx_e(n) + cf_e(n), 0.0)
  a_m = min(vx_w(n+1) - cf_w(n+1), vx_e(n) - cf_e(n), 0.0)
  F_p = (a_p * f_ed - a_m * f_wd + a_p * a_m * (u_wd - u_ed)) / (a_p - a_m)

  a_p = max(vx_w(n) + cf_w(n), vx_e(n-1) + cf_e(n-1), 0.0)
  a_m = min(vx_w(n) - cf_w(n), vx_e(n-1) - cf_e(n-1), 0.0)

  F_m = (a_p * f_e_md - a_m * f_w_md + a_p * a_m * (u_w_md - u_e_md)) / &
                                                          & (a_p - a_m)

  ziegler_flux = - (F_p - F_m) / dx

end function ziegler_flux

subroutine calculate_east_west(ud, u_ed, u_wd)

  ! interpolation onto cell walls

  real, intent(in) :: ud(0:n_cells+1)
  real, intent(out) :: u_ed(0:n_cells+1), u_wd(0:n_cells+1)
  real :: delta, s

  integer :: n2

  do n2 = 1, n_cells
    if ((ud(n2+1) - ud(n2)) * (ud(n2) - ud(n2-1)) .gt. 0.0) then
      delta = (ud(n2+1) - ud(n2)) * (ud(n2) - ud(n2-1)) / &
                                                & (ud(n2+1) - ud(n2-1))
      s = sign(1.0, ud(n2+1)-ud(n2))
    else
```

```
      delta = 0.0
      s = 0.0
    end if

    u_ed(n2) = ud(n2) + delta
    u_wd(n2) = ud(n2) - delta

  end do

  u_ed(0) = u_ed(1)
  u_wd(0) = u_wd(1)
  u_ed(n_cells+1) = u_ed(n_cells)
  u_wd(n_cells+1) = u_wd(n_cells)

end subroutine calculate_east_west

subroutine output_all

  ! output main fluid variables of interest
  call output_density
  call output_pressure
  call output_Bz
  call output_velocity_x

  ! output to compare strength of J x B force and pressure gradient
  call output_BzJy
  call output_dpdx

end subroutine output_all

subroutine output_density

  character(29) :: fname
  integer :: output_number ! this is the output time in femtoseconds

  write(fname,'(A29)') 'output/density/rho_xxxxxx.txt'
  output_number = floor(t / 1.0e-15) + 1000000
  write(fname(19:25),'(I7)') output_number
  write(fname(19:19),'(A1)') '_'
  open(500, file=fname)

  do n = 1, n_cells
    write(500,*) x_min + (real(n) - 0.5) * dx, rho(n)
  end do

  close(500)

end subroutine output_density

subroutine output_pressure

  character(28) :: fname
  integer :: output_number ! this is the output time in femtoseconds

  write(fname,'(A28)') 'output/pressure/p_xxxxxx.txt'
  output_number = floor(t / 1.0e-15) + 1000000
  write(fname(18:24),'(I7)') output_number
  write(fname(18:18),'(A1)') '_'
  open(500, file=fname)

  do n = 1, n_cells
    write(500,*) x_min + (real(n) - 0.5) * dx, p(n)
```

```
  end do

  close(500)

end subroutine output_pressure

subroutine output_Bz

  character(23) :: fname
  integer :: output_number ! this is the output time in femtoseconds

  write(fname,'(A23)') 'output/Bz/Bz_xxxxxx.txt'
  output_number = floor(t / 1.0e-15) + 1000000
  write(fname(13:19),'(I7)') output_number
  write(fname(13:13),'(A1)') '_'
  open(500, file=fname)

  do n = 1, n_cells
    write(500,*) x_min + (real(n) - 0.5) * dx, Bz(n)
  end do

  close(500)

end subroutine output_Bz

subroutine output_velocity_x

  character(23) :: fname
  integer :: output_number ! this is the output time in femtoseconds

  write(fname,'(A23)') 'output/vx/vx_xxxxxx.txt'
  output_number = floor(t / 1.0e-15) + 1000000
  write(fname(13:19),'(I7)') output_number
  write(fname(13:13),'(A1)') '_'
  open(500, file=fname)

  call calculate_vx

  do n = 1, n_cells
    write(500,*) x_min + (real(n) - 0.5) * dx, vx(n)
  end do

  close(500)

end subroutine output_velocity_x

subroutine output_BzJy

  character(27) :: fname
  integer :: output_number ! this is the output time in femtoseconds

  write(fname,'(A27)') 'output/BzJy/BzJy_xxxxxx.txt'
  output_number = floor(t / 1.0e-15) + 1000000
  write(fname(17:23),'(I7)') output_number
  write(fname(17:17),'(A1)') '_'
  open(500, file=fname)

  do n = 1, n_cells
    write(500,*) x_min + (real(n) - 0.5) * dx, Bz(n) * Jy(n)
  end do

  close(500)
```

```
640 end subroutine output_BzJy

    subroutine output_dpdx

      character(27) :: fname
      integer :: output_number ! this is the output time in femtoseconds

      write(fname,'(A27)') 'output/dpdx/dpdx_xxxxxx.txt'
      output_number = floor(t / 1.0e-15) + 1000000
      write(fname(17:23),'(I7)') output_number
650   write(fname(17:17),'(A1)') '_'
      open(500, file=fname)

      do n = 1, n_cells
        write(500,*) x_min + (real(n) - 0.5) * dx, (p(n+1) - p(n-1))/(2.0*dx)
      end do

      close(500)

    end subroutine output_dpdx
660
    end program ziegler_return
```

A.2 Two Dimensional, Two Fluid Hydrocode

The code described in section 3.5 was also written in Fortran 90 and tested with the GNU Fortran Compiler. The setup shown in figures 3.12 and 3.13 took 5 hours to run, with 200 × 100 cells and 30,000 time steps, on a single core of an Intel Core 2 Duo processor. Note that this code is also run with the compiler flag `-fdefault-real-8` when compiling with the GNU Fortran Compiler, such that double precision floating point numbers are used.

The code is split into a number of modules, only the modules to calculate the thermal conductivity and ion-electron equilibration are included here. Broadly speaking the code is similar to that shown in section A.1 of this appendix.

A.2.1 Thermal Conductivity

Here the module `global_variables` contains the variables that need to be accessed by most modules, such as the values of the fluid variables, and `fluid_calculations` contains functions to calculate quantities such as the pressure. The names of variables should be clear when comparing with the description of the numerical approach given in section 2.5.5. The Thomas algorithm is implemented from the *Numerical Recipes for Fortran 90* [76] function

`tridiag_ser`, which is included in the module `numerical_routines`, and also relies on the modules `nrtype` and `nrutillite` from the same book.

Note the thermal conduction is applied to the electron temperatures only, which are the dominate mechanism for the thermal conductivity. The ion-electron equilibration will transfer some of the energy that has been transported back to the ions. The thermal conduction is applied first in the x-direction, and then in the y-direction.

```
module thermal_conduction

use global_variables
use fluid_calculations

implicit none

contains

function kappaSH(nx,ny)  ! calculate the Spitzer-Harm thermal conductivity
                         ! for cell (nx, ny)
  real :: kappaSH
  real :: eps  ! eps is the correction factor due to atomic number Z

  integer, intent(in) :: nx, ny  ! cell number counters

  ! eps as given by Brueckner and Jorna, Rev. Mod. Phys. 1974
  eps = 0.472 * Z / (Z + 4.0)

  kappaSH = eps * (640.0 * sqrt(2.0*pi3) * kB**(7.0/2.0) * &
          & (pe(nx,ny) / (ne(nx,ny) * kB))**(5.0/2.0) * eps0**2) / &
          & (sqrt(me) * qe**4 * Z * coullog)

end function kappaSH

subroutine spitzer_harm_x  ! see thesis for a fuller explanation of scheme

  use numerical_routines

  ! VECTORS FOR MATRIX SOLVE

  ! Mb - vector for diagonal elemets of matrix
  ! Vd - vector for temperature at time n
  ! Vdp - solution vector for temperature at time n+1
  real, dimension(1:nx_cells) :: Mb, Vd, Vdp

  ! Ma - subdiagonal elements of solution matrix
  real, dimension(2:nx_cells) :: Ma

  ! Mc - superdiagonal elements
  real, dimension(1:nx_cells-1) :: Mc

  real :: a  ! used as a factor, alpha as described in thesis

  integer :: nx, ny  ! cell number counters
```

```
  ! populate vectors for tridiagonal matrix solve

  do ny = 1, ny_cells
    do nx = 1, nx_cells
     Vd(nx) = pe(nx,ny) / (ne(nx,ny) * kB)
    end do

    do nx = 2, nx_cells-1
      a = (gamma - 1.0) * dt / (2.0 * kB * ne(nx,ny) * dx**2)
      Mb(nx) = 1.0 + a * &
            & (kappaSH(nx+1,ny) + 2.0 * kappaSH(nx,ny) + kappaSH(nx-1,ny))
      Ma(nx) = - a * (kappaSH(nx,ny) + kappaSH(nx-1,ny))
      Mc(nx) = - a * (kappaSH(nx+1,ny) + kappaSH(nx,ny))
    end do

    ! apply appropriate values at the boundaries

    nx = 1
    a = (gamma - 1.0) * dt / (2.0 * kB * ne(nx,ny) * dx**2)
    Mc(nx) = - a * (kappaSH(nx+1,ny) + kappaSH(nx,ny))
    Mb(nx) = 1.0 + a * (kappaSH(nx+1,ny) + kappaSH(nx,ny))

    nx = nx_cells
    a = (gamma - 1.0) * dt / (2.0 * kB * ne(nx,ny) * dx**2)
    Ma(nx) = - a * (kappaSH(nx,ny) + kappaSH(nx-1,ny))
    Mb(nx) = 1.0 + a * (kappaSH(nx,ny) + kappaSH(nx-1,ny))

    ! call solver from numerical recipes

    call tridag_ser(Ma,Mb,Mc,Vd,Vdp)

    ! update electron energy

    do nx = 1, nx_cells
        ee(nx,ny) = ee(nx,ny) + kB * ne(nx,ny) * &
                  & (Vdp(nx) - Vd(nx)) / (gamma - 1.0)
    end do
  end do

end subroutine spitzer_harm_x

subroutine spitzer_harm_y  ! see thesis for a fuller explanation of scheme

  use numerical_routines

  ! VECTORS FOR MATRIX SOLVE

  ! Mb - vector for diagonal elemets of matrix
  ! Vd - vector for temperature at time n
  ! Vdp - solution vector for temperature at time n+1
  real, dimension(1:ny_cells) :: Mb, Vd, Vdp

  ! Ma - subdiagonal elements of solution matrix
  real, dimension(2:ny_cells) :: Ma

  ! Mc - superdiagonal elements
  real, dimension(1:ny_cells-1) :: Mc

  real :: a  ! used as a factor, alpha as described in thesis
  integer :: nx, ny  ! cell number counters

  ! populate vectors for tridiagonal matrix solve
```

```
  do nx = 1, nx_cells
    do ny = 1, ny_cells
     Vd(ny) = pe(nx,ny) / (ne(nx,ny) * kB)
    end do

    do ny = 2, ny_cells-1
      a = (gamma - 1.0) * dt / (2.0 * kB * ne(nx,ny) * dy**2)
      Mb(ny) = 1.0 + a *&
             & (kappaSH(nx,ny+1) + 2.0 * kappaSH(nx,ny) + kappaSH(nx,ny-1))
      Ma(ny) = - a * (kappaSH(nx,ny) + kappaSH(nx,ny-1))
      Mc(ny) = - a * (kappaSH(nx,ny+1) + kappaSH(nx,ny))
    end do

    ! apply appropriate values at the boundaries

    ny = 1
    a = (gamma - 1.0) * dt / (kB * ne(nx,ny) * dx**2)
    Mc(ny) = - a * (kappaSH(nx,ny+1) + kappaSH(nx,ny))
    Mb(ny) = 1.0 + a * (kappaSH(nx,ny+1) + kappaSH(nx,ny))

    ny = ny_cells
    a = (gamma - 1.0) * dt / (kB * ne(nx,ny) * dx**2)
    Ma(ny) = - a * (kappaSH(nx,ny) + kappaSH(nx,ny-1))
    Mb(ny) = 1.0 + a * (kappaSH(nx,ny) + kappaSH(nx,ny-1))

    ! call solver from numerical recipes

    call tridag_ser(Ma,Mb,Mc,Vd,Vdp)

    ! update electron energy

    do ny = 1, ny_cells
      ee(nx,ny) = ee(nx,ny) + kB * ne(nx,ny) * &
                & (Vdp(ny) - Vd(ny)) / (gamma - 1.0)
    end do
  end do

end subroutine spitzer_harm_y

end module thermal_conduction
```

A.2.2 Ion-Electron Equilibration

This module is for the ion-electron equilibration as described in section 2.4.8. The variable names correspond to those found in the description in section 2.5.5, where the numerical method is described.

```
module ie_equilibriation

use global_variables
use fluid_calculations

implicit none
```

```
contains

function b_ie_eq(Ti, Te, nx, ny)  ! calculate equilibriation time b_ie_eq =
                                  ! 1 / (tau_ie * n_i)
  real :: b_ie_eq
  real, intent(in) :: Ti, Te
  integer, intent(in) :: nx, ny
  real :: mi

  mi = Z(nx,ny) * 2.0 * mp

  b_ie_eq = (2.0 * Z(nx,ny)**3 * qe**4 * coullog(nx,ny)) / &
            & (3.0 * (2.0 * pi3)**(3.0/2.0) * mi * me * eps0**2 * &
            & kB**(3.0/2.0) * (Ti/mi + Te/me)**(3.0/2.0))

end function b_ie_eq

subroutine equilibriation  ! see thesis for a fuller explanation of scheme

  real :: Ti_prev, Te_prev
  real :: Ti_new, Te_new
  integer :: nx, ny

  do nx = 1, nx_cells
    do ny = 1, ny_cells

      ! values of T at step n
      Ti_prev = pi(nx,ny) / (ni(nx,ny) * kB)
      Te_prev = pe(nx,ny) / (ne(nx,ny) * kB)

      ! values of T at step n+1
      Ti_new = ((1.0 + ni(nx,ny) * b_ie_eq(Ti_prev,Te_prev,nx,ny) * dt) * &
             & Ti_prev + ne(nx,ny) * b_ie_eq(Ti_prev,Te_prev,nx,ny) * dt * &
             & Te_prev) / (1.0 + (ne(nx,ny) + ni(nx,ny)) * &
             & b_ie_eq(Ti_prev,Te_prev,nx,ny) * dt)
      Te_new = ((1.0 + ne(nx,ny) * b_ie_eq(Ti_prev,Te_prev,nx,ny) * dt) * &
               & Te_prev + ni(nx,ny) * b_ie_eq(Ti_prev,Te_prev,nx,ny) * dt * &
               & Ti_prev) / (1.0 + (ne(nx,ny) + ni(nx,ny)) * &
               & b_ie_eq(Ti_prev,Te_prev,nx,ny) * dt)

      ! apply new values to ion and electron energy
      ei(nx,ny) = ei(nx,ny) + (kB * ni(nx,ny) / (gamma - 1.0)) * &
                                                & (Ti_new - Ti_prev)
      ee(nx,ny) = ee(nx,ny) + (kB * ne(nx,ny) / (gamma - 1.0)) * &
                                                & (Te_new - Te_prev)
    end do
  end do

end subroutine equilibriation

end module ie_equilibriation
```

Appendix B

Ray Tracing Code

B.1 Description of Model

The code works by creating rays starting randomly from the parabolic mirror, and ending distributed randomly in the focal spot. The parameters used are based on the experiment as described in chapter 4. This means that at the mirror the beam had a Gaussian profile with a FWHM of 0.6 m, the mirror having a diameter of 0.65 m. At the focal point of the laser the beam was then modelled as having a Gaussian shape with a FWHM of 8 µm. The distance from the mirror to the focal spot was 1.95 m. Each ray was given a random start and end point according to the appropriate Gaussian probability distribution, using a pseudo-random number generator given in *Numerical Recipes in Fortran 90* [76].

Details of the intersection of a ray and a cone are detailed in *Geometric Tools for Computer Graphics* [125]. A cone can be defined by a point $\boldsymbol{V}$, at the cone vertex, and a direction $\boldsymbol{A}$ along the axis of symmetry inside the cone. The intersection of this with a line $\boldsymbol{X}(t) = \boldsymbol{P} + t\boldsymbol{D}$ must satisfy the equation

$$\boldsymbol{A} \cdot \left(\frac{\boldsymbol{X} - \boldsymbol{V}}{|\boldsymbol{X} - \boldsymbol{V}|} \right) = \cos\theta, \tag{B.1}$$

where $\cos\theta$ is the angle between the cone wall and $\boldsymbol{A}$. To find this solution the cone equation is squared

$$(\boldsymbol{A} \cdot (\boldsymbol{X} - \boldsymbol{V}))^2 = (\cos^2\theta)|\boldsymbol{X} - \boldsymbol{V}|^2. \tag{B.2}$$

This gives solutions for the cone and a mirror of the cone, defined by $\boldsymbol{V}$ and $-\boldsymbol{A}$.

This can be written as

$$(\boldsymbol{X} - \boldsymbol{V})^T M(\boldsymbol{X} - \boldsymbol{V}) = 0, \tag{B.3}$$

where $M = (\boldsymbol{A}\boldsymbol{A}^T - (\cos^2\theta)\boldsymbol{I})$ and using the condition and $\boldsymbol{A} \cdot (\boldsymbol{X} - \boldsymbol{V}) \geq 0$ to ensure only values for the positive cone are found. This can be then formulated in terms of a quadratic to find t. Similarly the intersection of the ray with a plane can be found, giving the intersection at the cone tip. The reflection at the surface can be calculated by

$$\boldsymbol{X}' = 2(\boldsymbol{N} \cdot \boldsymbol{X})\boldsymbol{N} - \boldsymbol{X}, \tag{B.4}$$

where $\boldsymbol{X}'$ is the reflected vector and $\boldsymbol{N}$ is the normal to the reflection surface.

The ray is propagated in this way until it escapes the cone. The reflection and absorption at each point on the surface is found, and summed up over 2 billion rays, the large number required to prevent noise in the lower intensity regions.

B.2 Code Verification and Selected Results

In the first plot of figure B.1 a sample problem is shown for the intensity at a flat surface, for a focal spot created with a FWHM of 8 µm. No reflections were allowed in this test case. The expected Gaussian curve is plotted alongside, and good agreement is seen between the two, showing the code is working as expected. In the second plot of figure B.1 the lower intensity region further from the centre of the laser focus is shown, which is also in good agreement until very low intensities are reached. The noise in this can be resolved by using more rays in the code.

Figure B.2 shows two selected examples of rays propagating through the cone, one reaching the cone tip and one escaping after hitting the cone walls. Figure B.3 shows 30 rays being traced through the cone, which illustrates the rays passing through the focus of the cone. Note that in these rays the geometry is shown as used in the code, although in two dimensions rather than three. Hence the defocus position is at +400 µm, which differs to the convention used in chapter 4. The overall results from the code were shown in figure 4.19.

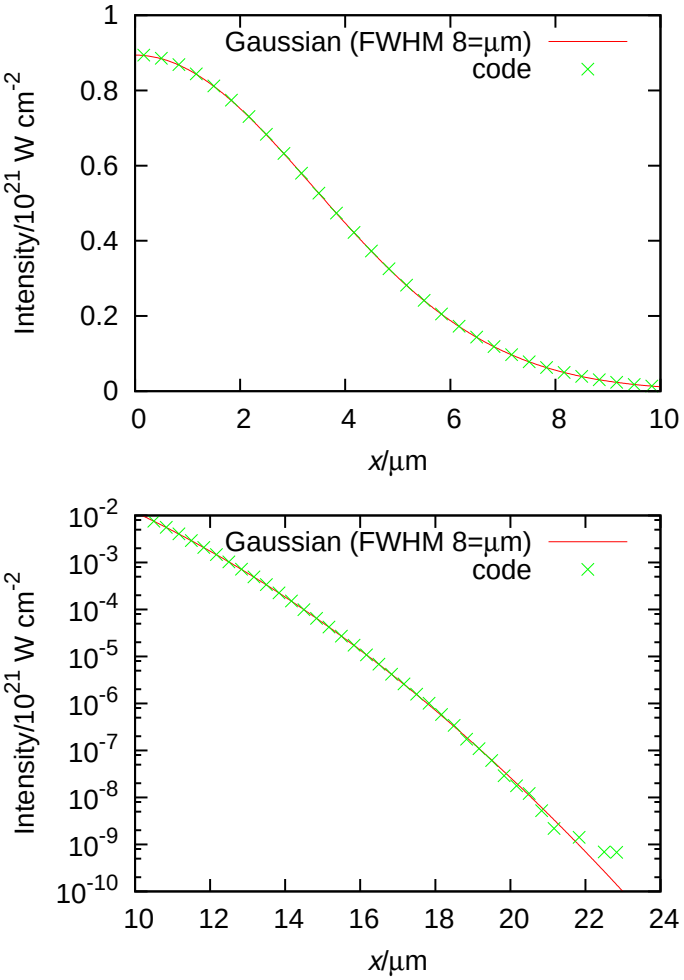

Figure B.1: Top: the output from the code for the intensity across a flat surface and the expected analytic solution. Bottom: output from the code in the regions further from the centre of the beam, plotted on a log scale. Here it can be seen that further out, in the lower intensity region some noise starts to affect the results. In this case the focal spot is created with a FWHM of 8 µm, and the total laser power is 10^{15} W cm^{-2}, leading to a peak intensity of 10^{21} W cm^{-2} as expected.

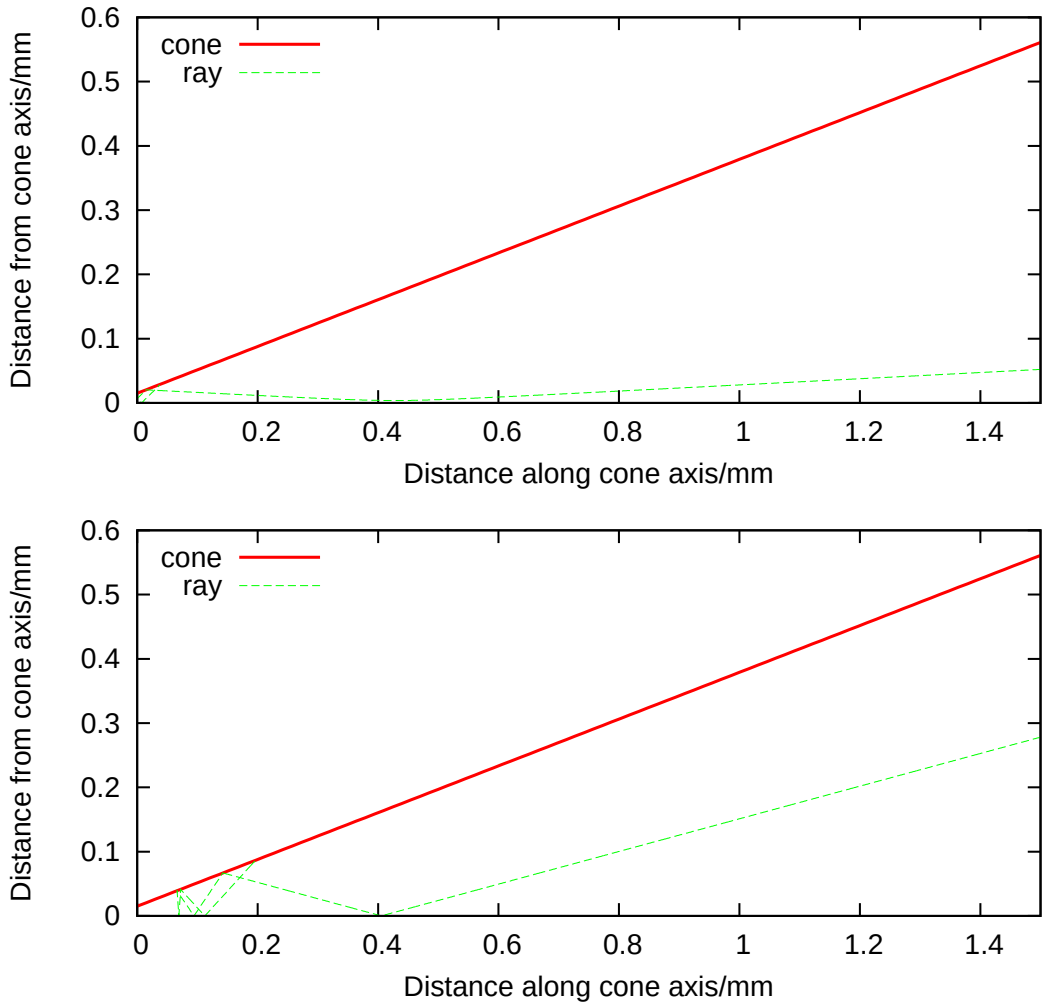

Figure B.2: Top: single ray from ray tracing code, which first hits the wall and is then reflected onto the cone tip. Bottom: ray that is reflected and escapes without hitting the cone tip. In both these cases the focus is 400 µm before the cone tip. The coordinates shown are in a cylindrical geometry, with r on the vertical axis and z on the horizontal axis. The escaping ray is not shown. The thick red line illustrates the cone wall, and the plane of the cone tip lies along the vertical axis.

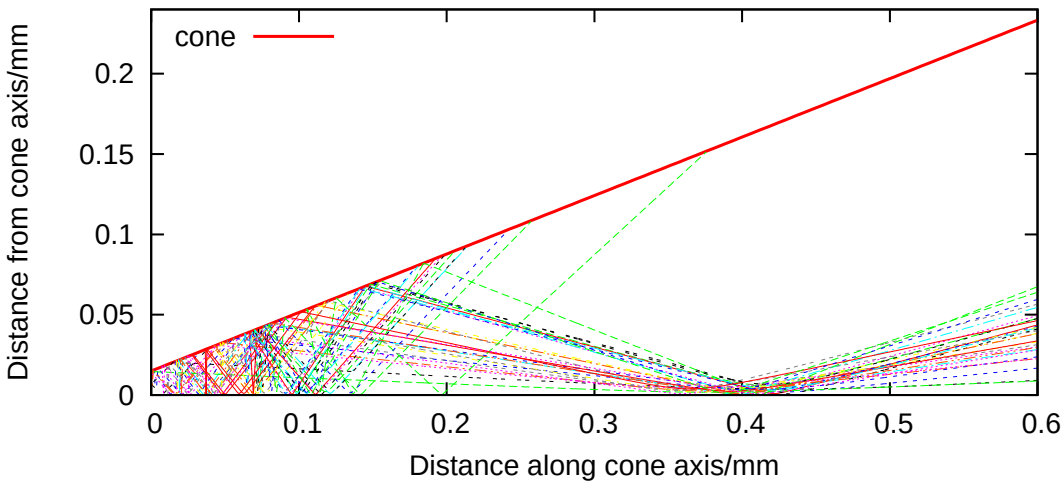

Figure B.3: A similar example of rays to figure B.2, again with the focus 400 µm before the cone tip. Here the whole cone is not shown, but a zoomed in view of the cone is given. 30 rays are illustrated in the figure.

B.3 Source Code

This code was written in Fortran 90 and tested with the GNU Fortran Compiler. The setup shown, with 2 billion rays, took around 2.5 hours to complete on an Intel Core 2 Duo processor. The code requires the Numerical Recipes subroutine `ran2_s`, to generate pseudo-random numbers, and this in turn relies on the modules `ran_state`, `nrtype` and `nrutil`. These are all listed in *Numerical Recipes for Fortran 90* [76].

```
program conetrace

use ran2_mod ! provided by Numerical Recipes

implicit none

  ! all values used correspond to SI units

  ! USEFUL PARAMETERS

  integer, parameter :: R4B = selected_real_kind(6,37)
  integer, parameter :: R8B = selected_real_kind(15,307)

  real(R8B), parameter :: pi = 3.14159265358979

  ! RAY PARAMETERS
```

```
  ! array for one ray:
  ! 'x' dimension is the reflection number, 0, 1, 2... n_reflections
  ! 'y' dimension contains 8 variables; P1(1:3), D(1:3), energy still in ray,
  ! +1.0 if ray has been reflected from cone wall or -1.0 otheriwse
  ! P1 and D are vectors for the ray, such that X = P1 + t*D
  real(R8B), dimension(:,:), allocatable :: ray

  ! n_rays is number of rays used, n_reflections maximum reflections
  integer :: n_rays = 2000000000, n_reflections = 10

  ! n_outputs determines number of ray trajectories to be outputted
  integer :: n_outputs = 1000

  ! output of ray coordinates is done by writing out values at set
  ! intervals along the z-axis, in steps of dz
  real(R8B) :: dz = 1.0D-6

  ! n_bins_tip is number of bins for outputting intensity across tip, same
  ! interval is used for the number of bins along the wall - given by dx
  integer :: n_bins_tip = 300, n_bins_wall
  real(R8B) :: dx
  real(R8B), dimension(:), allocatable :: tip_intensities(:), &
                                          & wall_intensities(:)

  ! LASER PARAMETERS

  ! the additional minus means that the value in brackets corresponds
  ! to the defocus sign convention used in the the thesis
  real(R8B) :: focus_position = -(-400.0d-6)

  ! following parameters for Vulcan PetaWatt as used in experiment
  real(R8B) :: mirror_distance = 0.650 * 3.0
  real(R8B) :: mirror_diameter = 0.650
  real(R8B) :: fwhm_mirror = 0.600
  real(R8B) :: fwhm_focal_spot = 8.0D-6
  real(R8B) :: laser_power = 1.0D15

  ! CONE PARAMETERS

  ! specific to cone used in experiment
  real(R8B) :: cone_angle = pi/9.0
  real(R8B) :: cone_length = 1.5D-3
  real(R8B) :: cone_tip_radius = 15.0D-6
  real(R8B) :: cone_height

  print*, 'Setting initial parameters...'
  call set_initial_parameters
  print*, 'Tracing and outputting rays...'
  call trace_rays

  print*, 'Outputting intensities...'
  call output_tip_intensities
  call output_wall_intensities
  call output_tip_energies
  call output_wall_energies
  print*, 'Done!'

contains

subroutine set_initial_parameters
```

```
  ! finish setting cone parameters
  cone_height = cone_tip_radius + cone_length * tan(cone_angle)

  ! finish setting intensity output bins
  dx = cone_tip_radius / real(n_bins_tip)
  allocate(tip_intensities(1:n_bins_tip))

  n_bins_wall = ceiling((cone_length/cos(cone_angle)) / dx)
  allocate(wall_intensities(1:n_bins_wall))

  wall_intensities = 0.0
  tip_intensities = 0.0

end subroutine set_initial_parameters

subroutine trace_rays

  ! counters, ray number and reflection number respectively
  integer :: i, j, j_temp

  ! P1(1:3) start of ray, P2(1:3) end of ray, D = P2 - P1
  ! t is used such that X = P1 + t * D
  real(R8B) :: P1(1:3), P2(1:3), D(1:3), t

  ! two random numbers, between -1 and 1
  real(R8B) :: random1, random2
  real(R4B) :: random ! require single precison for NR routine

  ! r is a radius based on random1 and random2
  real(R8B) :: r

  ! stanard deviation of the Gaussians at mirror and focus
  real(R8B) :: sigma_mirror, sigma_focus

  ! calculated intersection positions, X1, X2, X3
  ! 1.0 real intersection, -1.0 intersection outside of extent of tip or wall
  real(R8B) :: cone_wall(1:4), cone_tip(1:4)

  ! initialising

  allocate(ray(1:n_reflections,8))

  sigma_mirror = fwhm_mirror / (2.0 * sqrt(2.0 * log(2.0)))
  sigma_focus = fwhm_focal_spot / (2.0 * sqrt(2.0 * log(2.0)))

rayloop: do i = 1, n_rays
    ! find a random start position on parabolic mirror
rndloop_mirror: do
      call ran2_s(random)
      random1 = (random - 0.5) * 2.0
      call ran2_s(random)
      random2 = (random - 0.5) * 2.0
      r = random1**2 + random2**2
      ! limit maximum of r to 1.0, so results are in a circle
      if(r .gt. 1.0) cycle rndloop_mirror
      ! distribute rays by a Gaussian distribution
      P1(1) = sqrt(-2.0 * sigma_mirror**2 * log(r) / r) * random1
      P1(2) = sqrt(-2.0 * sigma_mirror**2 * log(r) / r) * random2
      P1(3) = mirror_distance
      ! check if P1 is on mirror, if it is can exit loop and continue...
      if((P1(1)**2 + P1(2)**2) .lt. mirror_diameter) exit rndloop_mirror
    end do rndloop_mirror
```

```
    ! find a random end position at the focal point
rndloop_focus: do
      call ran2_s(random)
      random1 = (random - 0.5) * 2.0
      call ran2_s(random)
      random2 = (random - 0.5) * 2.0
      r = random1**2 + random2**2
      ! limit maximum of r to 1.0, so results are in a circle
      if(r .gt. 1.0) cycle rndloop_focus
      ! distribute rays by a Gaussian distribution
      P2(1) = sqrt(-2.0 * sigma_focus**2 * log(r) / r) * random1
      P2(2) = sqrt(-2.0 * sigma_focus**2 * log(r) / r) * random2
      P2(3) = focus_position
      exit rndloop_focus
    end do rndloop_focus

    D = P2 - P1  ! direction vector of ray

    t = (cone_length - P1(3))/D(3) ! find value of t at the cone entrance

    do j = 1, 3
      ray(1:n_reflections, j) = P1(j) + t * D(j)
      ray(1:n_reflections, j + 3) = D(j)
    end do

    ray(1:n_reflections,7) = laser_power/real(n_rays) ! initial ray energy
    ray(1,8) = -1.0  ! (-1.0 no cone wall intersection)

!Tracing

    if(sqrt(abs(ray(1, 1))**2 + abs(ray(1, 2))**2) .gt. cone_height) then
      ! if the ray is not inside the cone ignore and restart loop
      cycle rayloop
    end if

reflectloop: do j = 1, n_reflections
      if (j .eq. n_reflections) then
        print*, 'WARNING! - Maximum reflections reached!', i, j
        exit reflectloop
      end if

      j_temp = j

      call output_ray(i, j)

      ! calculate and check for the intersections with the tip and wall
      cone_wall = cone_wall_intersection(j_temp)
      cone_tip = cone_tip_intersection(j_temp)

      ! now the intersections are checked, perform the reflection,
      ! or exit loop for reflections
      ! (error statements should be redundant, left for robustness)
      if (ray(j, 6) .lt. 0.0)  then ! ray going into cone
        if ((cone_wall(4) .gt. 0.0) .and. (cone_tip(4) .gt. 0.0)) then
          stop 'ERROR! - Multiple intersections found!'
        else if (cone_wall(4) .gt. 0.0) then
          call cone_wall_reflection(j, cone_wall)
        else if (cone_tip(4) .gt. 0.0) then
          call cone_tip_reflection(j, cone_tip)
        else
          stop 'ERROR! - Ray going into cone but not intersecting tip or wall!↩
              '
```

```
        end if
      else if (ray(j, 6) .gt. 0.0) then ! ray going out of cone
        if (cone_wall(4) .gt. 0.0) then
          call cone_wall_reflection(j, cone_wall)
        else
          exit reflectloop
        end if
      else
        stop 'ERROR! - Ray not going into or out of cone!'
      end if
    end do reflectloop
  end do rayloop

end subroutine trace_rays

function cone_tip_intersection(n_reflection)

  ! this subroutine finds where a ray will intersect a plane that represents
  ! the cone tip, and sets cone_tip_intersection(4) = 1.0 if this intersection
  ! is a real position on the cone tip, -1.0 otherwise

  integer, intent(IN) :: n_reflection
  real(R8B) :: cone_tip_intersection(1:4)

  integer :: i
  real(R8B) :: t

  t = (0.0 - ray(n_reflection, 3))/ray(n_reflection, 6)

  do i = 1, 3
    cone_tip_intersection(i) = ray(n_reflection, i) + &
                               & t * ray(n_reflection, i + 3)
  end do

  if((sqrt(cone_tip_intersection(1)**2 + cone_tip_intersection(2)**2) .lt. &
    & cone_tip_radius) .and. (ray(n_reflection, 6) .lt. 0.0)) then
    cone_tip_intersection(4) = 1.0
  else
    cone_tip_intersection(4) = -1.0
  end if

end function cone_tip_intersection

function cone_wall_intersection(n_reflection)

  ! this subroutine finds where a ray will intersect the cone wall, and sets
  ! cone_wall_intersection(4) = 1.0 if this intersection is a real position
  ! on the cone wall, -1.0 otherwise

  ! A, V, M and X are used as described in Appendix B of the thesis

  integer :: i, j
  integer, intent(IN) :: n_reflection
  real(R8B) :: cone_wall_intersection(1:4)

  real(R8B) :: P1(1:3), D(1:3)
  real(R8B) :: V(1:3), A(1:3)
  real(R8B) :: M(1:3,1:3)
  real(R8B) :: X1(1:3), X2(1:3)
  real(R8B) :: DELTA(1:3), TEMP(1:3) ! temporary dummy vectors
  real(R8B) :: c0, c1, c2 ! quadratic equation c2*x^2 + c1*x + c0 = 0
  real(R8B) :: t1, t2 ! 2 roots of equation, can be 2 intersections on cone
```

```
  do i = 1, 3
    P1(i) = ray(n_reflection, i)
    D(i) = ray(n_reflection, i + 3)
  end do

  V(1) = 0.0
  V(2) = 0.0
  V(3) = - cone_tip_radius/tan(cone_angle)

  A(1) = 0.0
  A(2) = 0.0
  A(3) = 1.0

  DELTA = P1 - V

  do i = 1, 3
    do j = 1, 3
      M(i,j) = A(i) * A(j)
      if (i .eq. j) M(i,j) = M(i,j) - cos(cone_angle)**2
    end do
  end do

  TEMP = 0.0
  do i = 1, 3
    do j = 1, 3
      TEMP(i) = TEMP(i) + M(i,j) * D(j)
    end do
  end do

  c2 = 0.0
  do i = 1,3
    c2 = c2 + TEMP(i) * D(i)
  end do

  TEMP = 0.0
  do i = 1, 3
    do j = 1, 3
      TEMP(i) = TEMP(i) + M(i,j) * DELTA(j)
    end do
  end do

  c1 = 0.0
  do i = 1,3
    c1 = c1 + TEMP(i) * D(i)
  end do

  TEMP = 0.0
  do i = 1, 3
    do j = 1, 3
      TEMP(i) = TEMP(i) + M(i,j) * DELTA(j)
    end do
  end do

  c0 = 0.0
  do i = 1,3
    c0 = c0 + TEMP(i) * DELTA(i)
  end do

  t1 = (-(c1*2.0) + sqrt((c1*2.0)**2 - 4.0 * c2 * c0))/(2.0 * c2)
  t2 = (-(c1*2.0) - sqrt((c1*2.0)**2 - 4.0 * c2 * c0))/(2.0 * c2)
```

```
  ! the two intersection points
  X1 = P1 + t1 * D
  X2 = P1 + t2 * D

330 if (D(3) .lt. 0.0) then ! ray going into cone

    ! checks to see if X1 and/or X2 intersect with the real cone,
    ! and if both do determines which comes first, outputs X1 or X2

    if (((X1(3) .gt. 0) .and. (X1(3) .lt. cone_length)) .and. &
     & ((X2(3) .gt. 0) .and. (X2(3) .lt. cone_length))) then
      if (X1(3) .lt. X2(3)) then
        do i = 1, 3
          cone_wall_intersection(i) = X1(i)
340     end do
        cone_wall_intersection(4) = 1.0
        return
      else if (X2(3) .lt. X1(3)) then
        do i = 1, 3
          cone_wall_intersection(i) = X2(i)
        end do
        cone_wall_intersection(4) = 1.0
        return
      end if
350 else if ((X1(3) .gt. 0) .and. (X1(3) .lt. cone_length)) then
      if (ray(n_reflection,8) .lt. 0.0) then
        do i = 1, 3
          cone_wall_intersection(i) = X1(i)
        end do
        cone_wall_intersection(4) = 1.0
        return
      end if
    else if ((X2(3) .gt. 0) .and. (X2(3) .lt. cone_length)) then
      if (ray(n_reflection,8) .lt. 0.0) then
360     do i = 1, 3
          cone_wall_intersection(i) = X2(i)
        end do
        cone_wall_intersection(4) = 1.0
        return
      end if
    end if

    cone_wall_intersection = -1.0 ! set cone_wall_intersection(4) to -1.0,
                                  ! no intersection
370
  else if (D(3) .gt. 0.0) then ! ray going out of cone

    ! checks to see if X1 and/or X2 intersect with the real cone,
    ! and if both do determines which comes first, outputs X1 or X2

    if (((X1(3) .gt. 0) .and. (X1(3) .lt. cone_length)) .and. &
     & ((X2(3) .gt. 0) .and. (X2(3) .lt. cone_length))) then
      if (X1(3) .gt. X2(3)) then
        do i = 1, 3
380       cone_wall_intersection(i) = X1(i)
        end do
        cone_wall_intersection(4) = 1.0
        return
      else if (X2(3) .gt. X1(3)) then
        do i = 1, 3
          cone_wall_intersection(i) = X2(i)
        end do
```

```
        cone_wall_intersection(4) = 1.0
        return
      end if
    else if ((X1(3) .gt. 0) .and. (X1(3) .lt. cone_length)) then
      if (ray(n_reflection,8) .lt. 0.0) then
        do i = 1, 3
          cone_wall_intersection(i) = X1(i)
        end do
        cone_wall_intersection(4) = 1.0
        return
      end if
    else if ((X2(3) .gt. 0) .and. (X2(3) .lt. cone_length)) then
      if (ray(n_reflection,8) .lt. 0.0) then
        do i = 1, 3
          cone_wall_intersection(i) = X2(i)
        end do
        cone_wall_intersection(4) = 1.0
        return
      end if
    end if

    cone_wall_intersection = -1.0 ! set cone_wall_intersection(4) to -1.0,
                                  ! no intersection

  else
    stop 'ERROR! - Ray not going forward or backwards'
  end if

end function cone_wall_intersection

subroutine cone_tip_reflection(n_reflection, cone_tip)

  ! calculates reflection of ray from cone tip,
  ! including absorption and new ray energy

  ! N as used in appendix B of thesis,
  ! L1, L2 incoming and reflected rays respectively

  integer, intent(IN) :: n_reflection
  real(R8B), intent(IN) :: cone_tip(1:4)

  integer :: i
  real(R8B) :: N(1:3), L1(1:3), L2(1:3)
  real(R8B) :: NdotL1, NdotL2 ! N dot product L1, L2
  real(R8B) :: r

  do i = 1, 3
    L1(i) = ray(n_reflection, i+3)
  end do

  N(1) = 0.0
  N(2) = 0.0
  N(3) = 1.0

  ! normalise vectors
  L1 = L1 / sqrt(L1(1)**2 + L1(2)**2 + L1(3)**2)

  NdotL1 = 0.0
  do i = 1, 3
    NdotL1 = NdotL1 + N(i) * L1(i)
  end do
```

```
  do i = 1, 3
    L2(i) = L1(i) - 2.0 * NdotL1 * N(i)
  end do

  NdotL2 = 0.0
  do i = 1, 3
    NdotL2 = NdotL2 + N(i) * L2(i)
  end do

  do i = 1, 3
    ray(n_reflection+1, i) = cone_tip(i)
    ray(n_reflection+1, i + 3) = L2(i)
  end do

  if (acos(NdotL2) .gt. pi/2.0) then
    stop 'ERROR! - NdotL2 .gt. pi/2.0! While in cone_tip_reflection.'
  end if

  ! reduce ray energy after reflection and absorption
  ray(n_reflection+1, 7) = ray(n_reflection, 7) * absorption(acos(NdotL2))

  r = sqrt(cone_tip(1)**2 + cone_tip(2)**2)

  tip_intensities(ceiling(r/dx)) = tip_intensities(ceiling(r/dx)) &
  & + ray(n_reflection, 7) * absorption(acos(NdotL2))

  ray(n_reflection+1,8) = -1.0 ! -1.0 cone tip reflection

end subroutine cone_tip_reflection

subroutine cone_wall_reflection(n_reflection, cone_wall)

  ! calculates reflection of ray from cone wall,
  ! including absorption and new ray energy

  ! N as used in appendix B of thesis,
  ! L1, L2 incoming and reflected rays respectively

  integer, intent(IN) :: n_reflection
  real(R8B), intent(IN) :: cone_wall(1:4)

  integer :: i
  real(R8B) :: N(1:3), L1(1:3), L2(1:3)
  real(R8B) :: NdotL1, NdotL2 ! N dot product L1, L2

  do i = 1, 3
    L1(i) = ray(n_reflection, i+3)
  end do

  ! work out L1 x L2, L1 line from intersection to vertex of cone,
  ! L2 line tangential to cone surface
  N(1) = - cone_wall(1) * (cone_wall(3) + cone_tip_radius/tan(cone_angle))
  N(2) = - cone_wall(2) * (cone_wall(3) + cone_tip_radius/tan(cone_angle))
  N(3) = (cone_wall(1)**2 + cone_wall(2)**2)

  ! normalise vectors
  N = N / sqrt(N(1)**2 +N(2)**2 + N(3)**2)
  L1 = L1 / sqrt(L1(1)**2 + L1(2)**2 + L1(3)**2)

  NdotL1 = 0.0
  do i = 1, 3
    NdotL1 = NdotL1 + N(i) * L1(i)
```

```
  end do

  do i = 1, 3
    L2(i) = -(2.0 * NdotL1 * N(i) - L1(i))
  end do

  NdotL2 = 0.0
  do i = 1, 3
    NdotL2 = NdotL2 + N(i) * L2(i)
  end do

  do i = 1, 3
    ray(n_reflection+1, i) = cone_wall(i)
    ray(n_reflection+1, i + 3) = L2(i)
  end do

  if (acos(NdotL2) .gt. pi/2.0) then
    stop 'ERROR - NdotL2 .gt. pi/2.0! While in cone_wall_reflection.'
  end if

  ray(n_reflection+1, 7) = ray(n_reflection, 7) * absorption(acos(NdotL2))

  wall_intensities(ceiling((cone_wall(3)/cos(cone_angle))/dx)) = &
  & wall_intensities(ceiling((cone_wall(3)/cos(cone_angle))/dx)) &
  & + ray(n_reflection, 7) * absorption(acos(NdotL2))

  ray(n_reflection+1,8) = 1.0 ! 1.0 cone wall reflection

end subroutine cone_wall_reflection

function absorption(angle)

  ! calculates absorption in the target based on an incident angle,
  ! using a predetermined model

  real(R8B) :: absorption
  real(R8B) :: angle

  angle = angle * 180.0 / pi ! convert to degrees for clarity

  if (angle .lt. 0.0) then
    stop 'ERROR! - Angle less than 0!'
  else if ((angle .ge. 0.0) .and. (angle .lt. 55.0)) then
    absorption = 0.65
  else if ((angle .ge. 55.0) .and. (angle .lt. 90.0)) then
    absorption = ((90.0 - angle) / 35.0) * 0.65
  else if (angle .ge. 90.0) then
    stop 'ERROR! - Angle greater than 90 degrees!'
  else
    stop 'ERROR! - Angle NaN?'
  end if

end function absorption

subroutine output_ray(n_ray, n_reflection)

  ! subroutine outputs number of rays specified by n_outputs into files
  ! starting with output/ray_000000001.txt, output/ray_000000002.txt...

  ! the rays are given on a 2D plane of x, y coordinates

  integer, intent(IN) :: n_ray, n_reflection
```

```
  integer :: i
  character(24) :: rayfname
  real(R8B) :: P1(1:3), P2(1:3)
  real(R8B) :: t, r
  integer :: n_points

  if (n_reflection .eq. 1) return
  if (mod(n_ray, n_rays/n_outputs) .ne. 0) return

  do i = 1, 3
    P1(i) = ray(n_reflection - 1, i)
    P2(i) = ray(n_reflection, i)
  end do

  n_points = ceiling(abs((P2(3) - P1(3)) / dz))

  write(rayfname,'(A24)') 'output/ray_XXXXXXXXX.txt'
  write(rayfname(11:20),'(I10)') n_ray/(n_rays/n_outputs) + 1000000000
  write(rayfname(11:11),'(A1)') '_'
  open(500, file=rayfname)

  do i = 1, n_points
    t = real(i - 1)/real(n_points)
    r = sqrt((P1(1) + t * (P2(1) - P1(1)))**2 + &
      & (P1(2) + t * (P2(2) - P1(2)))**2)
    write(500,*) P1(3) + t * (P2(3) - P1(3)), r
  end do

  if (n_reflection .eq. 2) print*, 'Output ', n_ray/(n_rays/n_outputs), &
                                & ' of ', n_outputs

end subroutine output_ray

subroutine output_tip_intensities

  integer :: i
  character(14) :: tipfname

  write(tipfname,'(A14)') 'output/tip.txt'
  open(501, file=tipfname)

  do i = 1, n_bins_tip
    write(501,*) 0.0, (real(i) - 0.5) * dx, &
    & tip_intensities(i) / (pi * ((real(i) * dx)**2 - (real(i-1) * dx)**2))
  end do

  close(501)

end subroutine output_tip_intensities

subroutine output_wall_intensities

  integer :: i
  character(15) :: wallfname

  real(R8B) :: s1, s2

  write(wallfname,'(A15)') 'output/wall.txt'
  open(502, file=wallfname)

  do i = 1, n_bins_wall
```

```
    s1 = (cone_tip_radius / sin(cone_angle)) + real(i-1) * dx
    s2 = (cone_tip_radius / sin(cone_angle)) + real(i) * dx

    write(502,*) (real(i) - 0.5) * dx * cos(cone_angle), &
    & cone_tip_radius + (real(i) - 0.5) * dx * sin(cone_angle), &
    & wall_intensities(i) / &
    & (pi * sin(cone_angle) * (s2**2 - s1**2))
  end do

  close(502)

end subroutine output_wall_intensities

subroutine output_tip_energies

  integer :: i
  character(16) :: tipefname

  write(tipefname,'(A16)') 'output/tip_e.txt'
  open(501, file=tipefname)

  do i = 1, n_bins_tip
    write(501,*) 0.0, (real(i) - 0.5) * dx, tip_intensities(i)
  end do

  close(501)

end subroutine output_tip_energies

subroutine output_wall_energies

  integer :: i
  character(17) :: wallefname

  write(wallefname,'(A17)') 'output/wall_e.txt'
  open(502, file=wallefname)

  do i = 1, n_bins_wall
    write(502,*) (real(i) - 0.5) * dx * cos(cone_angle), &
    & cone_tip_radius + (real(i) - 0.5) * dx * sin(cone_angle), &
    & wall_intensities(i)
  end do

  close(502)

end subroutine output_wall_energies

end program conetrace
```

Nomenclature

Where appropriate the definition is given, or the equation or section number where the variable is first defined. Vectors are denoted in bold, such as $\boldsymbol{A}$, and the scalar version of the same quantity is denoted as A. Individual components of the vector are denoted either with numbers or where appropriate the subscripts x, y and z. Tensors are denoted with a double arrow, such as $\overleftrightarrow{\boldsymbol{A}}$. Subscripts j and k are used for Cartesian tensor notation, i is omitted to avoid ambiguity. Some symbols are multiply defined, in this case the appropriate meaning should be clear from the context. Subscripts are listed separately where appropriate. Units in the subscript indicate the variable is in terms of those units. The convention used in differencing schemes is shown in figure 2.2.

Roman Symbols

a	Acceleration
A_i	Airy Function
A_t	The Atwood number
$\boldsymbol{B}$	Magnetic Field
b	The Distance of Closest Approach for a Scatter
b_0	The Impact Parameter for a 90° Scatter
c	The Speed of Light in Vacuum
C_p	Constant Pressure Specific Heat
c_s	Sound Speed $[c_s = \sqrt{\gamma p/\rho} = \sqrt{\gamma k_B T_e/m_i}]$
C_V	Constant Volume Specific Heat
$\boldsymbol{E}$	Electric Field
E	Total Energy
e	The Elementary Charge, e.g. Charge on a Proton

e	The Internal Energy Density, Including Kinetic, Thermal and Magnetic
$\boldsymbol{F}$	Force
f	Distribution Function [$f = f(\boldsymbol{x}, \boldsymbol{v}, t)$]
f_B	Fraction of Fuel Burned
G	Gain, Ratio of Energy in to Energy Out
H_B	The Burn Parameter [Defined Equation 1.22]
I	Laser Intensity
$\boldsymbol{J}$	Electric Current Density
k	Wave Number [$k = 2\pi/\lambda$]
k_B	Boltzmann's Constant
L	Scale Length
m	Particle Mass
m	Total Mass, e.g. in ICF Target
n	Number Density
$\overleftrightarrow{\boldsymbol{P}}$	Pressure Tensor
$\boldsymbol{p}_{sr}$	Momentum Change in Species s due to Collisions with Species r
P	Power
p	Pressure Scalar
$\boldsymbol{Q}$	Heat Flux
q	Effective Pressure
q	Total Charge on Species
R	Radius of Fuel
R_M	Magnetic Reynolds Number
T	Temperature
t	Time Coordinate
$\boldsymbol{u}$	Velocity
$\boldsymbol{v}$	Velocity
V	Volume
Z	Atomic Number

Greek Symbols

ϵ_0	Permittivity of Free Space
η	Resistivity

$\eta_\parallel$, $\eta_\perp$	Resistivity Parallel or Perpendicular to the Magnetic Field
γ	Adiabatic Index or Ratio of Specific Heats [$\gamma = C_p/C_V$]
λ	Wavelength or Mean Free Path
λ_d	Debye Length [Defined Equation 2.13]
$\ln \Lambda$	Coulomb Logarithm [Defined Section 2.4.3]
μ_0	Permeability of Free Space
μ_{sr}	Reduced Mass for Species s and r [$\mu_{sr} = m_s m_r/(m_s + m_r)$]
∇_v	Gradient in Velocity Space
ν_{sr}	Collision Frequency of Species s with Species r [Defined Equation 2.41]
ω	Angular Frequency
ϕ	Electric Potential
ψ	Efficiency
ρ	Mass Density
ρ_q	Charge Density
σ	Conductivity
σ	Reaction Cross Section
σ	Rayleigh-Taylor Instability Growth Rate
τ	Total time, e.g. energy confinement, laser pulse, equilibration

Subscripts

0	Initial Value, at Time $t = 0$
a	Ablation, e.g. Ablation Velocity
$brem$	Bremsstrahlung
c	Critical Surface, e.g. Critical Density Surface
$coll$	Collision Term
$conf$	Confinement, e.g. confinement time
D	Deuterium Ions
drv	Driver (such as Laser Driver)
DT	Deuterium-Tritium Reaction, e.g. Energy of Reaction
e	Electron
f	Fast Electrons
fus	Total Fusion Reactions
gen	Generator Efficiency

H	Hydrodynamic, e.g. Hydrodynamic Scale Length
h	Heavier Fluid
L	Laser, e.g. Laser Wavelength, Laser Frequency
l	Lighter Fluid
max	Maximum Value of Fluid Quantity in Problem at Current Time Step
p	Plasma, e.g. Plasma Frequency
S	Source Terms
s,r	Species s, r of Charged Particles
T	Tritium Ions
tot	Total Pressure, Including Magnetic

Bibliography

[1] F. J. McClung and R. W. Hellwarth. Giant Optical Pulsations from Ruby. *Journal of Applied Physics*, **33** 3 pp. 828–829, 1962. Web: dx.doi.org/10.1063/1.1777174. 23

[2] C. H. Townes. *How the Laser Happened: Adventures of a Scientist*. Oxford University Press, New York, US, 1999. Web: www.worldcat.org/oclc/39123151. 23

[3] R. Priddle, editor. *World Energy Outlook*, International Energy Agency, Paris, France, p. 42. 2009. Web: www.worldcat.org/oclc/470266911. 23

[4] D. MacKay. *Sustainable Energy: without the hot air*, UIT Cambridge Ltd., Cambridge, UK, chap. 18, 24. 2009. Web: www.worldcat.org/oclc/612088885. 24

[5] J. Friedberg. *Plasma Physics and Fusion Energy*, Cambridge University Press, Cambridge, UK, chap. 1, 5, 10. 2007. Web: www.worldcat.org/oclc/71808136. 24, 25, 40, 57, 67, 68

[6] J. D. Hubba. *NRL Plasma Formulary*, Naval Research Laboratory, Washington DC, US, pp. 44–45. 2009. Web: wwwppd.nrl.navy.mil/nrlformulary. 11, 25, 36, 63, 64

[7] S. Atzeni and M. Ciampi. Burn performance of fast ignited, tritium-poor ICF fuels. *Nuclear Fusion*, **37** 12 p. 1665, 1997. Web: dx.doi.org/10.1088/0029-5515/37/12/I01. 26

[8] S. Atzeni and J. Meyer-ter-Vehn. *The Physics of Inertial Fusion: beam plasma interaction, hydrodynamics, hot dense matter*, Oxford University

Press, Oxford, UK, chap. 1–4, 8–9, 11–12. 2009. Web: www.worldcat.org/oclc/690564474. 11, 26, 27, 32, 33, 34, 36, 40, 68

[9] M. Tabak. What is the role of tritium-poor fuels in ICF? *Nuclear Fusion*, **36** 2 p. 147, 1996. Web: dx.doi.org/10.1088/0029-5515/36/2/I03. 26

[10] I. Lindemuth and R. Kirkpatrick. Parameter space for magnetized fuel targets in inertial confinement fusion. *Nuclear Fusion*, **23** 3 p. 263, 1983. Web: dx.doi.org/10.1088/0029-5515/23/3/001. 27

[11] I. R. Lindemuth, R. E. Reinovsky, R. E. Chrien, J. M. Christian, C. A. Ekdahl, J. H. Goforth, R. C. Haight, G. Idzorek, N. S. King, R. C. Kirkpatrick, R. E. Larson, G. L. Morgan, B. W. Olinger, H. Oona, P. T. Sheehey, J. S. Shlachter, R. C. Smith, L. R. Veeser, B. J. Warthen, S. M. Younger, V. K. Chernyshev, V. N. Mokhov, A. N. Demin, Y. N. Dolin, S. F. Garanin, V. A. Ivanov, V. P. Korchagin, O. D. Mikhailov, I. V. Morozov, S. V. Pak, E. S. Pavlovskii, N. Y. Seleznev, A. N. Skobelev, G. I. Volkov and V. A. Yakubov. Target Plasma Formation for Magnetic Compression/Magnetized Target Fusion. *Physical Review Letters*, **75** 10 pp. 1953–1956, 1995. Web: dx.doi.org/10.1103/PhysRevLett.75.1953. 27

[12] J. Nuckolls, L. Wood, A. Thiessen and G. Zimmerman. Laser Compression of Matter to Super-High Densities: Thermonuclear (CTR) Applications. *Nature*, **239** pp. 139–142, 1972. Web: dx.doi.org/10.1038/239139a0. 27, 79

[13] A. B. Langdon. Nonlinear Inverse Bremsstrahlung and Heated-Electron Distributions. *Physical Review Letters*, **44** pp. 575–579, 1980. Web: dx.doi.org/10.1103/PhysRevLett.44.575. 29

[14] P. Gibbon. *Short Pulse Laser Interactions with Matter*. Imperial College Press, London, UK, 2005. Web: www.worldcat.org/oclc/62673761. 29, 31

[15] D. W. Forslund, J. M. Kindel and E. L. Lindman. Theory of stimulated scattering processes in laser irradiated plasmas. *Physics of Fluids*, **18** 8 pp. 1002–1016, 1975. Web: dx.doi.org/10.1063/1.861248. 30

[16] S. C. Wilks and W. L. Kruer. Absorption of ultrashort, ultra-intense laser light by solids and overdense plasmas. *IEEE Journal of Quantum Electronics*, **33** pp. 1954–1968, 1997. Web: dx.doi.org/10.1109/3.641310. 31, 45

[17] D. W. Forslund, J. M. Kindel and K. Lee. Theory of Hot-Electron Spectra at High Laser Intensity. *Physical Review Letters*, **39** pp. 284–288, 1977. Web: dx.doi.org/10.1103/PhysRevLett.39.284. 31

[18] K. Estabrook and W. L. Kruer. Properties of Resonantly Heated Electron Distributions. *Physical Review Letters*, **40** pp. 42–45, 1978. Web: dx.doi.org/10.1103/PhysRevLett.40.42. 31

[19] A. R. Bell. Transport in Laser-Produced Plasmas. In R. A. Cairns, editor, *Laser Plasma Interactions 5: Inertial Confinement Fusion*, Taylor & Francis Group, Abingdon, UK. 1995. Web: www.worldcat.org/oclc/473324911. 31

[20] L. Rayleigh. Investigation of the Character of the Equilibrium of an Incompressible Heavy Fluid of Variable Density. *Proceedings of the London Mathematical Society*, **s1-14** 1 pp. 170–177, 1882. Web: dx.doi.org/10.1112/plms/s1-14.1.170. 31

[21] H. Takabe, K. Mima, L. Montierth and R. L. Morse. Self-consistent growth rate of the Rayleigh–Taylor instability in an ablatively accelerating plasma. *Physics of Fluids*, **28** 12 pp. 3676–3682, 1985. Web: dx.doi.org/10.1063/1.865099. 32

[22] J. Lindl. Development of the indirect-drive approach to inertial confinement fusion and the target physics basis for ignition and gain. *Physics of Plasmas*, **2** 11 pp. 3933–4024, 1995. Web: dx.doi.org/10.1063/1.871025. 33, 34

[23] D. C. Wilson, P. A. Bradley, N. M. Hoffman, F. J. Swenson, D. P. Smitherman, R. E. Chrien, R. W. Margevicius, D. J. Thoma, L. R. Foreman, J. K. Hoffer, S. R. Goldman, S. E. Caldwell, T. R. Dittrich, S. W. Haan, M. M. Marinak, S. M. Pollaine and J. J. Sanchez. The development and advantages of beryllium capsules for the National Ignition Facility. **5** 5 pp. 1953–1959, 1998. Web: dx.doi.org/10.1063/1.872865. 34

[24] J. H. Hammer, M. Tabak, S. C. Wilks, J. D. Lindl, D. S. Bailey, P. W. Rambo, A. Toor, G. B. Zimmerman and J. John L. Porter. High yield inertial confinement fusion target design for a z-pinch-driven hohlraum. *Physics of Plasmas*, **6** 5 pp. 2129–2136, 1999. Web: dx.doi.org/10.1063/1.873464. 34

[25] M. K. Matzen, M. A. Sweeney, R. G. Adams, J. R. Asay, J. E. Bailey, G. R. Bennett, D. E. Bliss, D. D. Bloomquist, T. A. Brunner, R. B. Campbell, G. A. Chandler, C. A. Coverdale, M. E. Cuneo, J.-P. Davis, C. Deeney, M. P. Desjarlais, G. L. Donovan, C. J. Garasi, T. A. Haill, C. A. Hall, D. L. Hanson, M. J. Hurst, B. Jones, M. D. Knudson, R. J. Leeper, R. W. Lemke, M. G. Mazarakis, D. H. McDaniel, T. A. Mehlhorn, T. J. Nash, C. L. Olson, J. L. Porter, P. K. Rambo, S. E. Rosenthal, G. A. Rochau, L. E. Ruggles, C. L. Ruiz, T. W. L. Sanford, J. F. Seamen, D. B. Sinars, S. A. Slutz, I. C. Smith, K. W. Struve, W. A. Stygar, R. A. Vesey, E. A. Weinbrecht, D. F. Wenger and E. P. Yu. Pulsed-power-driven high energy density physics and inertial confinement fusion research. *Physics of Plasmas*, **12** 5 p. 055503, 2005. Web: dx.doi.org/10.1063/1.1891746. 35

[26] C. A. Haynam, P. J. Wegner, J. M. Auerbach, M. W. Bowers, S. N. Dixit, G. V. Erbert, G. M. Heestand, M. A. Henesian, M. R. Hermann, K. S. Jancaitis, K. R. Manes, C. D. Marshall, N. C. Mehta, J. Menapace, E. Moses, J. R. Murray, M. C. Nostrand, C. D. Orth, R. Patterson, R. A. Sacks, M. J. Shaw, M. Spaeth, S. B. Sutton, W. H. Williams, C. C. Widmayer, R. K. White, S. T. Yang and B. M. V. Wonterghem. National Ignition Facility laser performance status. *Applied Optics*, **46** 16 pp. 3276–3303, 2007. Web: dx.doi.org/10.1364/AO.46.003276. 35

[27] S. C. Cowley and J. John Peoples, editors. *Plasma Science: Advancing Knowledge in the National Interest*, The National Academies Press, Washington DC, US, chap. C. 2007. Web: `www.worldcat.org/oclc/567909228`. 35

[28] C. Bibeau, A. Bayramian, P. Armstrong, E. Ault, R. Beach, M. Benapfl, R. Campbell, J. Dawson, C. Ebbers, B. Freitas, R. Kent, Z. Liao, T. Ladran, J. Menapace, B. Molander, E. Moses, S. Oberhelman, S. Payne, N. Peterson, K. Schaffers, C. Stolz, S. Sutton, J. Tassano, S. Telford, E. Utterback, M. Randles, B. Chai and Y. Fei. The mercury laser system - An average power, gas-cooled, Yb:S-FAP based system with frequency conversion and wavefront correction. *Journal de Physique IV*, **133** pp. 797–803, 2006. Web: `dx.doi.org/10.1051/jp4:2006133161`. 35

[29] S. Banerjee, K. Ertel, P. Mason, C. Hernandez-Gomez and J. Collier. Concept for Cryogenic kJ-Class Yb:YAG Pump Laser. *AIP Conference Proceedings*, **1228** 1 pp. 223–229, 2010. Web: `dx.doi.org/10.1063/1.3426056`. 35

[30] A. Giesen, H. Hgel, A. Voss, K. Wittig, U. Brauch and H. Opower. Scalable concept for diode-pumped high-power solid-state lasers. *Applied Physics B: Lasers and Optics*, **58** pp. 365–372, 1994. Web: `dx.doi.org/10.1007/BF01081875`. 35

[31] J. Wesson. *Tokamaks*, Oxford University Press, Oxford, UK, chap. 1. Third edn., 2004. Web: `www.worldcat.org/oclc/440127078`. 35

[32] J. D. Lawson. Some Criteria for a Power Producing Thermonuclear Reactor. *Proceedings of the Physical Society. Section B*, **70** 1 p. 6, 1957. Web: `dx.doi.org/10.1088/0370-1301/70/1/303`. 35

[33] G. S. Fraley, E. J. Linnebur, R. J. Mason and R. L. Morse. Thermonuclear burn characteristics of compressed deuterium-tritium microspheres. *Physics of Fluids*, **17** 2 pp. 474–489, 1974. Web: `dx.doi.org/10.1063/1.1694739`. 39, 68

[34] Y. B. Zel'dovich and Y. P. Raizer. *Physics of Shock Waves and High-Temperature Hydrodynamic Phenomena*, Dover Publications, Inc., New York, US, chap. 2, 7. 2002. Web: `www.worldcat.org/oclc/48013651`. 41, 99

[35] I. Ross, P. Matousek, M. Towrie, A. Langley and J. Collier. The prospects for ultrashort pulse duration and ultrahigh intensity using optical parametric chirped pulse amplifiers. *Optics Communications*, **144** 1-3 pp. 125 – 133, 1997. Web: `dx.doi.org/10.1016/S0030-4018(97)00399-4`. 42

[36] M. Tabak, J. Hammer, M. E. Glinsky, W. L. Kruer, S. C. Wilks, J. Woodworth, E. M. Campbell, M. D. Perry and R. J. Mason. Ignition and high gain with ultrapowerful lasers. *Physics of Plasmas*, **1** 5 pp. 1626–1634, 1994. Web: `dx.doi.org/10.1063/1.870664`. 42, 79, 91, 109

[37] Y. Sentoku, K. Mima, P. Kaw and K. Nishikawa. Anomalous Resistivity Resulting from MeV-Electron Transport in Overdense Plasma. *Physical Review Letters*, **90** p. 155001, 2003. Web: `dx.doi.org/10.1103/PhysRevLett.90.155001`. 43

[38] M. Tabak, J. H. Hammer, E. M. Campbell, W. L. Kruer, J. Goodworth, S. C. Wilks, and M. Perry. Lawrence Livermore National Laboratory patent disclosure, IL8826B, 1997. 43, 79

[39] R. Kodama, P. A. Norreys, K. Mima, A. E. Dangor, R. G. Evans, H. Fujita, Y. Kitagawa, K. Krushelnick, T. Miyakoshi, N. Miyanaga, T. Norimatsu, S. J. Rose, T. Shozaki, K. Shigemori, A. Sunahara, M. Tampo, K. A. Tanaka, Y. Toyama, T. Yamanaka and M. Zepf. Fast heating of ultrahigh-density plasma as a step towards laser fusion ignition. *Nature*, **42** pp. 798–802, 2001. Web: `dx.doi.org/10.1038/35090525`. 43, 79

[40] R. Kodama, H. Shiraga, K. Shigemori, Y. Toyama, S. Fujioka, H. Azechi, H. Fujita, H. Habara, T. Hall, Y. Izawa, T. Jitsuno, Y. Kitagawa, K. M. Krushelnick, K. L. Lancaster, K. Mima, K. Nagai, M. Nakai, H. Nishimura, T. Norimatsu, P. A. Norreys, S. Sakabe, K. A. Tanaka, A. Youssef, M.Zepf

and T. Yamanak. Fast heating scalable to laser fusion ignition. *Nature*, **43** pp. 933–934, 2002. Web: dx.doi.org/10.1038/418933a. 43

[41] A. Caruso and V. Pais. The ignition of dense DT fuel by injected triggers. *Nuclear Fusion*, **36** 6 p. 745, 1996. Web: dx.doi.org/10.1088/0029-5515/36/6/I06. 43

[42] M. Roth, T. E. Cowan, M. H. Key, S. P. Hatchett, C. Brown, W. Fountain, J. Johnson, D. M. Pennington, R. A. Snavely, S. C. Wilks, K. Yasuike, H. Ruhl, F. Pegoraro, S. V. Bulanov, E. M. Campbell, M. D. Perry and H. Powell. Fast Ignition by Intense Laser-Accelerated Proton Beams. *Physical Review Letters*, **86** pp. 436–439, 2001. Web: dx.doi.org/10.1103/PhysRevLett.86.436. 43

[43] R. Betti, C. D. Zhou, K. S. Anderson, L. J. Perkins, W. Theobald and A. A. Solodov. Shock Ignition of Thermonuclear Fuel with High Areal Density. *Physical Review Letters*, **98** 15 p. 155001, 2007. Web: dx.doi.org/10.1103/PhysRevLett.98.155001. 43

[44] M. H. Key. Status of and prospects for the fast ignition inertial fusion concept. *Physics of Plasmas*, **14** 5 p. 055502, 2007. Web: dx.doi.org/10.1063/1.2719178. 43

[45] F. Cattani, A. Kim, D. Anderson and M. Lisak. Threshold of induced transparency in the relativistic interaction of an electromagnetic wave with overdense plasmas. *Physical Review E*, **62** pp. 1234–1237, 2000. Web: dx.doi.org/10.1103/PhysRevE.62.1234. 45

[46] M. G. Haines, M. S. Wei, F. N. Beg and R. B. Stephens. Hot-Electron Temperature and Laser-Light Absorption in Fast Ignition. *Physical Review Letters*, **102** p. 045008, 2009. Web: dx.doi.org/10.1103/PhysRevLett.102.045008. 45

[47] A. R. Bell, J. R. Davies, S. Guerin and H. Ruhl. Fast-electron transport in high-intensity short-pulse laser - solid experiments. *Plasma Physics and Controlled Fusion*, **39** 5 p. 653, 1997. Web: dx.doi.org/10.1088/0741-3335/39/5/001. 45

[48] J. S. Green, V. M. Ovchinnikov, R. G. Evans, K. U. Akli, H. Azechi, F. N. Beg, C. Bellei, R. R. Freeman, H. Habara, R. Heathcote, M. H. Key, J. A. King, K. L. Lancaster, N. C. Lopes, T. Ma, A. J. MacKinnon, K. Markey, A. McPhee, Z. Najmudin, P. Nilson, R. Onofrei, R. Stephens, K. Takeda, K. A. Tanaka, W. Theobald, T. Tanimoto, J. Waugh, L. Van Woerkom, N. C. Woolsey, M. Zepf, J. R. Davies and P. A. Norreys. Effect of Laser Intensity on Fast-Electron-Beam Divergence in Solid-Density Plasmas. *Physical Review Letters*, **100** 1 p. 015003, 2008. Web: `dx.doi.org/10.1103/PhysRevLett.100.015003`. 46

[49] R. Kodama, Y. Sentoku, Z. L. Chen, G. R. Kumar, S. P. Hatchett, Y. Toyama, T. E. Cowan, R. R. Freeman, J. Fuchs, Y. Izawa, M. H. Key, Y. Kitagawa, K. Kondo, T. Matsuoka, H. Nakamura, M. Nakatsutsumi, P. A. Norreys, T. Norimatsu, R. A. Snavely, R. B. Stephens, M. Tampo, K. A. Tanaka and T. Yabuuchi. Plasma devices to guide and collimate a high density of MeV electrons. *Nature*, **432** pp. 1005–1008, 2004. Web: `dx.doi.org/10.1038/nature03133`. 46, 131

[50] M. I. K. Santala, M. Zepf, I. Watts, F. N. Beg, E. Clark, M. Tatarakis, K. Krushelnick, A. E. Dangor, T. McCanny, I. Spencer, R. P. Singhal, K. W. D. Ledingham, S. C. Wilks, A. C. Machacek, J. S. Wark, R. Allott, R. J. Clarke and P. A. Norreys. Effect of the Plasma Density Scale Length on the Direction of Fast Electrons in Relativistic Laser-Solid Interactions. *Physical Review Letters*, **84** 7 pp. 1459–1462, 2000. Web: `dx.doi.org/10.1103/PhysRevLett.84.1459`. 46

[51] J. R. Davies, A. R. Bell, M. G. Haines and S. M. Guérin. Short-pulse high-intensity laser-generated fast electron transport into thick solid targets. *Physical Review E*, **56** pp. 7193–7203, 1997. Web: `dx.doi.org/10.1103/PhysRevE.56.7193`. 46, 80

[52] J. R. Davies, A. R. Bell and M. Tatarakis. Magnetic focusing and trapping of high-intensity laser-generated fast electrons at the rear of solid targets. *Physical Review E*, **59** pp. 6032–6036, 1999. Web: `dx.doi.org/10.1103/PhysRevE.59.6032`. 46

[53] J. C. Maxwell. A Dynamical Theory of the Electromagnetic Field. *Philosophical Transactions of the Royal Society of London*, **155** pp. 459–512, 1865. Web: `rstl.royalsocietypublishing.org/content/155/459.short`. 49

[54] P. J. W. Debye and E. A. A. J. Hückel. Zur Theorie der Elektrolyte. I. Gefrierpunktserniedrigung und verwandte Erscheinungen (The theory of electrolytes. I. Lowering of freezing point and related phenomena). **184** pp. 185–206, 1923. Web: `electrochem.cwru.edu/estir/history.htm`. 50

[55] R. J. Hastie. Plasma particle dynamics. In R. Dendy, editor, *Plasma Physics: An Introductory Course*, Cambridge University Press, Cambridge, UK. 1993. Web: `www.worldcat.org/oclc/463980592`. 50

[56] L. Boltzmann. *Lectures in Gas Theory*. University of California Press, Berkeley, US, 1964. Web: `www.worldcat.org/oclc/462821354`. 52

[57] J. A. Elliott. Plasma kintetic theory. In R. Dendy, editor, *Plasma Physics: An Introductory Course*, Cambridge University Press, Cambridge, UK. 1993. Web: `www.worldcat.org/oclc/463980592`. 52, 53

[58] D. A. Gurnett and A. Bhattacharjee. *Introduction to Plasma Physics*. Cambridge University Press, Cambridge, UK, 2005. Web: `www.worldcat.org/oclc/442874677`. 52, 60, 61

[59] A. A. Vlasov. The Vibrational Properties of an Electron Gas. *Soviet Physics Uspekhi*, **10** 6 p. 721. Web: `dx.doi.org/10.1070/PU1968v010n06ABEH003709`. 52

[60] J. Hubbard. The Friction and Diffusion Coefficients of the Fokker-Planck Equation in a Plasma. *Proceedings of the Royal Society of London. Series A. Mathematical and Physical Sciences*, **260** 1300 pp. 114–126, 1961. Web: `dx.doi.org/10.1098/rspa.1961.0017`. 53

[61] T. J. M. Boyd and J. J. Sanderson. *The Physics of Plasmas*. Cambridge University Press, Cambridge, UK, 2003. Web: `www.worldcat.org/oclc/49327007`. 62, 65

[62] L. Spitzer. *Physics of Fully Ionized Gases*. Dover Publications, Inc., Mineola, New York, US, 2nd edn., 1962. Web: `www.worldcat.org/oclc/255559775`. 64, 66, 69, 83

[63] L. Spitzer and R. Härm. Transport Phenomena in a Completely Ionized Gas. *Physical Review*, **89** pp. 977–981, 1953. Web: `dx.doi.org/10.1103/PhysRev.89.977`. 64

[64] Y. T. Lee and R. M. More. An electron conductivity model for dense plasmas. *Physics of Fluids*, **27** 5 pp. 1273–1286, 1984. Web: `dx.doi.org/10.1063/1.864744`. 65, 66

[65] Y. Zhang, J. Zhang, S. hua Pan and Y. xin Nie. A simple model for electron temperature and penetration depth in interaction of ultra-short laser pulses with solid targets. *Journal of Physics D: Applied Physics*, **30** 4 p. 655, 1997. Web: `dx.doi.org/10.1088/0022-3727/30/4/021`. 66

[66] K. A. Brueckner and S. Jorna. Laser-driven fusion. *Rev. Mod. Phys.*, **46** pp. 325–367, 1974. Web: `dx.doi.org/10.1103/RevModPhys.46.325`. 66

[67] L. Spitzer, Jr. The stability of isolated clusters. *Monthly Notices of the Royal Astronomical Society*, **100** p. 396, 1940. Web: `adsabs.harvard.edu/abs/1940MNRAS.100..396S`. 69

[68] G. A and Sod. A survey of several finite difference methods for systems of nonlinear hyperbolic conservation laws. *Journal of Computational Physics*, **27** 1 pp. 1 – 31, 1978. Web: `dx.doi.org/10.1016/0021-9991(78)90023-2`. 71, 102

[69] C. P. Ridgers. *Magnetic Fields and Non-Local Transport in Laser Plasmas*. Ph.D. thesis, Imperial College London, 2008. Web: `unicorn.lib.ic.ac.uk/uhtbin/primo/638365`. 72, 74

[70] U. Ziegler. A central-constrained transport scheme for ideal magnetohydrodynamics. *Journal of Computational Physics*, **196** pp. 393–416, 2004. Web: `dx.doi.org/10.1016/j.jcp.2003.11.003`. 74, 75, 92

[71] P.L and Roe. Approximate Riemann solvers, parameter vectors, and difference schemes. *Journal of Computational Physics*, **43** 2 pp. 357 – 372, 1981. Web: dx.doi.org/10.1016/0021-9991(81)90128-5. 74

[72] S. K. Godunov. A Difference Scheme for Numerical Solution of Discontinuous Solution of Hydrodynamic Equations. *Mathematics Sbornik*, **47** pp. 271–306, 1959. Web: mi.mathnet.ru/eng/msb4873. 74

[73] A. Kurganov, S. Noelle and G. Petrova. Semidiscrete Central-Upwind Schemes for Hyperbolic Conservation Laws and Hamilton–Jacobi Equations. *SIAM Journal on Scientific Computing*, **23** pp. 707–740, 2001. Web: dx.doi.org/10.1137/S1064827500373413. 74

[74] C. R. Evans and J. F. Hawley. Simulation of magnetohydrodynamic flows - A constrained transport method. *Astrophysical Journal*, **332** pp. 659–677, 1988. Web: dx.doi.org/10.1086/166684. 75

[75] D. S. Balsara and D. S. Spicer. A Staggered Mesh Algorithm Using High Order Godunov Fluxes to Ensure Solenoidal Magnetic Fields in Magnetohydrodynamic Simulations. *Journal of Computational Physics*, **149** 2 pp. 270 – 292, 1999. Web: dx.doi.org/10.1006/jcph.1998.6153. 75

[76] W. H. Press, S. A. Teukolsky, W. T. Vetterling and B. P. Flannery. *Numerical Recipes in Fortran 90*, Cambridge University Press, Cambridge, UK, vol. 2, chap. B2, B7. 1996. Web: www.worldcat.org/oclc/496213871. 77, 152, 157, 161

[77] P. Norreys, R. Scott, K. Lancaster, J. Green, A. Robinson, M. Sherlock, R. Evans, M. Haines, S. Kar, M. Zepf, M. Key, J. King, T. Ma, T. Yabuuchi, M. Wei, F. Beg, P. Nilson, W. Theobald, R. Stephens, J. Valente, J. Davies, K. Takeda, H. Azechi, M. Nakatsutsumi, T. Tanimoto, R. Kodama and K. Tanaka. Recent fast electron energy transport experiments relevant to fast ignition inertial fusion. *Nuclear Fusion*, **49** 10 p. 104023, 2009. Web: dx.doi.org/10.1088/0029-5515/49/10/104023. 79

[78] D. A. Hammer and N. Rostoker. Propagation of High Current Relativistic Electron Beams. *Physics of Fluids*, **13** pp. 1831–1850, 1970. Web: dx.doi.org/10.1063/1.1693161. 80

[79] M. E. Glinsky. Regimes of suprathermal electron transport. *Physics of Plasmas*, **2** pp. 2796–2806, 1995. Web: dx.doi.org/10.1063/1.871472. 80

[80] R. J. Kingham, M. Sherlock, C. P. Ridgers and R. G. Evans. Vlasov-Fokker-Planck simulations of fast-electron transport with hydrodynamic plasma response. *Journal of Physics: Conference Series*, **244** 2 p. 022042, 2010. Web: dx.doi.org/10.1088/1742-6596/244/2/022042. 81

[81] A. R. Bell. The interaction of cosmic rays and magnetized plasma. *Monthly Notices of the Royal Astronomical Society*, **358** pp. 181–187, 2005. Web: dx.doi.org/10.1111/j.1365-2966.2005.08774.x. 81, 82

[82] A. V. Brantov, V. Y. Bychenkov and W. Rozmus. Ion acoustic instability driven by a temperature gradient in laser-produced plasmas. *Physics of Plasmas*, **8** pp. 3558–3564, 2001. Web: dx.doi.org/10.1063/1.1379760. 83

[83] M. Tabak, D. S. Clark, S. P. Hatchett, M. H. Key, B. F. Lasinski, R. A. Snavely, S. C. Wilks, R. P. J. Town, R. Stephens, E. M. Campbell, R. Kodama, K. Mima, K. A. Tanaka, S. Atzeni and R. Freeman. Review of progress in Fast Ignition. *Physics of Plasmas*, **12** 5 p. 057305, 2005. Web: dx.doi.org/10.1063/1.1871246. 91

[84] A. R. Bell and R. J. Kingham. Resistive Collimation of Electron Beams in Laser-Produced Plasmas. *Physical Review Letters*, **91** 3 p. 035003, 2003. Web: dx.doi.org/10.1103/PhysRevLett.91.035003. 91

[85] A. P. L. Robinson and M. Sherlock. Magnetic collimation of fast electrons produced by ultraintense laser irradiation by structuring the target composition. *Physics of Plasmas*, **14** 8 p. 083105, 2007. Web: dx.doi.org/10.1063/1.2768317. 91, 101

[86] E. Kreyszig. *Advanced Engineering Mathematics*. John Willey & Sons, New York, US, 1999. Web: `www.worldcat.org/oclc/442094237`. 93

[87] D. Ryu and T. W. Jones. Numerical magetohydrodynamics in astrophysics: Algorithm and tests for one-dimensional flow. *Astrophysical Journal*, **442** pp. 228–258, 1995. Web: `dx.doi.org/10.1086/175437`. 13, 93, 94, 95

[88] R. Courant, K. Friedrichs and H. Lewy. On the Partial Difference Equations of Mathematical Physics. *IBM Journal of Research and Development*, **11** 2 pp. 215 –234, 1967. Web: `dx.doi.org/10.1147/rd.112.0215`. 94

[89] L. I. Sedov. Propagation of strong shock waves. *Journal of Applied Mathematics and Mechanics*, **10** pp. 241–250, 1946. Web: `www.journals.elsevier.com/journal-of-applied-mathematics-and-mechanics/`. 99

[90] L. I. Sedov. *Similarity and dimensional methods in mechanics*. Infosearch Ltd., London, UK, 1959. Web: `www.worldcat.org/oclc/220175107`. 99

[91] R. B. Stephens, R. A. Snavely, Y. Aglitskiy, F. Amiranoff, C. Andersen, D. Batani, S. D. Baton, T. Cowan, R. R. Freeman, T. Hall, S. P. Hatchett, J. M. Hill, M. H. Key, J. A. King, J. A. Koch, M. Koenig, A. J. MacKinnon, K. L. Lancaster, E. Martinolli, P. Norreys, E. Perelli-Cippo, M. Rabec Le Gloahec, C. Rousseaux, J. J. Santos and F. Scianitti. K_α fluorescence measurement of relativistic electron transport in the context of fast ignition. *Physical Review E*, **69** p. 066414, 2004. Web: `dx.doi.org/10.1103/PhysRevE.69.066414`. 99

[92] A. P. L. Robinson, M. H. Key and M. Tabak. Focusing of Relativistic Electrons in Dense Plasma Using a Resistivity-Gradient-Generated Magnetic Switchyard. *Phys. Rev. Lett.*, **108** p. 125004, 2012. Web: `dx.doi.org/10.1103/PhysRevLett.108.125004`. 101

[93] S. Kar, A. P. L. Robinson, D. C. Carroll, O. Lundh, K. Markey, P. McKenna, P. Norreys and M. Zepf. Guiding of Relativistic Electron Beams in Solid Targets by Resistively Controlled Magnetic Fields. *Physical Review Letters*, **102** p. 055001, 2009. Web: `dx.doi.org/10.1103/PhysRevLett.102.055001`. 101

[94] W. Seka, S. Jacobs, J. Rizzo, R. Boni and R. Craxton. Demonstration of high efficiency third harmonic conversion of high power Nd-glass laser radiation. *Optics Communications*, **34** 3 pp. 469 – 473, 1980. Web: dx.doi.org/10.1016/0030-4018(80)90419-8. 110

[95] L. V. Woerkom, K. U. Akli, T. Bartal, F. N. Beg, S. Chawla, C. D. Chen, E. Chowdhury, R. R. Freeman, D. Hey, M. H. Key, J. A. King, A. Link, T. Ma, A. J. MacKinnon, A. G. MacPhee, D. Offermann, V. Ovchinnikov, P. K. Patel, D. W. Schumacher, R. B. Stephens and Y. Y. Tsui. Fast electron generation in cones with ultraintense laser pulses. *Physics of Plasmas*, **15** 5 p. 056304, 2008. Web: dx.doi.org/10.1063/1.2890124. 15, 111, 133

[96] R. J. Clarke, D. Neely, R. D. Edwards, P. N. M. Wright, K. W. D. Ledingham, R. Heathcote, P. McKenna, C. N. Danson, P. A. Brummitt, J. L. Collier, P. E. Hatton, S. J. Hawkes, C. Hernandez-Gomez, P. Holligan, M. H. R. Hutchinson, A. K. Kidd, W. J. Lester, D. R. Neville, P. A. Norreys, D. A. Pepler, T. B. Winstone, R. W. W. Wyatt and B. E. Wyborn. Radiological characterisation of photon radiation from ultra-high-intensity laserplasma and nuclear interactions. *Journal of Radiological Protection*, **26** 3 p. 277, 2006. Web: dx.doi.org/10.1088/0952-4746/26/3/002. 111

[97] C. N. Danson, J. Collier, D. Neely, L. J. Barzanti, A. Damerell, C. B. Edwards, M. H. R. Hutchinson, M. H. Key, P. A. Norreys, D. A. Pepler, I. N. Ross, P. F. Taday, W. T. Toner, M. Trentelman, F. N. Walsh, T. B. Winstone and R. W. W. Wyatt. Well characterized 1019W cm2 operation of VULCAN–an ultra-high power Nd:glass laser. *Journal of Modern Optics*, **45** pp. 1653–1669, 1998. Web: dx.doi.org/10.1080/09500349808230660. 113

[98] C. Spindloe, M. K. Tolley, P. Hiscock, M. Beardsley and J. J. Spencer. An Update of Target Fabrication Techniques for the Mass Production of Advanced Fast Ignition Cone Targets. *Fusion Science and Technology*, **59** 1 pp. 221–226, 2011. Web: epubs.cclrc.ac.uk/work-details?w=55042. 113

[99] A. Thompson and D. Vaughan. *Centre for X-ray Optics and Advanced Light Source X-ray Data Booklet*, Lawrence Berkeley National Laboratory, Berkeley, US, chap. 1.2. 2009. Web: `xdb.lbl.gov`. 115

[100] J. A. Koch, Y. Aglitskiy, C. Brown, T. Cowan, R. Freeman, S. Hatchett, G. Holland, M. Key, A. MacKinnon, J. Seely, R. Snavely and R. Stephens. 4.5- and 8-keV emission and absorption x-ray imaging using spherically bent quartz 203 and 211 crystals (invited). *Review of Scientific Instruments*, **74** pp. 2130–2135, 2003. Web: `dx.doi.org/10.1063/1.1537448`. 116

[101] K. U. Akli, M. H. Key, H. K. Chung, S. B. Hansen, R. R. Freeman, M. H. Chen, G. Gregori, S. Hatchett, D. Hey, N. Izumi, J. King, J. Kuba, P. Norreys, A. J. Mackinnon, C. D. Murphy, R. Snavely, R. B. Stephens, C. Stoeckel, W. Theobald and B. Zhang. Temperature sensitivity of Cu K_α imaging efficiency using a spherical Bragg reflecting crystal. *Physics of Plasmas*, **14** 2 023102 (pages 9), 2007. Web: `dx.doi.org/10.1063/1.2431632`. 116, 125

[102] A. K. Freund, A. Munkholm and S. Brennan. X-ray diffraction properties of highly oriented pyrolytic graphite. SPIE, 1996, vol. 2856, pp. 68–79. Web: `dx.doi.org/10.1117/12.259851`. 116

[103] M. O. Krause and J. H. Oliver. Natural widths of atomic K and L levels, Kα X-ray lines and several KLL Auger lines. *Journal of Physical and Chemical Reference Data*, **8** pp. 329–338, 1979. Web: `www.nist.gov/data/PDFfiles/jpcrd137.pdf`. 117

[104] A. Pak, G. Gregori, J. Knight, K. Campbell, D. Price, B. Hammel, O. L. Landen and S. H. Glenzer. X-ray line measurements with high efficiency Bragg crystals. *Review of Scientific Instruments*, **75** 10 pp. 3747 –3749, 2004. Web: `dx.doi.org/10.1063/1.1788870`. 117

[105] A. L. Meadowcroft, C. D. Bentley and E. N. Stott. Evaluation of the sensitivity and fading characteristics of an image plate system for x-ray diagnostics. *Review of Scientific Instruments*, **79** 11 113102 (pages 4), 2008. Web: `dx.doi.org/10.1063/1.3013123`. 118

[106] S. G. Gales and C. D. Bentley. Image plates as x-ray detectors in plasma physics experiments. *Review of Scientific Instruments*, **75** 10 pp. 4001–4003, 2004. Web: dx.doi.org/10.1063/1.1789256. 118

[107] K. A. Tanaka, T. Yabuuchi, T. Sato, R. Kodama, Y. Kitagawa, T. Takahashi, T. Ikeda, Y. Honda and S. Okuda. Calibration of imaging plate for high energy electron spectrometer. *Review of Scientific Instruments*, **76** 1 p. 013507, 2005. Web: dx.doi.org/10.1063/1.1824371. 118

[108] C. Stoeckl, W. Theobald, T. C. Sangster, M. H. Key, P. Patel, B. B. Zhang, R. Clarke, S. Karsch and P. Norreys. Operation of a single-photon counting x-ray charge-coupled device camera spectrometer in a petawatt environment. *Review of Scientific Instruments*, **75** 10 pp. 3705 –3707, 2004. Web: dx.doi.org/10.1063/1.1788867. 119

[109] B. R. Maddox, H. S. Park, B. A. Remington and M. McKernan. Calibration and characterization of single photon counting cameras for short-pulse laser experiments. *Review of Scientific Instruments*, **79** 10 p. 10E924, 2008. Web: dx.doi.org/10.1063/1.2966374. 119

[110] I. H. Hutchinson. *Principles of Plasma Diagnostics*. Cambridge University Press, Cambridge, UK, 2002. Web: www.worldcat.org/oclc/470316242. 120

[111] K. L. Lancaster, J. Pasley, J. S. Green, D. Batani, S. Baton, R. G. Evans, L. Gizzi, R. Heathcote, C. H. Gomez, M. Koenig, P. Koester, A. Morace, I. Musgrave, P. A. Norreys, F. Perez, J. N. Waugh and N. C. Woolsey. Temperature profiles derived from transverse optical shadowgraphy in ultraintense laser plasma interactions at 6×10^{20} W cm^{-2}. *Physics of Plasmas*, **16** 5 056707 (pages 5), 2009. Web: dx.doi.org/10.1063/1.3133024. 120

[112] B. Henke, E. Gullikson and J. Davis. X-Ray Interactions: Photoabsorption, Scattering, Transmission, and Reflection at E = 50-30,000 eV, Z = 1-92. *Atomic Data and Nuclear Data Tables*, **54** 2 pp. 181 – 342, 1993. Web: dx.doi.org/10.1006/adnd.1993.1013. 122

[113] M. Nakatsutsumi, R. Kodama, Y. Aglitskiy, K. U. Akli, D. Batani, S. D. Baton, F. N. Beg, A. Benuzzi-Mounaix, S. N. Chen, D. Clark, J. R. Davies, R. R. Freeman, J. Fuchs, J. S. Green, C. D. Gregory, P. Guillou, H. Habara, R. Heathcote, D. S. Hey, K. Highbarger, P. Jaanimagi, M. H. Key, M. Koenig, K. Krushelnick, K. L. Lancaster, B. Loupias, T. Ma, A. Macphee, A. J. Mackinonn, K. Mima, A. Morace, H. Nakamura, P. A. Norryes, D. Piazza, C. Rousseaux, R. B. Stephans, M. Storm, M. Tampo, W. Theobald, L. V. Woerkom, R. L. Weber, M. S. Wei and N. C. Woolsey. Heating of solid target in electron refluxing dominated regime with ultra-intense laser. *Journal of Physics: Conference Series*, **112** 2 p. 022063, 2008. Web: dx.doi.org/10.1088/1742-6596/112/2/022063. 124

[114] J. T. Larsen and S. M. Lane. HYADES-A plasma hydrodynamics code for dense plasma studies. *Journal of Quantitative Spectroscopy and Radiative Transfer*, **51** 1-2 pp. 179 – 186, 1994. Web: dx.doi.org/10.1016/0022-4073(94)90078-7. 125

[115] T. Ma, H. Sawada, P. K. Patel, C. D. Chen, L. Divol, D. P. Higginson, A. J. Kemp, M. H. Key, D. J. Larson, S. Le Pape, A. Link, A. G. MacPhee, H. S. McLean, Y. Ping, R. B. Stephens, S. C. Wilks and F. N. Beg. Hot Electron Temperature and Coupling Efficiency Scaling with Prepulse for Cone-Guided Fast Ignition. *Physical Review Letters*, **108** p. 115004, 2012. Web: dx.doi.org/10.1103/PhysRevLett.108.115004. 127

[116] M. Sherlock. Universal scaling of the electron distribution function in one-dimensional simulations of relativistic laser-plasma interactions. *Physics of Plasmas*, **16** 10 p. 103101, 2009. Web: dx.doi.org/10.1063/1.3240341. 128

[117] J. P. Santos, F. Parente and Y.-K. Kim. Cross sections for K-shell ionization of atoms by electron impact. *Journal of Physics B: Atomic, Molecular and Optical Physics*, **36** 21 p. 4211, 2003. Web: dx.doi.org/10.1088/0953-4075/36/21/002. 128

[118] A. G. R. Thomas *et al.* In preparation. 128

[119] D. K. Brice. Stopping powers for electrons and positrons (ICRU report 37). *Nuclear Instruments and Methods in Physics Research B*, **12** pp. 187–188, 1985. Web: dx.doi.org/10.1016/0168-583X(85)90718-9. 17, 131, 132

[120] J. A. King, K. U. Akli, R. R. Freeman, J. Green, S. P. Hatchett, D. Hey, P. Jamangi, M. H. Key, J. Koch, K. L. Lancaster, T. Ma, A. J. MacKinnon, A. Macphee, P. A. Norreys, P. K. Patel, T. Phillips, R. B. Stephens, W. Theobald, R. P. J. Town, L. van Woerkom, B. Zhang and F. N. Beg. Studies on the transport of high intensity laser-generated hot electrons in cone coupled wire targets. *Physics of Plasmas*, **16** 2 p. 020701, 2009. Web: dx.doi.org/10.1063/1.3076142. 131

[121] G. Rinker and G. Bohannon. Focused Beam Ray Tracing for Laser Fusion. *Plasma Science, IEEE Transactions on*, **8** 2 pp. 55 –60, 1980. Web: dx.doi.org/10.1109/TPS.1980.4317271. 133

[122] S. D. Baton, M. Koenig, J. Fuchs, A. Benuzzi-Mounaix, P. Guillou, B. Loupias, T. Vinci, L. Gremillet, C. Rousseaux, M. Drouin, E. Lefebvre, F. Dorchies, C. Fourment, J. J. Santos, D. Batani, A. Morace, R. Redaelli, M. Nakatsutsumi, R. Kodama, A. Nishida, N. Ozaki, T. Norimatsu, Y. Aglitskiy, S. Atzeni and A. Schiavi. Inhibition of fast electron energy deposition due to preplasma filling of cone-attached targets. *Physics of Plasmas*, **15** 4 042706 (pages 11), 2008. Web: dx.doi.org/10.1063/1.2903054. 133

[123] M. Nakatsutsumi, R. Kodama, P. A. Norreys, S. Awano, H. Nakamura, T. Norimatsu, A. Ooya, M. Tampo, K. A. Tanaka, T. Tanimoto, T. Tsutsumi and T. Yabuuchi. Reentrant cone angle dependence of the energetic electron slope temperature in high-intensity laser-plasma interactions. *Physics of Plasmas*, **14** p. 050701, 2007. Web: dx.doi.org/10.1063/1.2730490. 134

[124] Y. Ping, R. Shepherd, B. F. Lasinski, M. Tabak, H. Chen, H. K. Chung, K. B. Fournier, S. B. Hansen, A. Kemp, D. A. Liedahl, K. Widmann, S. C. Wilks, W. Rozmus and M. Sherlock. Absorption of Short Laser Pulses on

Solid Targets in the Ultrarelativistic Regime. *Physical Review Letters*, **100** 8 p. 085004, 2008. Web: dx.doi.org/10.1103/PhysRevLett.100.085004. 136

[125] P. J. Schneider and D. H. Eberly. *Geometric Tools for Computer Graphics*, Morgan Kaufmann Publishers, Amsterdam, Netherlands, chap. 11. 2002. Web: www.worldcat.org/oclc/301058662. 157